Molecular Properties of Mesogenic Fragments and Molecules from First Principles

C. J. Adam

A thesis submitted in fulfilment of the requirements

for the degree of Doctor of Philosophy

to the

University of Edinburgh

1998

EX BIBL. UNIV. EDINBURGEN

abstract

In order to gain a deeper understanding of the relationship between molecular structure and liquid crystal properties, accurate data is required on single molecule properties of mesogenic fragments and molecules. This thesis applies a pseudopotential plane wave total energy method to calculate molecular properties of prototypical mesogenic fragments and the molecule 4-n-pentyl-4′-cyanobiphenyl (5CB) from first principles. Optimised molecular structures, vibrational properties and torsional potentials are determined and found to compare well with experimental observations and other *ab initio* investigations. A study is made of the transferability of torsional potentials between mesogenic fragments and 5CB. Also investigated is the conformation-dependence of dipole and quadrupole moments. The strength of the coupling is found to depend sensitively on the molecular structure and the conformation-dependence of quadrupole moments is found to significantly influence inter-molecular interactions. Finally, by combining first principles calculations with an empirical mean field approximation, conformational distributions of the alkyl tail in 5CB are examined.

Much of the work described in this thesis has been submitted for publication.

- "Conformation dependent molecular dipoles of liquid crystal molecules from first principles computer simulation", C. J. Adam, S. J. Clark, G. J. Ackland and J. Crain. *Phys Rev E*, 55:5641, 1997.

- "Properties of liquid crystal molecules and mesogenic fragments from first principles computer simulation", S. J. Clark, C. J. Adam, J. White, G. J. Ackland and J. Crain. *Liquid Crystals*, 22:477, 1997.

- "Transferability of First Principles Derived Torsional Potentials for Mesogenic Molecules". C. J. Adam, S. J. Clark, M. R. Wilson and J. Crain, *Mol. Phys.*, 93:947, 1998

- "Molecular properties of mesogenic molecules from first principles", C. J. Adam, S. J. Clark, G. J. Ackland and J. Crain. In R. J. Allan, editor, *High Performance Computing*, Plenum Press, New York, 1998.

- "Molecular properties of liquid crystals calculated by first principles calculations performed on a Cray T3D", C. J. Adam, S. J. Clark, G. J.Ackland and J. Crain. *SPIE Proceedings of the European Conference on Liquid Crystals*, 3318:171, 1998.

- "A first principles and mean field investigation of the conformational properties of 5CB", C. J. Adam, A. Ferrarini, M. R. Wilson, G. J. Ackland and J. Crain. *Mol. Phys.*, 1998.

- "The influence of conformation dependent quadrupoles on inter-molecular interactions", C. J. Adam, M. P. Neal, S. J. Clark, G. J. Ackland and J. Crain. *Mol. Phys.*, 1998.

Acknowledgements

There are several people who have helped me over the last three years. I must first thank Dr. Jason Crain and Dr. Greame Ackland, for their supervision on the nature and direction of my work. Many thanks also goes to Dr. Alberta Ferrarini of Padova University, Dr. Mark Wilson and Dr. Stewart Clark of Durham University, Dr Maureen Neal of Coventry University and Dr. Pardeep Ahluwalia, who helped me solve several difficulties encountered during my research.

And finally, I especially thank my parents, Derek and Muriel Adam, and my girlfriend Dr. Marion Dimigen, for their constant encouragement and support.

Contents

Chapter 1

Introduction

The unique anisotropic, optical, electrical, magnetic and mechanical properties of liquid crystals (which are detailed by De Gennes [1]), have kept them at the focus of intense research activity for decades. Although they have been extensively studied for the last 25 years, only a number of empirical rules have been formulated that describe the relationship between the bulk properties of liquid crystals and those of the single molecule [2]; the so called structure-property relationship. Since only minor changes in molecular structure are enough to alter bulk properties [2, 3], it is obvious that this relationship is complex.

Many attempts to develop a deeper understanding of the structure-property relationship have been hindered by a lack of information on single molecule properties, such as conformational dynamics, electrostatic moments and molecular structures. However, with increasing computational power, first principles computer simulations provide an attractive route to such properties and are now able to tackle both mesogenic (liquid crystal forming) molecules and fragments. This thesis applies a reliable, accurate and computationally efficient pseudopotential plane wave total energy method to determine single molecule properties of mesogenic fragments and the prototypical mesogenic molecule 4-n-pentyl-4′-cyanobiphenyl (5CB).

The layout of this thesis is as follows. This chapter gives a brief introduction to

liquid crystals, their molecular properties and computer simulations. Chapter 2 gives a brief description of the theory, applications and general considerations relating to first principles calculations. Chapters 3 to 6 describe the results of calculations to determine molecular properties such as equilibrium structure, molecular vibrations, torsional potentials, electrostatic moments and their conformational dependence, and the influence of the nematic environment, described in terms of the surface tensor model, on conformational distributions. Each Chapter begins with an introduction to the particular molecular property under investigation.

1.0.1 Introduction to liquid crystals

A mesophase is a state of order which is intermediate between between solid and liquid. Today there are many materials known to exhibit mesophase transitions in passing from solid to liquid. The classification of these mesophases depends on the degree and nature of the ordering which they possess. However, there are two basic types of mesophase that have been observed. First there are those which retain a 3-dimensional crystal lattice, but are characterised by orientational disorder (i.e. plastic crystals) and second, those having no lattice, but exhibiting approximate orientational order (i.e. liquid crystals). Plastic crystals tend to be formed by molecules with spherical symmetry such as methane whereas liquid crystals tend to be formed by elongated molecules. This was to be expected since orientational ordering only has meaning when the constituent molecules are non-spherical.

Liquid crystals flow freely and assume the shape of their container, a property most common with the macroscopic behaviour of ordinary liquids [1]. There are two types of liquid crystals, thermotropic and lyotropic. Thermotropic liquid crystals are formed by thermal effects (i.e. heating a solid or cooling a liquid phase), whereas lyotropic liquid crystals are formed as a result of solute-solvent mixtures. Figure 1.1 summarises these relationships. The work in this thesis is entirely confined to thermotropic mesogenic molecules and fragments.

The first observation of a liquid crystal was provided by the Austrian botanist Reinitzer [4], who in 1888 witnessed unusual melting behaviour in certain organic compounds. He observed that on heating, crystals of cholesterol benzoate melted to form a cloudy liquid at 145.5°C, which then cleared at a higher temperature of 178.5°C to form a transparent liquid. This first discovery is now recognised to be a chiral nematic liquid crystal. It was not known until later, that the unique properties of liquid crystals arise from the long range orientational order of the molecules. Although each molecule in a liquid crystal undergoes continuous thermal fluctuations in orientation, it is possible to define an average molecular orientation at any location in the fluid. The direction of this average orientation is represented by a unit vector $\hat{\mathbf{n}}$, called the director.

Since the first discovery many mesogenic compounds have been discovered, although it was not until the latter part of this century that substantial effort has gone into the systematic investigation of the structure-property relationship. One vital consequence of orientational ordering is the anisotropy of bulk properties of the mesophase, such as the refractive index and dielectric permittivity, both of which are essential for many applications of liquid crystals [5]. In the 1960's, renewed interest in liquid crystals centred on their electro-optic properties and their use in display technology [6]. Some significant advances were made in the synthesis of stable room temperature nematics that could be used in display technology [7]. Today liquid crystal research encompasses all the major science disciplines and constitutes a major scientific challenge. This research is motivated not only by the increasing stringent demands of display technology but also by applications to such diverse areas as data storage mediums [8] and medicine [1].

Thermotropic mesophases

Thermotropic mesophases are divided into two main categories: nematic and smectic. The nematic phase is uniaxial (there exists rotational symmetry around the director $\hat{\mathbf{n}}$) and consists of molecules lined up preferentially to each other but distributed randomly

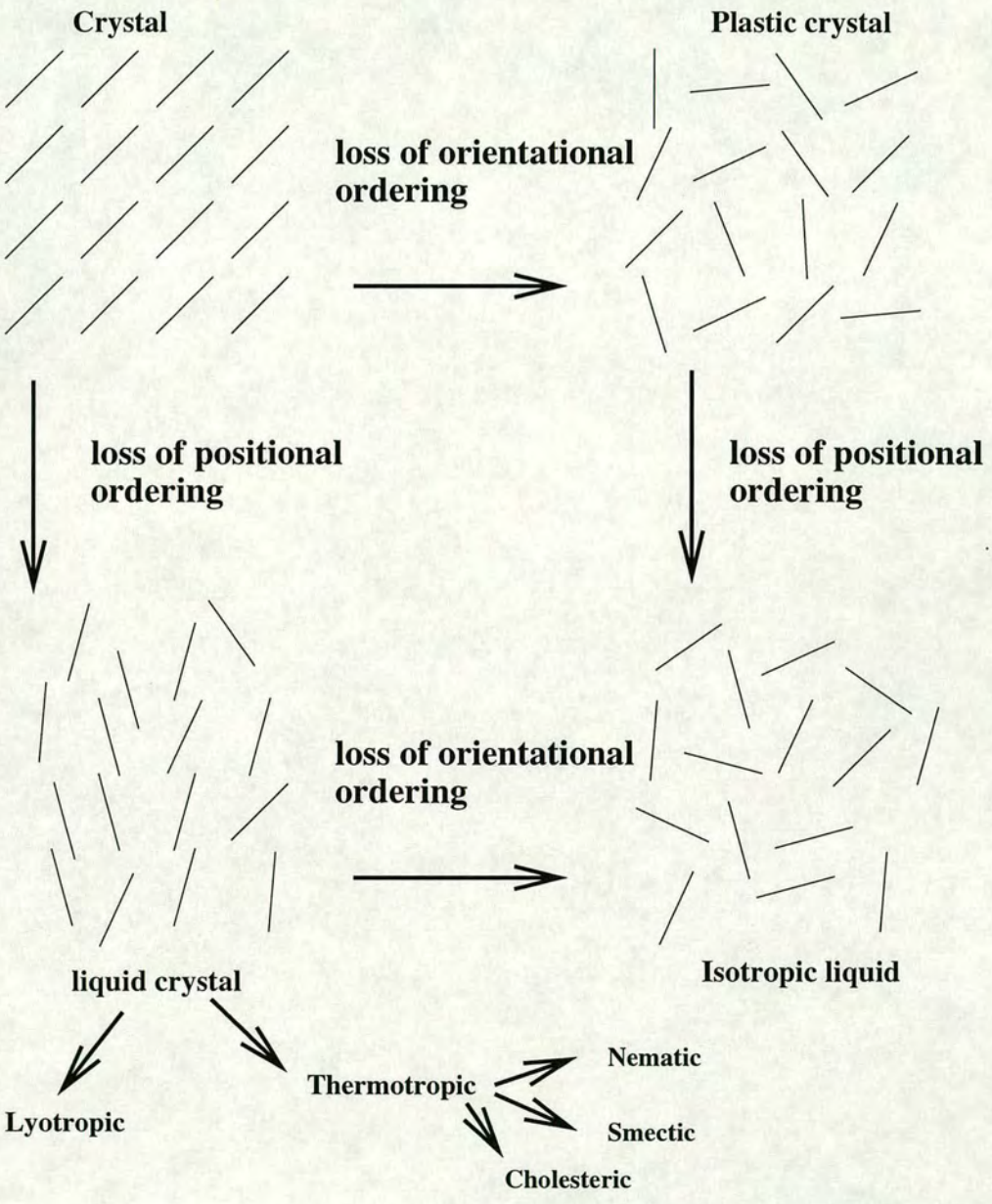

Figure 1.1. The translational and orientational ordering in crystals, liquids and mesophases. Liquid crystals show some degree of average orientational ordering (and in some cases translational as well) even though the crystal lattice has been destroyed.

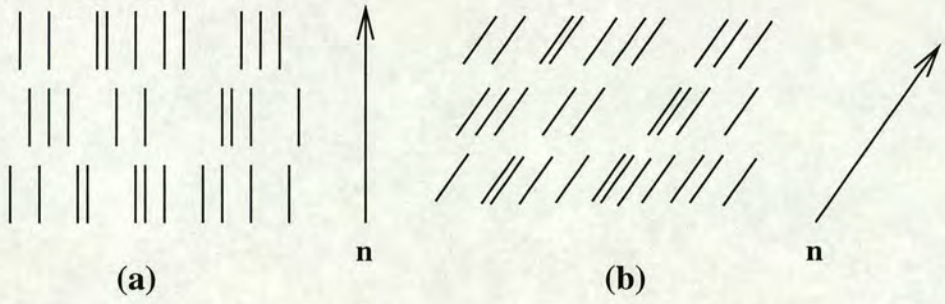

Figure 1.2. Schematic illustration of two types of smectic order: (a) smectic A order; (b) smectic C order.

in space (there is no positional ordering of the centres of mass of the molecules). A chiral nematic mesophase (or cholesteric) is similar to a nematic except that the director has a natural twist with a specific pitch which arises due to either the mesogenic molecule or a dopant material being optically active (not superimposable on their mirror image). A mesogenic molecule can be made optically active simply by substituting a chiral centre into a terminal alkyl tail. The size of the pitch depends on the twisting power of the chiral molecule and for many molecules this pitch is comparable with the wavelength of visible light. Consequently, cholesteric phases appear coloured as selective reflection of the incident white light occurs.

The smectic phase differs from the nematic phase in that it has an additional degree of order. The molecules are grouped together in planes. There exist many different types of smectic phase, from smectic A to smectic I. The two most commonly found phases are smectic A and smectic C, are shown schematically in Figure 1.2 (a) and (b) respectively. Within the layers of a smectic A mesophase the molecules are aligned parallel to the layer normal, whereas in the smectic C mesophase, there is a uniform tilting of the molecular axes with respect to the layer normal. Liquid crystal materials typically show more than one mesophase between the solid and liquid phases. Generally the more ordered the mesophase, the closer it lies to the solid phase in terms of temperature.

Thermotropic liquid crystal materials

The typical thermotropic liquid crystal is rod-like, consisting of two or more aromatic groups (groups are usually *para* to preserve linearity) sometimes connected by a bridging group such as an ester, with simple end terminations such as alkyl tails, CN and NO_2 groups. Typical examples of aromatic groups used are cyclohexane or phenyl groups. Some molecules may also have lateral substituents on them. Thermotropic liquid crystals usually exhibit nematic and smectic mesophases and if optically active give rise to a cholesteric mesophase. However, there is no way of predicting with certainty, whether or not a given molecule will exhibit a liquid crystal mesophase.

The majority of thermotropic liquid crystal mesogens share common structural features. The two most essential features are (1) the mesogens must be elongated and (2) they must have a significant degree of rigidity. Figure 1.3 represent schematically these generalisations in terms of a typical mesogenic molecule. It should be noted however that these are only very general guidelines and even small changes to the molecular structure can alter the liquid crystal properties. The classic example of this is the odd-even effect seen in the cyano-biphenyl (nCB) homologous series (discovered by Gray *et al.* in 1974 [7]), where the nematic-isotropic phase transition temperature changes with the number of carbons, n, in the alkyl tail group. The explanation of this effect depends on the conformational dynamics, as it is proposed that for even values of n the molecules are on average more elongated and therefore more likely to form a nematic phase [3]. Another example of how small changes can alter liquid crystal properties, is the dependence of the optical birefringence Δn, which is the difference between the ordinary and extraordinary refractive indices of the liquid crystal, on the molecular structure. Many nematic materials show a strong Δn as a consequence of the anisotropic polarisability of the molecule (thought to be due to the highly delocalised electrons present on the phenyl groups). It was found that replacement of the phenyl rings with saturated rings such as cyclohexane in the nematogen 5CB causes a lowering

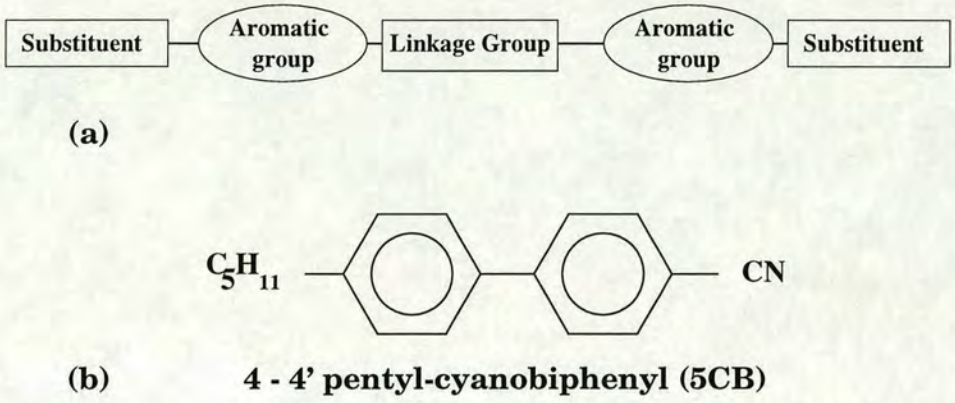

Figure 1.3. Figure (a) is a schematic illustration of the structure of a typical nematic forming molecule, where it can be seen from the structure that the molecule satisfies the requirements of elongation and rigidity. Figure (b) shows the prototypical nematogen (5CB) from the cyano-biphenyl (nCB) homologous series which has no linking group. This molecule has a large permanent dipole located on the CN group [10] and a high level of molecular polarisability which also helps mesophase thermal stability. It also happens to be one of the smallest mesogenic molecules and the first to be engineered with properties appropriate for use in LCDs.

of the birefringence [5]. Many more examples of such structure-property relationships have been discussed by Luckhurst and Gray [2].

1.0.2 Liquid crystal displays

The anisotropic structure of liquid crystals can lead to the anisotropy of certain bulk physical properties, which are uniquely useful in a variety of applications. In particular, recent liquid crystal research and development has been driven by the liquid crystal displays (LCDs) industry in its attempts to produce a flat, light weight and low powered device to replace the cathode ray tube. In order to advance the technology, a more complete understanding of both structure-property relationships and liquid crystal surface interactions is fundamental to the success of many projects. Although there are thousands of molecules that show liquid crystal phases, only a small fraction are suitable for use in LCDs. A device will only function satisfactorily if the liquid crystal material possesses a suitable combination of physical properties. For example, a liquid

crystal developed for use in a device planned to operate over a wide range of temperatures, should exhibit a stable mesophase over the same range of temperatures. This wide range is very difficult to achieve without using mixtures of different mesogenic molecules. Also, the functionality of a LCD is dependent on such quantities as viscosity, elasticity and dielectric properties which influence switching times, contrast ratios and operating voltages [3, 5, 9].

LCDs use electric fields to align the liquid crystal. Upon application of an electric field, the dielectric anisotropy $\Delta\epsilon$ of the material, which is the difference between the dielectric constant parallel to and perpendicular to the director, causes the molecules to align. The strength of the reorientation is related to the sign and magnitude of $\Delta\epsilon$. The $\Delta\epsilon$ may be positive or negative, depending upon the detailed chemical structure of the constituent molecules. Due to the size and complexity of mesogenic molecules, prediction of the dielectric properties is difficult and only a number of empirical relationships exist. Mesogenic molecules with a dipolar group positioned along the molecular axis tend to have strong positive dielectric anisotropies, such as 5CB shown in Figure 1.3 which has a large permanent dipole on the CN group [10]. Liquid crystals such as these generally operate at lower voltages and require less power. For mesogenic molecules without significant polarity the polarisability anisotropy is responsible for $\Delta\epsilon$, which is usually small.

In a LCD, the electric field realigns a liquid crystal from a defined *off* state configuration into a defined field aligned *on* state. The most predominantly used liquid crystals in LCDs are twisted nematics (TN). In a TN device a 90° twist of the nematic director is enforced by confining the liquid crystal material between two glass substrates and imposing surface alignment at each substrate. The orientation of the liquid crystal molecules on the surface is parallel to the substrate (homogeneous alignment). Crossed polarisers are then used to achieve contrast between the on and off states and colour filters to reproduce the colours of the visible spectrum. A more detailed review of LCD technology is given in [11].

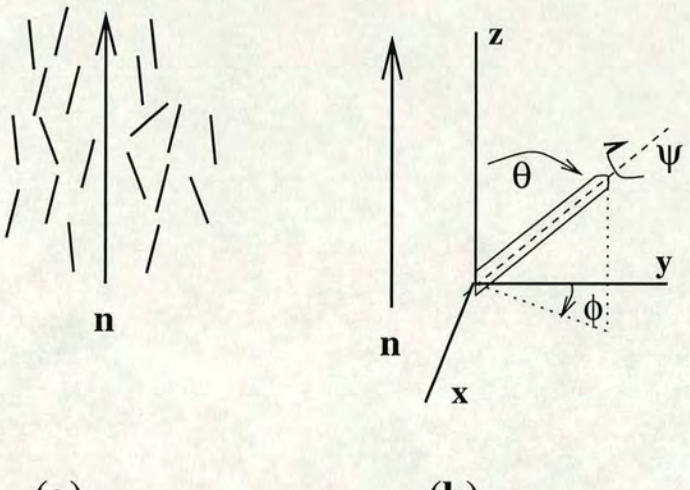

Figure 1.4. Schematic illustration of the (a) structure of a nematic phase (b) the Euler angles required to describe the orientation of a molecule.

Lately, LCD technologies are making use of cholesteric smectic C liquid crystals which exhibit ferroelectric properties. Ferroelectric liquid crystals (FLC's) possess a permanent or spontaneous polarisation when combined with suitable boundary conditions (the surface stabilised effect). For example, in a cholesteric smectic C (S_C^*) phase there is no net polarisation as the director spirals through the material from layer to layer (determined by the helical pitch). However, with the use of boundary conditions the helical pitch can be suppressed and the S_C^* can then show a net polarisation. This polarisation can be reversed with the application of a small d.c. electric field. This allows faster reorientation times (switching times) and higher contrast ratios for LCDs. Displays which use this technology are called Surface Stabilised Ferroelectric Liquid Crystal (SSFLC) displays.

1.1 Molecular properties of nematics

1.1.1 Orientational ordering

Since a nematic liquid crystal (shown schematically in Figure 1.4(a)) has cylindrical symmetry, just one single angle is enough to describe the orientation of the molecule. This angle, θ, is the angle between the director and molecular symmetry axis. In Figure 1.4(b), the director lies along the Z-axis of a fixed coordinate system. If the angles ψ (rotation about the long molecular axis) or ϕ (rotation in the azimuthal direction) were favoured then the symmetry would be lower than cylindrical. At the single molecule level the most complete description of its orientational ordering is provided by the orientational distribution function f(θ), which gives the probability of finding a molecule in a particular orientation. The distribution is normalised such that:

$$\int_0^{\pi} f(\theta) \sin\theta d\theta = 1 \tag{1.1}$$

The orientational distribution function f(θ) can be expanded in a basis of Legendre Polynomials:

$$f(\theta) = \frac{1}{2} \sum_{L(even)} (2L+1) f_L P_L(\cos(\theta)), \tag{1.2}$$

where L is restricted to even values and the expansion coefficients are,

$$f_L = \int_0^{\pi} P_L(\cos(\theta))\, f(\theta)\, \sin(\theta) d\theta. \tag{1.3}$$

These coefficients define the order parameters denoted by $\overline{P}_L$. When there is perfect order they all take the value 1, and the value of 0 for the isotropic phase. The first

three order parameters are

$$\overline{P}_0 = 1 \tag{1.4}$$

$$\overline{P}_2 = (3\overline{\cos^2(\theta)} - 1)/2$$

$$\overline{P}_4 = (35\overline{\cos^4(\theta)} - 30\overline{\cos^2(\theta)} + 3)/8$$

The L=0 term is an additive constant and is therefore neglected. $\overline{P}_2$ is sometimes represented by the symbol S.

Mean field theories of nematics

The distribution function $f(\theta)$ can be described by an effective single-molecule orientational potential function $V(\theta)$, such that:

$$f(\theta) = \frac{exp[-V(\theta)/k_BT]}{Z}, \tag{1.5}$$

where Z is the single molecule partition function,

$$Z = \int exp[-V(\theta)/k_BT]d\theta. \tag{1.6}$$

The potential $V(\theta)$ acts as a potential of mean torque responsible for making the molecules preferentially align with each other. In the late 1950's Maier and Saupe [12] developed a successful mean field theory for $V(\theta)$. They began by first introducing a generalised pair potential V_{12}, which was expanded into a series of spherical harmonics and then averaged to give a single molecule potential function; first over all orientations of the intermolecular vector, then over all orientations of the one molecule relative to the other and finally over all intermolecular separations. Maier and Saupe truncated the single molecule potential at L=2. The potential $V(\theta)$ then became,

$$V(\theta) = -\nu\overline{P}_2P_2(cos\theta) \tag{1.7}$$

where the parameter ν scales the intermolecular interaction. The mean field approximation views each molecule as moving in a field generated by its interaction with all the other molecules, ignoring the fact that the individual behaviour and interactions of the molecules can be widely distributed about the average.

In the original description of their model, Maier and Saupe proposed that it was the long range anisotropic interactions resulting from dispersion forces which were responsible for nematic ordering. However, this assumption was not essential since all that is required to obtain their results is a particular form of the pair potential [2]. The Maier and Saupe theory successfully predicts the existence of orientationally ordered and disordered phases separated by a first order phase transition. $\overline{P}_2$ is predicted to have a universal dependence on reduced temperature with a value at the phase transition of 0.429 which is in good agreement with experiment [13]. However, there are failures of the theory, which are generally reported to be a result of the mean field approximation rather than the form of the inter-molecular potential used [2]. An excellent discussion of issues such as these can be found in [2].

Since this original theory of Maier and Saupe, there have been many studies of mean field theories for nematics. Further work by Straley [14] generalised the Maier-Saupe molecular field expressions [12] to non-axially symmetric molecules by considering the mutually excluded volume between pairs of hard parallelepipeds. There have been other different approaches to parameterise a form of the mean field. Samulski and Dong [15] for example enclosed a molecule in a hypothetical cylindrical constraint and had each atom in the molecule interacting with the nearest point on the cylinder via a Lennard-Jones potential. More discussion relating to mean fields can be found in Chapter 6, where an empirical mean field developed by Ferrarini *et al.* [16], is used to investigate the conformational properties of the molecule 5CB in the nematic phase.

Experimental measurement of nematic ordering

The function $f(\theta)$ provides a complete description of the ordering distribution at the single molecule level. In principle $f(\theta)$ can be measured from x-ray and neutron scattering experiments but in practice this is difficult. Interpretation of the results requires major assumptions and can often only be used to study glassy phases [3]. Therefore most research has instead concentrated on determining orientational order parameters $\overline{P}_n$. The order parameter $\overline{P}_2$ can be found from the splitting of the spectral lines in NMR spectra [17]. Deuterium NMR spectroscopy is most widely used. The splitting is the result of the interaction between the quadrupole moment of the deuteron and the electric field gradient which it experiences. The splitting is proportional to the angle between the static magnetic field and the carbon deuteron (C-D) bond. Assuming that the interaction tensor for deuterons is cylindrically symmetric (with symmetry axis parallel to the C-D bond) the deuterium NMR spectrum then consists of a pair of lines where the splitting changes according to

$$\Delta\tilde{\nu} = (3/2)q_{CD}S_{CD}, \tag{1.8}$$

where S_{CD} is the order parameter $\overline{P}_2$ for the C-D bond direction. The tilde indicates that the change is measured in the liquid crystalline phase, where the splitting is an average of the splittings over all orientations and conformations. The quadrupolar constant q_{CD} along the C-D direction can be determined by measuring the angular dependence of the splitting from single crystal experiments and is reasonably transferable between compounds [17].

In the discussion so far, the order parameters were defined using the assumption that the molecules effectively act as rigid rods with the nematic phase being cylindrically symmetric. In many instances however, the molecules are more lath-like (biaxial) and do not behave as rigid rods. In those cases this model is inadequate and it is then necessary to use the Saupe ordering matrix, which can describe the orientational order

of biaxial molecules. The elements of the 3×3 Saupe ordering matrix can be written as

$$S_{ij} = (3\overline{\cos\theta_i \cos\theta_j} - \delta_{ij})/2 \tag{1.9}$$

where δ_{ij} is the Kronecker delta function and θ_i and θ_j are the angles which the molecular symmetry axis makes with an orthogonal axis system xyz. The matrix contains nine elements and is real, symmetric and traceless. It can therefore be diagonalised and since it is traceless there are only two independent principal components. These are usually defined as the largest order parameter S_{zz} and the biaxiality $(S_{xx} - S_{yy})$.

1.2 Computer simulations of liquid crystals

1.2.1 Hard particle simulations

The first attempt at modelling the nature of the anisotropic interactions responsible for orientational ordering was developed by Onsager in 1949 [18]. He proposed a simple "hard rod" model for the behaviour of liquid crystals, suggesting that it was the short range steric interactions due to the impenetrability of the molecules that were primarily responsible for the ordering. He showed that a system of hard rods without any attractive interactions, can have a first-order transition from the isotropic to nematic phase as the density was increased. The loss of entropy as a result of the orientational order was offset by the gain in translational entropy since parallel rods could slide past each other more easily than if randomly orientated. This was the first entropically driven phase transition proposed for liquid crystals.

The original calculations by Onsager are only appropriate in the limit where the aspect ratio of length over diameter goes to infinity and so cannot be related to typical mesogenic molecules whose aspect ratios range between 3 and 30. However, computer

simulations based on the hard anisotropic particle model [19, 20, 21, 22] have convincingly proved that entropically driven phase transitions between isotropic and nematic phases do exist for aspect ratios larger than 3 and less than $\frac{1}{3}$. The shape of the anisotropic particle plays an important role in determining the type of phase simulated. Simulations involving spherocylinders usually exhibit a smectic phase, whereas simulations involving oblate (disc-like) and prolate ellipsoids of revolution (a spheroid with two transverse axes of equal length and a unique symmetry axis) form columnar and nematic phases respectively.

These models are highly idealised and they represent the simplest possible level of inter-molecular interactions, where density is the only thermodynamic variable. However, they have had success in modelling phase diagrams and also provided insight into the orientational mechanism. Progress is currently being made in using biaxial shapes, which are spheroids with three axes all of different lengths. Studies by Allen *et al.* [23] have shown that the isotropic-nematic transition is weakened by a modest degree of molecular biaxiality. To perform more realistic studies it is becoming increasingly clear that certain liquid crystalline properties such as molecular ordering and phase stability require the modelling of more detailed chemical interactions such as molecular flexibility [24].

1.2.2 The Gay-Berne potential

The need to explore the effects of generic long range interactions on phase stability has led to development of liquid crystal models based on highly symmetrical but anisotropic soft-core potentials. The standard among these anisotropic pair potentials is the Gay-Berne (GB) [25] which has been used in many molecular dynamics (MD) simulations to study the phase behaviour of thermotropic liquid crystals [26, 27]. The GB potential models mesogenic molecules as simple rigid units interacting via attractive as well as repulsive forces. It is an extension of the Berne-Pechukas [28] potential, and is regarded as an anisotropic and shifted version of the Lennard-Jones 6-12 interaction where the

strength ϵ, and the range parameter σ, depend on the intermolecular vector of the two particles and their orientation (attractive forces greater when molecules are side by side rather than end to end).

As is the case for real molecules, GB simulations [26] have predicted the nematic-isotropic transition at constant volume to be also thermally driven (although this does involve having the correct number density of particles emphasising the important role played by repulsive forces). Other GB simulations have also exhibited smectic liquid crystal phases [27] in addition to the nematic. GB simulations are not as computationally demanding as atomistic simulations and hence allow far greater overall simulation times. Luckhurst and Simmonds [29] for example used the single-site GB potential to determine the relative importance of short range anisotropic repulsive and long range attractive interactions in various phases. Their results indicated that the structures of the isotropic and nematic phases were dominated by short range anisotropic forces whereas the stability of the smectic A was found to be critically dependent upon the anisotropy of the attractive forces.

Luckhurst and Simmonds [29] parameterised the GB potential by taking a Boltzmann weighted average of the interactions between a pair of molecules. The interactions were calculated by the sum of an atom centred Lennard-Jones potential, after which a biaxial averaging procedure was performed as GB units are typically uniaxial. A description of this procedure can be found in [29]. The procedure allows for an objective means to parameterise a potential specific to molecules of various shapes. However, it has been found that the ratios of the GB potential well depths for certain inter-molecular configurations are often too large using this method. Cleaver et al [30] states that this is due to neglecting molecular flexibility and important factors such as quadrupolar interactions. Recently a biaxial version of the GB potential has been proposed [31]. Also the GB potential has been extended to model interactions between non-equivalent particles [30] and implemented in multisite models (assemblies of identical GB units) [32].

1.2.3 Atomistic approaches

At present, simulations based on detailed atom-atom potentials are very demanding in terms of computer time. However, there have been a few simulations using realistic models [33, 34, 35] and the field is likely to expand rapidly with the growth of faster computer hardware. In atomistic simulations each molecule is represented by a number of bonded atom-based Lennard-Jones interaction sites. Intra-molecular flexibility is introduced through the use of a standard molecular mechanics force field. More details pertaining to force fields can be found in Chapter 4. The goal of such simulations is to realistically model the properties of the real liquid crystals, and thereby gain a detailed picture of the microscopic structure and dynamics.

An atomistic simulation, performed by Wilson and Allen on 128 molecules of 4-(*trans*-4-n-pentylcyclohexyl)cyclohexylcarbonitrile (CCH5) [33], was able to indicate phase stability at three state points; a temperature of 350K at which a nematic phase was stable with order parameter $\overline{P_2}$= 0.62, 370K at which the nematic order parameter was stable at $\overline{P_2}$= 0.38, and 390K where the pretransitional region of the isotropic phase was seen. The simulation also yielded information on the variation of the dihedral angle distributions at the different temperatures and found that in going from the isotropic to the nematic there was a quenching of the *gauche* conformers of the tail. Another atomistic simulation by Komolkin *et al.* [34], investigated the conformational distributions of the alkyl tail in 5CB. Two simulations were performed; a united atom (UA) simulation where the CH, CH_2 and CH_3 groups were treated as single interaction sites, and a full atom (FA) simulation. The UA simulation was found to give reasonable predictions of the conformational distributions of the tail, but an incorrect estimation of the torsional angle between the phenyl rings. The FA simulation was found to give a reasonable prediction of this torsional angle, but did not correctly predict the conformations of the alkyl tail.

Kromer *et al.* [36] performed an atomistic simulation on 4-(*trans*-4-n-pentylcyclohexyl)

benzonitril (PCH-5). They were able to give a detailed description of the microscopic structure and anisotropic partial diffusion behaviour, which compared well with experimental results. However, the intra-molecular flexibility and the distribution of partial charges were found not to agree with experimental observations. It was found that force field rendered the molecules too rigid in comparison with NMR data. It was also found that the microscopic structure was highly dependent on the dipole of the cyano group. This important finding further emphasises the important contribution that first principles calculations can have in determining the correct values for these important quantities. A number of other studies have focused on the the cyanobiphenyls, performing molecular dynamics studies of their bulk [37] and adsorption [38] behaviour, using a number of different interaction potentials.

Chapter 2

First Principles Total Energy Calculations

2.1 Introduction

The fundamental quantum-mechanical equations that govern the behaviour of electrons and atomic nuclei are well known and *in principle* allow us to calculate the properties of materials without the use of adjustable or empirical parameters. However, in practice this is an impossible task to perform, as the ground-state wavefunction of a typical molecule (which represents a large assembly of interacting electrons and nuclei), depends on the coordinates of all the electrons together in an inconceivably complicated way. Theoretical approaches therefore make approximations and incur a consequent loss of accuracy, the degree of which depends on the ability of the approximations to adequately describe the physical features involved at the quantum mechanical level.

The first principles calculations performed in this thesis are based on the Kohn-Sham Hamiltonian [39]. Kohn and Sham developed the density functional theory (DFT) of Hohenberg and Kohn [40] to deal with the many-electron problem by mapping a system of strongly interacting electrons onto a series of single electron equations where each particle is moving in an effective potential. The many body effects

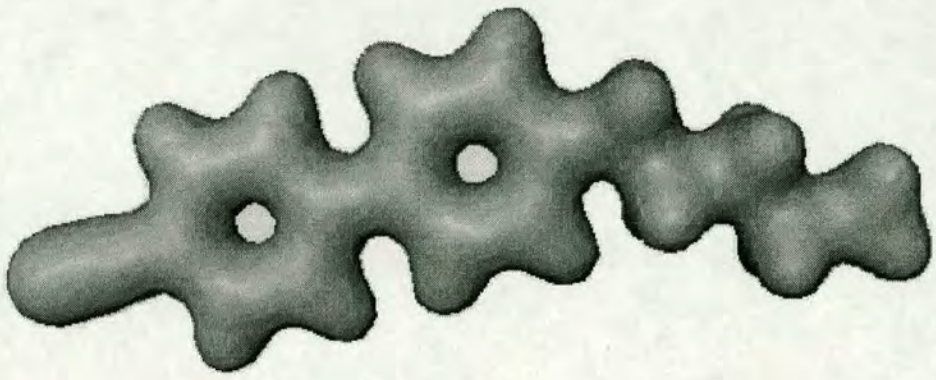

Figure 2.1. Calculated valence charge distribution for the 38 atom molecule 5CB as reconstructed from the electron wavefunctions corresponding to occupied bands. The two phenyl groups, hydrocarbon chain and cyano end group are clearly visible. The charge density is evaluated on a discrete grid with a basis set containing 2.5 million plane waves. The entire calculation (including structural relaxation) took 6 hours on 128 nodes of the Edinburgh CRAY-T3D.

of exchange and correlation are included via density approximations which assume exchange-correlation interactions are local to a small volume. The core electrons and the strong nuclear potentials are removed and replaced with pseudopotentials, since the physical properties of molecules are primarily dependent on the valence electrons. A plane wave basis set is used for the expansion of the electron wavefunction. The variational principle and function minimisation procedures are then used to locate the ground state wavefunction.

The conventional method for accurately calculating the total energy of a molecule is to first perform a Hartree-Fock (HF) calculation followed by a calculation of the correlation energy. The HF computational cost formally scales as N^4, where N is the number of basis functions used in the expansion of the orbitals. If more accurate results are sought and correlation effects are included via for example, perturbation theory or configuration interactions, then the cost can scale as much as N^7. Methods based on DFT are receiving a significant amount of attention since the computational effort scales between N^2 and N^3. Its efficient scaling opens exciting opportunities for the study of large and complex molecular systems, previously considered out of reach

for conventional *ab initio* calculations. This chapter begins with a brief description of the earlier approximations and conventional computational chemistry methods, before giving a description of the techniques used throughout this thesis. A more detailed review of these techniques can be found elsewhere [41, 42, 43].

2.1.1 Earlier approximations

As already stated, calculating of the total energy of a many-electron system is a complicated problem to which solutions can only be obtained using physical approximations. The main difficulty in the calculation arises because of the strength of the electron-electron interactions. It is therefore necessary to introduce approximations to make the calculation of the wavefunction feasible. This Section will give a brief description of earlier approximations made to solve this many-electron problem and a description of the important physical features omitted from these theories.

The full Hamiltonian for a general polyatomic molecule with N_i electrons at positions $\mathbf{r_i}$ and N_I nuclei at positions $\mathbf{R_I}$ with atomic numbers Z_I is:

$$H = -\sum_{i=1}^{N_i} \frac{\hbar^2}{2m_e} {\nabla_i}^2 - \sum_{I=1}^{N_I} \frac{\hbar^2}{2m_I} {\nabla_I}^2 - \sum_{i=1}^{N_i}\sum_{I=1}^{N_I} \frac{e^2 Z_I}{4\pi\epsilon_o |\mathbf{r_i} - \mathbf{R_I}|} + \frac{1}{2}\sum_{i=1}^{N_i}\sum_{i'=1,i'\neq i}^{N_i} \frac{e^2}{4\pi\epsilon_o |\mathbf{r_i} - \mathbf{r_{i'}}|} + \frac{1}{2}\sum_{I=1}^{N_I}\sum_{I'=1,I'\neq I}^{N_I} \frac{e^2 Z_I Z_{I'}}{4\pi\epsilon_o |\mathbf{R_I} - \mathbf{R_{I'}}|} \tag{2.1}$$

The terms are (from left to right); the kinetic energy of the electrons, the kinetic energy of the nuclei, the potential energy between the electron i and nucleus I, the potential energy between electron i and i' and the potential energy between nucleus I and nucleus I'.

Arguably the most important approximation used to determine the solution to this Hamiltonian is the Born-Oppenheimer (BO) approximation. Since the electron speeds are so much greater than nuclear speeds then the BO approximation considers the

nuclei to be fixed in space and the electrons to move in the electrostatic field they generate. The nuclear kinetic energy is therefore zero and since the nuclei positions R_I are static, the nuclear repulsive potential is simply a constant. This potential is calculated by the Ewald sum which is discussed in Section 2.7.

The properties of a system can now be described by an N-electron wavefunction $\Psi(\mathbf{r_1}, \mathbf{r_2}, ..., \mathbf{r_N})$ obtained from the N-electron Schrödinger equation:

$$H\Psi = E\Psi \tag{2.2}$$

where the Hamiltonian describing the interaction of electron and nuclei is now

$$H = \sum_{i=1}^{N_i} \left(-\frac{\hbar^2}{2m_e} {\nabla_i}^2 - \sum_{I=1}^{N_I} \frac{e^2 Z_I}{4\pi\epsilon_o |\mathbf{r_i} - \mathbf{R_I}|} + \frac{1}{2} \sum_{i'=1, i' \neq i}^{N_i} \frac{e^2}{4\pi\epsilon_o |\mathbf{r_i} - \mathbf{r_i'}|} \right). \tag{2.3}$$

The first term is the kinetic energy operator, the second describes the interaction of the electrons with the fixed configuration of nuclei R_I and the third term represents the electron-electron interactions. It was not known what functional form the wavefunction should take until Hartree in 1928 suggested a mean-field approach [44]. In Hartree's treatment of the many-electron system each electron is imagined to move in an average field of the other electrons. Electrons are treated as independent non-interacting particles with wavefunctions which are solutions of a one-electron Schrödinger equation. The wavefunction Ψ is considered as a product of single-particle functions:

$$\Psi(\mathbf{r_1}, \mathbf{r_2}, ..., \mathbf{r_N}) = \psi_1(\mathbf{r_1})\psi_2(\mathbf{r_2})...\psi_N(\mathbf{r_N}), \tag{2.4}$$

where each of the functions $\psi_i(\mathbf{r_i})$ satisfies a one-electron Schrödinger equation of the form:

$$-\frac{\hbar^2}{2m}\nabla^2\psi_i(\mathbf{r}) + V(\mathbf{r})\psi_i(\mathbf{r}) = \epsilon_i\psi_i(\mathbf{r}). \tag{2.5}$$

The first term is now the one-electron kinetic energy and $V(\mathbf{r})$ is the mean-field potential in which the electron is moving. $V(\mathbf{r})$ is composed of two parts, the nuclear potential for the ion-electron interactions and the Hartree potential for the electron-electron interactions. The nuclear potential (considered an external field) V_{ext} is:

$$V_{ext} = -\sum_I \frac{Z_I e^2}{4\pi\epsilon_o |\mathbf{r_i} - \mathbf{R_I}|}. \tag{2.6}$$

The Hartree potential gives the interaction of each electron with the electron density $n(\mathbf{r}')$:

$$V_H = \int \frac{n(\mathbf{r}')e^2}{4\pi\epsilon_o |\mathbf{r} - \mathbf{r}'|} dr' \tag{2.7}$$

The set of equations Eqn. 2.5 (there is one for each occupied one-electron level $\psi_i(\mathbf{r})$) is known as the Hartree equations. These equations can be solved self-consistently to determine the single particle functions $\psi_i(\mathbf{r})$ and corresponding eigenvalues ϵ_i. However there are several important features of electron-electron interactions that are absent in the Hartree approximation. The wavefunction is incompatible with the Pauli exclusion principle which demands the N-body wavefunction to be anti-symmetric under the interchange of two electrons.

The Pauli exclusion principle can be incorporated by replacing the product wave-function by a single determinantal function, often called a 'configuration'. This wave-function is in fact a Slater determinant of one-electron wavefunctions which is a linear combination of all possible Hartree wavefunctions obtainable from permutations of $\mathbf{r_i}$ added together with weights ± 1 so as to guarantee the anti-symmetric condition:

$$\Psi(\mathbf{r_1}, ..., \mathbf{r_a}, ..., \mathbf{r_b}, ..., \mathbf{r_N}) = -\Psi(\mathbf{r_1}, ..., \mathbf{r_b}, ..., \mathbf{r_a}, ..., \mathbf{r_N}). \tag{2.8}$$

Evaluating the ground state energy using this correct anti-symmetric wavefunction

leads to a generalisation of the Hartree equations known as the Hartree-Fock equations:

$$-\frac{\hbar^2}{2m}\nabla^2\psi_i(\mathbf{r}) + V_{ext}(\mathbf{r}) + V_H(\mathbf{r})\psi_i(\mathbf{r}) + \sum_j \int \frac{e^2}{4\pi\epsilon_0|\mathbf{r}-\mathbf{r}'|} d\mathbf{r}\ \psi^*{}_j(\mathbf{r}')\psi_i(\mathbf{r}')\psi_j(\mathbf{r})\psi_i^*(\mathbf{r}) = \epsilon_i\psi_i(\mathbf{r}). \quad (2.9)$$

These equations differ from the Hartree equations 2.5 by an additional term on the left hand side, which term arises from the exclusion principle. This term describes the exchange interaction, which produces a repulsion between electrons with parallel spins.

However, even with the exchange term fully accounted for, in many instances the total energies are still not accurate enough. Until now the motion of the electrons has been considered independent. The wavefunction expressed in Eqn. 2.4 is a product of single-particle functions. This assumption ignored the fact that each electron in the system repels the other electrons due to classical electrostatic repulsion interactions. Their motion is correlated. The result of these many-body correlation effects, in addition to exchange interactions, is that there is a depletion in the probability of finding an electron near to a given electron. This depletion is called the exchange-correlation hole. The hole has the effect of screening the electrons from each other, such that when viewed from a distance the electron and hole appear neutral. The electron and hole are inseparable and are called a quasiparticle [41]. Section 2.3 describes the approximation to exchange and correlation effects used in this work.

2.1.2 Conventional ab initio methods

This Section gives a brief summary of the conventional *ab initio* methods used in computational chemistry. There is vast literature available which gives a more detailed description [45, 46, 47]. Although Hartree-Fock calculations (often referred to as 'self-consistent field' (SCF)) have remarkable value in molecular electronic structure investigations, they are not complete in their description since they ignore correlation effects. In general, conventional methods make use of configuration mixing as a route

to incorporating electron correlation. The 'configuration' with the lowest energy is only one of many possible configurations with comparable energies. A combination of these configurations can improve the energy by improving the wavefunction. This is known as 'configuration mixing', which in principle can lead to the exact wavefunction if all permutations are included, although the numerical effort increases tremendously. By mixing configurations fractional populations of orbitals is allowed.

A configuration is described by the number of differing spin orbitals it has in comparison with a reference configuration (normally the SCF). There are configurations which have single substitutions (i.e. differing by a single spin orbital), double substitutions and so on. Single capital letters (i.e. S,D,T..) are used to indicate the level of substitution in a correlated wavefunction. Accuracy generally improves as the number of substitutions increase; however, it is the double substitutions which have the largest correlation effects. This is due to the fact that the Hamiltonian has only one and two body operators and hence triple substitutions mix only because of their interactions with doubly or singly substituted configurations. Also it should be noted that single substitutions have no effect and yield the SCF results (which is correct to first order).

There are several methods available for determining the correct mixing of configurations that gives a good description of electron correlation. The most direct way is to let the set of expansion coefficients for the configurations (i.e. single or double) be variational parameters. This approach is called configuration interaction (CI). The coupled cluster (CC) approach is similar, except that it uses an exponential substitution operator to generate the correlated wavefunction. Another way of mixing together the configurations is to define the difference between the true Hamiltonian and the SCF Hamiltonian as a perturbation. Møller and Plesset [48] (MP) were first to identify perturbational calculations which have become know as MPn (where n=2,3,4,5.., and is the perturbation order.) Once again there is no level one here as the SCF energy is correct to the first order.

There are other *ab initio* methods in use that are hybrids of both HF and DFT.

The simplest methods calculate the HF energy and electron density, from which the correlation energy is determined using a correlation functional. They represent a sizable reduction in computational cost compared to CI or CC methods and have been shown by several investigations to produce molecular properties which are highly accurate [44]. The exchange and correlation functional used in these studies is the B-LYP functional which is typically a combination of the Becke [49] exchange and Lee, Yang and Parr [50] correlation functionals.

When calculating the wavefunction it is important, whatever technique described above is used, that a suitable basis set is chosen. An early approach to basis set construction was to fit a Slater-type atomic orbital (STO) with a number of n Gaussian functions. These were called STO-nG and were not very accurate. The quality improved when more than one STO was used to fit each orbital, and it was proposed then that the inner and outer electron shells should be modelled differently. Pople *et al.* [45] introduced n-31G basis sets where inner shell orbitals were modelled with one STO-nG and the outer shell orbitals with two STO-nG's. These were much better than the original STO-G sets. For example the 6-31G basis set has the inner shell modelled with a STO-6G and the outer shell modelled with one STO-3G and STO-1G. Added on to these basis sets can be d-type functions (denoted by single *) for the heavier atoms and p-type functions (denoted by **) for hydrogen and helium. Generally the more complicated the basis set, higher is the accuracy achieved.

2.2 Density functional theory

DFT expresses the problem of dealing with a system of N-interacting electrons in an external potential $V_{ext}(\mathbf{r})$ in terms of the electron density distribution, $n(\mathbf{r})$ and a universal functional of the density $F[n(\mathbf{r})]$. It was originally developed by Hohenberg and Kohn [40] who proved that the ground state energy E_G of a system of interacting electrons acted on by some external potential V_{ext} is a unique functional of the electron

density $n(\mathbf{r})$. The functional can be written as:

$$E[n(\mathbf{r})] = F[n(\mathbf{r})] + \int V_{ext}(\mathbf{r})n(\mathbf{r})d\mathbf{r} \tag{2.10}$$

where $F[n(\mathbf{r})]$ is a universal (independent of V_{ext} and N) functional of the density $n(\mathbf{r})$. $F[n(\mathbf{r})]$ is the sum of the kinetic energy of the electrons and their mutual coulomb interaction energy. An explicit form of this functional is not known.

2.2.1 The Kohn-Sham scheme

Kohn and Sham [39] separated the functional $F[n(\mathbf{r})]$ into three parts so that $E[n(\mathbf{r})]$ became:

$$E[n(\mathbf{r})] = T[n(\mathbf{r})] + E_H[n(\mathbf{r})] + E_{xc}[n(\mathbf{r})] + \int V_{ext}(\mathbf{r})n(\mathbf{r})d\mathbf{r} \tag{2.11}$$

where the first, second and third terms represent the kinetic energy, the Hartree energy and the exchange-correlation energy respectively. The last term is the external potential which in this case is the Coulomb potential due to the ions. Only the second term $E_H[n(\mathbf{r})]$ can be expressed in an explicit form:

$$E_H[n(\mathbf{r})] = \frac{1}{2}\int\int \frac{e^2 n(\mathbf{r})n(\mathbf{r}')}{4\pi\epsilon_0|\mathbf{r}-\mathbf{r}'|}d^3\mathbf{r}d^3\mathbf{r}' \tag{2.12}$$

In analogy with Hartree's treatment, Kohn and Sham then defined the kinetic energy T[n(**r**)] as the energy of a system of non-interacting electrons. The last term $E_{xc}[n(\mathbf{r})]$ was then defined to be the part of $F[n(\mathbf{r})]$ not included in the $T[n(\mathbf{r})]$ and $E_H[n(\mathbf{r})]$, and therefore includes the exchange and correlation effects. Kohn and Sham were then able to map the many body problem onto an exactly equivalent set of self consistent one-electron equations:

$$\left\{-\frac{\hbar^2}{2m}\nabla^2 + V_{eff}(\mathbf{r})\right\}\psi_i(\mathbf{r}) = \epsilon_i\psi_i(\mathbf{r}) \tag{2.13}$$

These equations called the Kohn-Sham equations represent the electrons as moving in an effective field:

$$V_{eff}(\mathbf{r}) = V_{ext}(\mathbf{r}) + \int \frac{e^2 n(\mathbf{r}')}{4\pi\epsilon_0 |\mathbf{r} - \mathbf{r}'|} d\mathbf{r}' + \mu_{xc}(\mathbf{r}). \tag{2.14}$$

Eqn. 2.13 can be solved using the variational principle and efficient minimisation procedures to locate the ground state. The electron density may be found from the individual wavefunctions:

$$n(\mathbf{r}) = \sum_{i=1}^{N} \psi_i^*(\mathbf{r})\psi_i(\mathbf{r}) \tag{2.15}$$

The Kohn-Sham equations and corresponding Kohn-Sham single-particle orbitals are just the components of the total energy and density distribution required to work out the density approximation to the exchange and correlation. They themselves do not have physical significance, they are only used to achieve self-consistency. The fact that the problem has been formulated in terms of independent particles does not mean correlations have been ignored.

2.3 Electron-electron interactions: LDA and GGA

From the solution of the single particle equations 2.13 it is possible to determine the total energy and ground state of a system of electrons and nuclei. In fact, in principle, it is possible to calculate the exact total energy if exact form of the exchange-correlation potential functional is known. However since the exact form is not known approximations are unavoidable.

The local density approximation (LDA) was first proposed by Kohn and Sham [39] and involves the following integral:

$$E_{xc}^{LDA}[n(\mathbf{r})] = \int n(\mathbf{r})\mathcal{E}_{xc}(n(\mathbf{r}))d\mathbf{r} \tag{2.16}$$

where $\mathcal{E}_{xc}(n(\mathbf{r}))$ is the exchange-correlation potential. The LDA assumes that the exchange-correlation energy per electron at a point $\mathbf{r}$ to be that of a homogeneous electron gas which has the same electron density $n(\mathbf{r})$ (i.e. $\mathcal{E}_{xc}(\mathbf{r}) = \mathcal{E}_{xc}^{hom}(\mathbf{r})$). In their original work Kohn and Sham did not recommend the application of LDA to molecules and solids. They felt that the highly varying charge densities may not be adequately dealt with using a local approximation. In fact they comment in their paper [39] that they "do not expect an accurate description of chemical binding". In light of this comment and the inexact nature of LDA it is surprising that it has performed so well. This achievement can be partly attributed to the fact that LDA satisfies the *correct sum rule* for the exchange-correlation hole [51]. As described earlier the exchange-correlation hole refers to the area around an electron where other electrons are excluded from entering due to the Pauli exclusion principle and correlation effects. If the amount of negative charge excluded is equal to the charge of one electron, then the correct sum rule is achieved. In LDA the shape of this hole does not depend on the spin type of the interacting electrons.

Parameterisations of the LDA are based on Monte Carlo simulations of the free electron gas by Ceperley and Alder [52]. They solved the many-particle wave function for electron gases of different densities using Quantum Monte Carlo (QMC) simulations. There were several early parameterisations of which the one by Perdew and Zunger [53] was most commonly used. By interpolating between the different densities they parameterised the LDA using only four variables. Initial attempts to improve on LDA failed generally because the improvements did not adhere to the correct sum rule. However, recently more sophisticated schemes have been developed which do adhere to the correct sum rule and are able to provide non-local corrections. The generalised gradient approximation (GGA) [54] allows some degree of non-locality to be introduced by taking the exchange-correlation energy as a functional of the local electron density and also its gradient. They have been shown to improve upon LDA [55]. Figure 2.2 illustrates some of the points mentioned in this section.

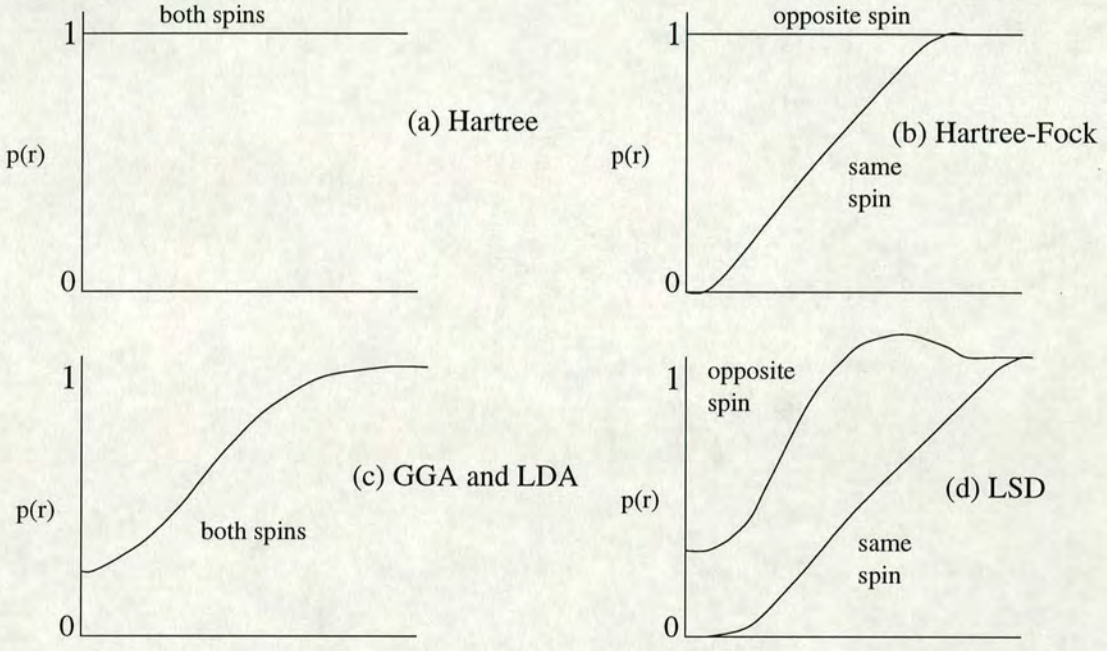

Figure 2.2. Figures (a) to (d) illustrate the probability distribution for N-1 electrons using the different exchange-correlation schemes. The x-axis represents distance r from an electron of some spin situated at r=0 while the y-axis gives the probability normalised such that $p(r) \rightarrow 1$ as $r \rightarrow \infty$. Within the Hartree approximation (shown in Figure (a)), the electrons move in a mean field and are independent of each other. The Hartree-Fock approximation (Figure (b)) however includes the exchange interaction for electrons of similar spin. The reduction in density at r=0 shown on the curve for electrons of the same spin is referred to as the exchange hole. The LDA and GGA approximations (Figure (c)) include correlation and act on all electrons irrespective of spin. Finally Figure (d) shows the local spin density approximation (LSD) which allows differently shaped holes for electrons of equal and opposite spins. The GGA and LDA are spin averages of the LSD. This Figure is after Schlüter and Sham [56].

2.4 Ion-electron interactions

While it is feasible to treat all the electrons in a system explicitly it can be computationally expensive. In the core region where the potential is strong, the core electrons are tightly bound and the valence electrons exhibit rapid oscillations (reflecting the high kinetic energy of these electrons near the nucleus). The wavefunctions for these electrons require an enormous number of plane waves. It is well known however that the physical and chemical nature of atoms in materials is determined mainly by the valence electrons. Material properties are governed by the formation of the bonding and anti-bonding valence orbitals and the distribution of the valence electrons in these orbitals. The core electrons are not affected by the environment the atom is in. Therefore it is reasonable that only the valence electrons need to be treated explicitly and that the core electrons should be accounted for in some other way. This is achieved by grouping the core electrons with the nucleus to act as an ion, whose potential exerted on the valence electrons is generally treated by means of a effective potential, usually referred to as a pseudopotential [57].

Norm conserving pseudopotentials and transferability

A pseudopotential modifies the potential felt by the valence electrons in the core region but must be able to describe the salient features of the valence electrons by preserving, as exactly as possible, the valence orbital structure. This is achieved by ensuring that the pseudopotential generates an identical charge density outside the core radius r_c to that of an all-electron calculation. For example if the exchange-correlation energy is to be obtained accurately it is necessary that outside the core region the pseudo-wavefunction (ps) ψ^{ps} and all electron (ae) wavefunction ψ^{ae} be identical in their spatial dependencies and magnitudes ($\psi^{ps} = \psi^{ae}$ for $r > r_c$). Only then will they both generate identical charge densities and estimates of exchange-correlation energy. The requirement is called *norm conservation* [42]. It can be achieved by adjusting the

pseudopotential to ensure that the integrals of the squared amplitudes of the real and pseudowavefunctions inside the core region are identical [41] :

$$\int_0^{r_c} |\psi^{ae}(r)|^2 r^2 d^3r = \int_0^{r_c} |\psi^{ps}(r)|^2 r^2 d^3r. \tag{2.17}$$

Although this condition arises from considering norm conservation, it also appears when considering transferability of pseudopotentials [58]. It was found that the transferability of the pseudopotential from the atom to molecular environment, is dependent on the ability of the pseudopotential to have the correct scattering properties, which in turn is ensured by the norm conservation condition of Eqn. 2.17.

2.4.1 Generation of pseudopotentials

Although at first they were generated from experimental data [57], pseudopotentials are now generated from first principles [59, 60, 61]. The potential is constructed such that for a given chemical element it should reproduce the properties of the valence states of the free atom obtained from an all electron calculation. In practice the construction is performed by using an assumed functional form of the pseudopotential which is then parameterised such that the conditions discussed in the previous Section are fulfilled. The construction of the pseudopotential is often performed separately for each angular momentum quantum number l component of the pseudo-wavefunction. These pseudopotentials that act differently depending on l are called non-local (NL). The general from of a NL pseudopotential is:

$$V_{NL} = \sum_{lm} |Y_{lm} > V_l < Y_{lm}| \tag{2.18}$$

where the spherical harmonics Y_{lm} project out each angular momentum component. V_l is the pseudopotential for angular momentum l and the operator has the effect of decomposing (projection operator) the wavefunction into spherical harmonics which are

then multiplied by the relevant V_l. However this form of the pseudopotential requires the projection operators to be used for each plane wave in the simulation and requires many integrals.

A pseudopotential that uses the same potential for all the angular momentum components of the wavefunction is called a local pseudopotential, and is a function only of the distance from the nucleus. Although they are computationally more efficient than non-local pseudopotentials they are not as reliable. Kleinman and Bylander [62] introduced a method of splitting the pseudopotential into local and non-local parts to reduce the number of integrals requiring to be evaluated while maintaining reliability. The pseudopotentials used in this thesis are based on their method. Figure 2.3 shows schematically both the all atom potential and the corresponding pseudopotential. The all electron and pseudo wavefunctions are also shown.

Optimisation of pseudopotentials

An important consideration when generating pseudopotentials is to achieve accuracy as well as efficiency during computation. The smoothness or *softness* of a pseudopotential determines the number of plane waves required in the expansion. It must eliminate rapid oscillations of the valence wavefunction in the core region by having no nodes inside r_c (oscillations shown by all-electron eigenfunctions). However, the shape also determines the accuracy of a pseudopotential, which is measured by the agreement between the logarithmic derivatives of the pseudo and all electron wavefunctions in a certain energy range (equivalent to the characterisation of the scattering properties of a pseudopotential in terms of phase shifts for different incoming waves [61]). Flexible schemes have been developed to generate quickly and systematically new pseudopotentials where great attention has been placed on maximising the pseudopotential performance without compromising the science [61].

The pseudopotentials used throughout this thesis use the Kleinman-Bylander form generated using the Q_c tuning method for optimisation. In the Q_c tuning scheme

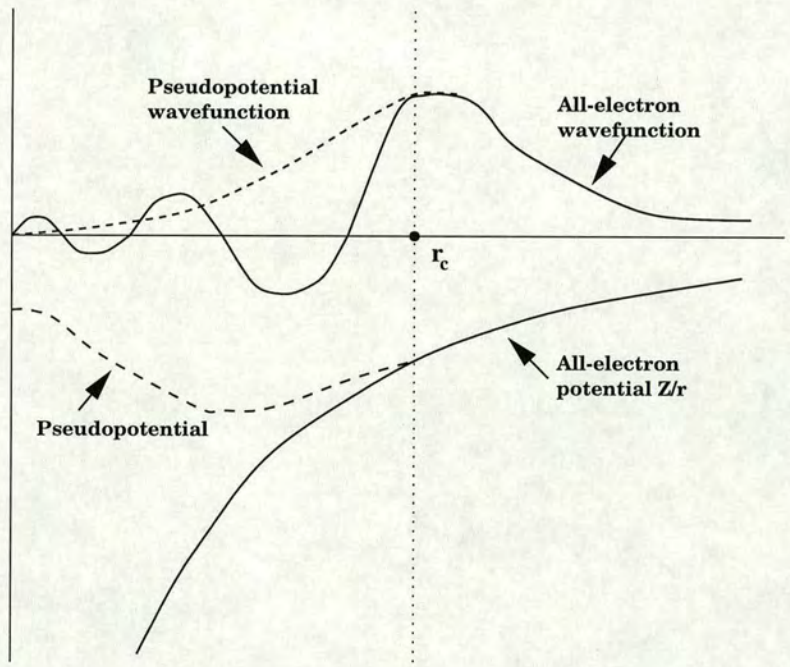

Figure 2.3. Schematic illustration of all-electron and pseudo-electron potentials and their corresponding wave functions. The radius at which all electron and pseudo-electron values match is called r_c. If pseudopotentials obey this constraint they are known as norm-conserving. The pseudopotential is constructed so that its scattering properties or phase shifts for pseudo wavefunctions are identical to the scattering properties of the ion and core electrons on the all-electron derived valence wavefunctions. The pseudopotential acts on a pseudo wavefunction rather than the real wavefunction.

[60, 61] a wave-vector Q_c acts as a kinetic energy filter controlling a constrained minimisation of the kinetic energy of the pseudo-wavefunction. The underlying idea is that a pseudo-wavefunction with lower curvature requires fewer plane waves for its expansion, hence by minimising the kinetic energy (and therefore the curvature) of the pseudo-wavefunction a pseudopotential is more computationally efficient.

2.5 The plane wave basis set and supercells

It has been demonstrated that the complex functionals in the many-electron problem can be mapped onto equivalent functionals in an effective single-particle problem. However, there still remains the task of constructing the wavefunction for the electrons moving in the static potential generated by the nuclei. This is done by expanding the electronic wavefunction in terms of a discrete plane-wave basis set. The advantages of a plane wave basis set are that its convergence properties toward completeness are easily tested, and force calculations are simplified (see Section 3.2.1).

In these calculations periodic boundary conditions are imposed. The molecule is placed in a supercell which is reproduced throughout space. The plane waves are expanded in accordance with Bloch's Theorem [63] which states that in a periodic system each electronic wave function can be expressed as the product of a wave-like component (with wave vector $\mathbf{k}$) and a supercell-periodic component $f_i(\mathbf{r})$:

$$\psi_i(\mathbf{r}) = \exp[i\mathbf{k}.\mathbf{r}]\ f_i(\mathbf{r}) = \sum_G c_{i,\mathbf{k}+\mathbf{G}}\ \exp[i(\mathbf{k}+\mathbf{G}).\mathbf{r}] \tag{2.19}$$

The supercell periodic function ($f_i(\mathbf{r})$), where i is the band index, is expanded using a basis set consisting of a discrete set of plane waves corresponding to the reciprocal lattice vectors $\mathbf{G}$ of the periodic structure. Basically the introduction of a periodic component to the wavefunction means the wave-like component of the function, the plane wave, need only be defined using a finite number of $\mathbf{k}$-points. An isolated molecular system presents the simplest case where only one k-point, the gamma point is required.

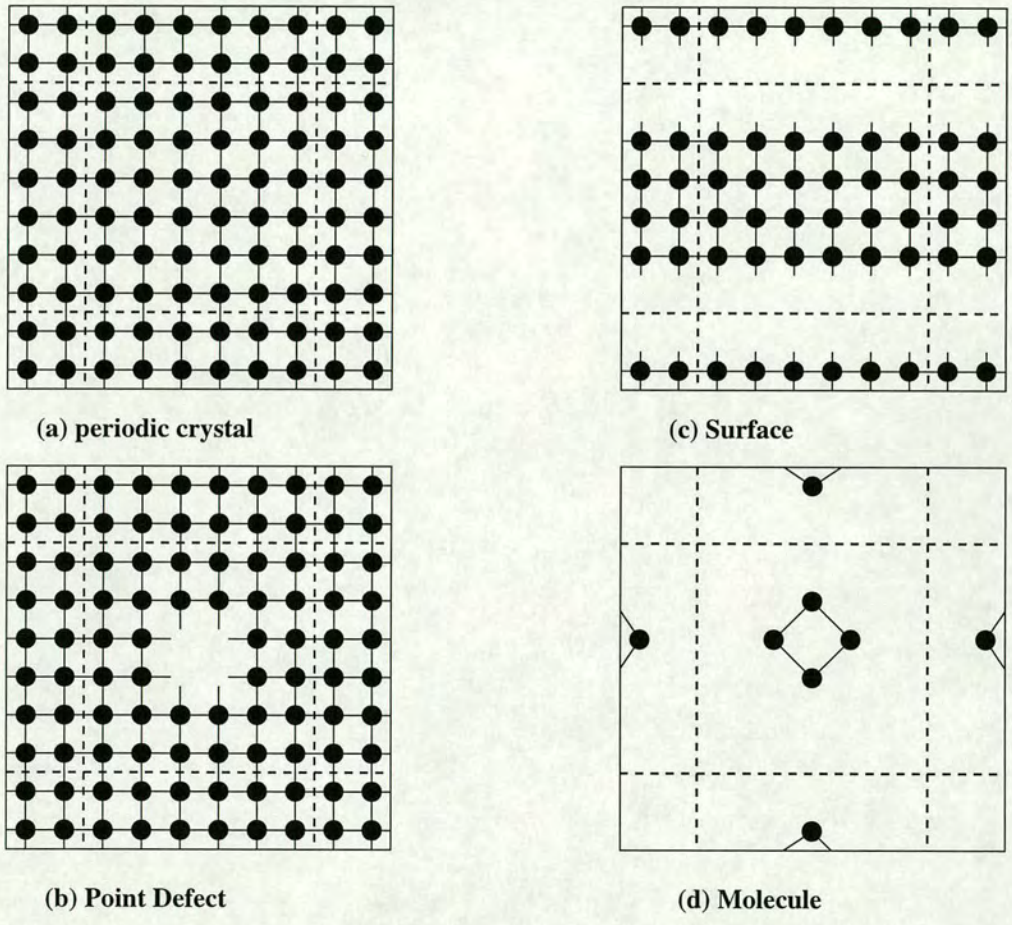

Figure 2.4. Schematic illustration of the supercell geometries for (a) the crystalline solid, (b) a point defect in a crystalline solid, (c) surface of a bulk solid and (d) an isolated molecule.

For crystalline systems with highly complex Brillouin zones many more k-points are required. For these systems it is important that the set of **k**-points used is sufficiently dense to calculate the electronic wavefunctions accurately. This is ensured by checking that the total energy is converged with respect to the density of **k**-points.

Figure 2.4 illustrates the supercell geometries for four cases; bulk solid, point defect, a surface and a molecule. As indicated in the Figure the molecule is placed in the centre of a periodically repeating supercell, the size of which must be taken to be sufficiently large that to ensure the molecules are effectively isolated from each other. This is further discussed in the next Section. An advantage of using the plane waves as described by Eqn. 2.19, is that the Kohn-Sham equations take on a simple form [41]. Substitution of Eqn. 2.19 into the Kohn-Sham equations, Eqn. 2.13, and integration over **r** gives:

$$\sum_{\mathbf{G}'} \left[\frac{\hbar^2}{2m} |\mathbf{k}+\mathbf{G}|^2 \delta_{\mathbf{G}\mathbf{G}'} + V_{eff}(\mathbf{G}\text{-}\mathbf{G}') \right] c_{i,\mathbf{k}+\mathbf{G}'} = \epsilon_i c_{i,\mathbf{k}+\mathbf{G}} \tag{2.20}$$

Solution of Eqn. 2.20 may be performed by matrix diagonalisation after which new potentials are recalculated and the process iterated until the ground state charge density which minimises the Kohn-Sham functional is found. However this procedure is computationally expensive as the cost of matrix diagonalisation increases as the third power of the number of plane waves. Therefore an alternative technique must be used for minimising the Kohn-Sham energy functional which leads to the same self-consistent Kohn-Sham eigenstates and eigenvalues as would conventional matrix diagonalisation.

In this work the variational principle is used to locate the ground state of the Kohn-Sham functional. The minimisation procedure is performed using the conjugate-gradients [64] technique. This conjugate-gradients technique directly minimises the energy as a function of the wavefunction coefficients in the knowledge that there is only one well defined minimum. Whereas the steepest descents method chooses the descent direction based on the gradient of the current step and makes a single step

in this direction, the conjugate gradients method starts along the steepest descents direction until a minimum in this direction is obtained and then proceeds along a direction perpendicular (or conjugate) to this current direction. The assumption is that once the current direction has been minimised any improvement will occur in orthogonal directions. This process is continued until the energy is minimised below a specified threshold. The rate of convergence of the conjugate-gradients method is improved further by using pre-conditioning which quickly converts the broad eigenvalue spectrum of the KS Hamiltonian to a nearly degenerate spectrum. The conjugate gradients technique provides a simple, direct and effective method for locating the minimum of the functional. Prior to the variational approach described above, the Car-Parrinello [65] molecular-dynamics scheme was used. In this scheme the coefficients of the plane wave basis set ($c_{i,\mathbf{k}+\mathbf{G}}$) are treated as coordinates of classical particles which are given a kinetic energy. The system of these particles is gradually cooled (simulated annealing procedure for minimisation) until the set of coordinates reaches the values which minimise the functional.

Determination of basis set size

Eqn. 2.19 represents the wavefunctions as a sum of plane waves with vectors $\mathbf{k} + \mathbf{G}$. If the supercell for an isolated molecule contains $2m$ electrons then there will be m doubly occupied bands and one $\mathbf{k}$ wave-vector, the gamma point. Ideally there should be an infinite number of plane waves contributing to each band wavefunction, but in practice the series is truncated according to some cutoff energy $\mathcal{E}_c$ to cut down the computational cost. The energy $\mathcal{E}_c$ truncates the basis set such that the coefficients $c_{i,\mathbf{k}+\mathbf{G}}$ in Eqn. 2.19 for the plane waves with kinetic energy ($\hbar^2|\mathbf{k}+\mathbf{G}|^2/2m$) above the cutoff energy are zero. The error introduced due to this truncation is small as the value of $\mathcal{E}_c$ is carefully chosen to ensure those plane waves not used would not have taken any significant part in bonding. Typically plane waves with high kinetic energy (which represent rapid fluctuations in the charge density) only occur in response to an

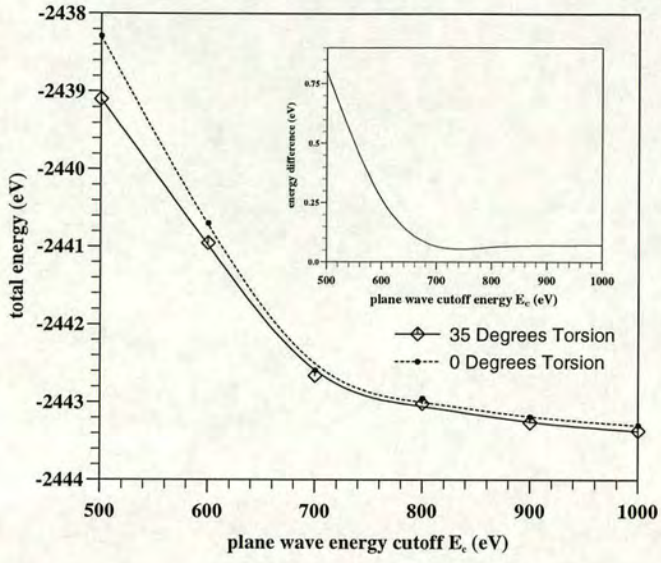

Figure 2.5. The total energy for two conformers of 4-cyanobiphenyl. The inset shows the difference between them. The convergence of the energy difference between the two structures indicates what plane wave cut-off energy $\mathcal{E}_c$ must be used for this system. The energy is in eV (1eV= 96.45 kJ/mol).

extreme external potential. For molecular systems these would only occur in region close to the ions which are occupied by the core electrons. The charge density in this region plays little part in any bonding between atoms.

Figure 2.5 shows how the total energy difference in between two different conformations of the same molecule varies with respect to $\mathcal{E}_c$. At 700eV, it can be seen that the energy difference (inset graph) converges. The energies are converged to within 0.01 eV for both conformations ($\sim$0.001eV per atom). This signifies that beyond 700eV the extra plane waves of higher kinetic energy do not take any part in bonding. If they did take part then the energy difference between the two conformers would change since they have different bonding structures. For all the calculations presented in this thesis the electronic wavefunctions were expanded to a 700eV cutoff, except for the molecules containing fluorine where 1000eV is used as it has a deeper pseudopotential.

2.6 Determination of supercell dimensions

An important consideration in performing a calculation to determine molecular properties, is that the size of the supercell is large enough so as to ensure that the molecule is isolated from its periodic images. It has been found that by ensuring that the properties under investigation are converged with the size of the supercell, the supercell method gives identical results to calculations for finite systems [66], even for molecules with large dipole moments. An insufficiently large supercell can significantly influence the property under investigation whether that be torsional potentials, structure or electrostatic moments. In particular, when the molecules under consideration have strong electric dipoles which can create a dipolar field, then careful attention must be given to the supercell dimensions so as to ensure isolation of the molecule. In this Section the influence of the supercell size on total energy, dipole moments and conformational energy differences for the two dipolar molecules 2-2′ difluorobiphenyl and 5CB is demonstrated. For all the calculations presented in this thesis the supercell was tested for convergence to ensure isolation. In general, it was found that a vacuum distance between neighbouring molecules of greater than 6Å was sufficient to isolate them.

2-2′ Difluorobiphenyl

The mesogenic fragment 2-2′ difluorobiphenyl consists of two phenyl groups with a fluorine atom replacing one of the hydrogens on each group. The addition of fluorine atoms on the lateral hydrogen sites creates highly dipolar regions situated on carbon fluorine bonds. The dipolar field arising from these regions must be made arbitrarily small by increasing and testing the size of the unit cell. Figure 2.6 shows how the weak dipole-dipole interaction can be made arbitrarily small, and is overcome by a strong repulsion due to wavefunction overlap at small separation. From the Figure it can be seen that a supercell dimension of $15 \times 10 \times 10 \mathring{A}$ is adequate to converge total energy and

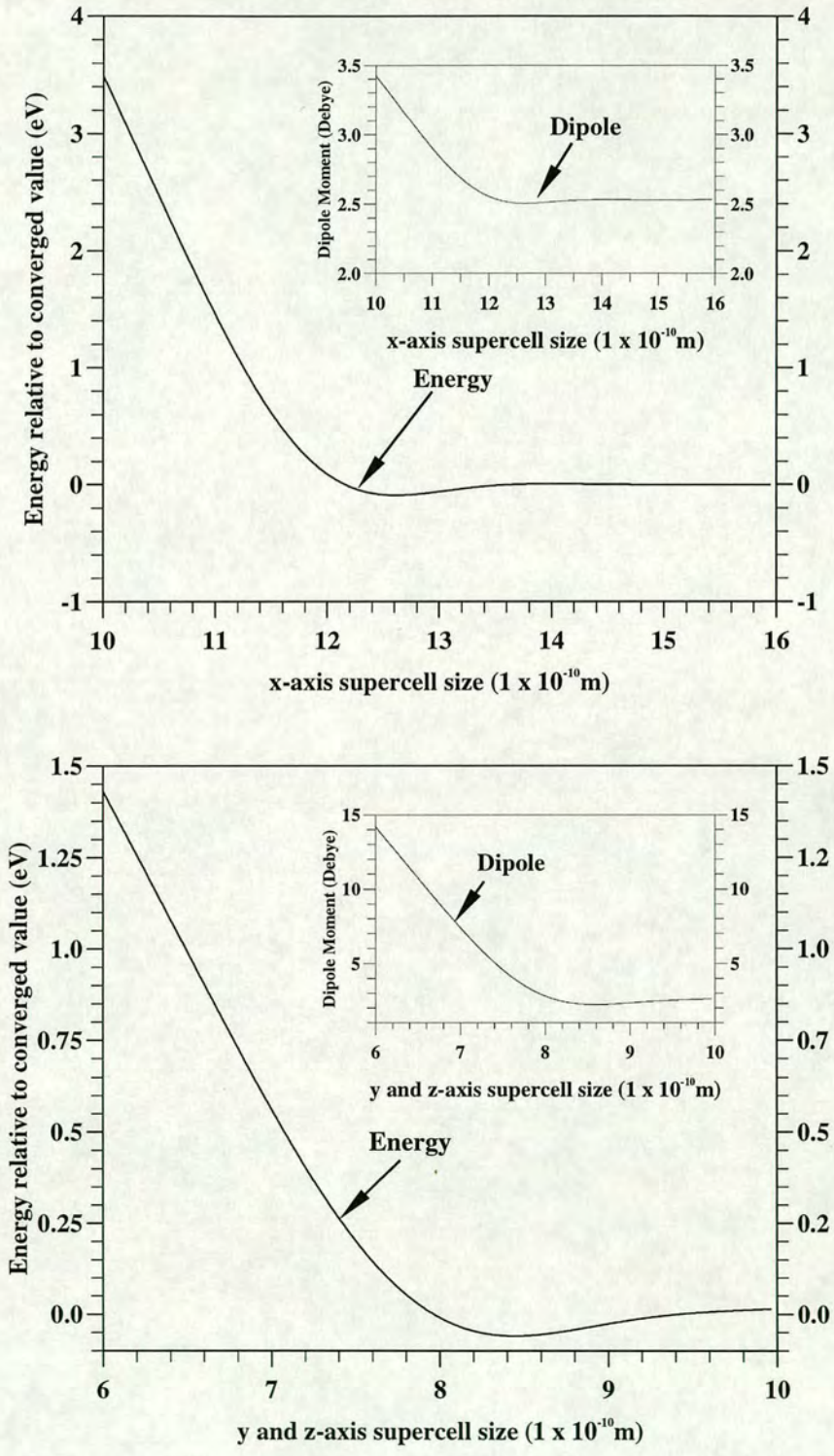

Figure 2.6. Convergence of the total energy and dipole moment with increasing supercell size for the molecule 2-2′ difluorobiphenyl. The long molecular axis lies along the x axis. The top Figure refers to the variation in total energy and dipole with respect to the x-axis supercell dimension for fixed values of the y and z dimensions. The bottom Figure plots the energy and dipole with respect to the y and z-axis supercell dimensions for a fixed value of x dimension. Energy is in eV where 1eV=96.45 kJ/mol.

Dimensions in Å			Energy difference in kJ/mol
x	y	z	(ttt - gtt)
16.0	10.0	10.0	7.39
17.0	10.0	10.0	3.66
19.0	10.0	10.0	3.07
20.5	10.0	10.0	2.31
21.0	10.0	10.0	2.29
20.5	10.5	10.5	2.31
20.5	11.0	11.0	2.32

Table 2.1. Table to illustrate the convergence of the energy difference between two conformers of 5CB with increasing supercell size. The two conformers were chosen on the basis that they had the most dissimilar shape and would therefore be most sensitive to the supercell dimensions. Geometries for both conformers were only partially relaxed at this stage of testing. More details for these calculations with fully relaxed geometries and their use in the calculation of ordering parameters can be found in Chapters 4 and 6.

render the dipolar field too weak to have any influence. Higher order electric multipole moments of the molecule will also be converged by this point as the electric field falls off as increasingly higher powers with distance.

Another issue for consideration is that one must also test for the convergence of the dipole moment. Figure 2.6 (inset) shows how the dipole converges with supercell size. The algorithm used to calculate the dipole is described in Section 5.1.1. It was found that for small supercell dimensions, some of the electron charge overlaps with the edges of the supercell. This charge however, enters the supercell on the opposite side due to the periodicity. Since the dipole algorithm only considers the charge within one cell, the displaced electron charge therefore gives an incorrect value for the dipole. This can be clearly seen in Figure 2.6, where the dipole significantly increases for smaller supercell dimensions. All the molecules investigated in this thesis were placed in the centre of the supercell. The dipoles were checked for convergence to ensure there was no electron charge overlap.

5CB

A significant amount of work presented in this thesis is performed on the mesogenic molecule 5CB. A investigation into this molecule required all the conformations of the tail to be investigated. As these variations in the tail conformations significantly changed the overall shape of the molecule, a larger than normal supercell was required so as each conformer was isolated irrespective of shape. Table 2.1 shows some of the results from the convergence tests aimed at determining the most efficient and accurate supercell size. The long axis of the molecule is along the x-direction. The Table shows how the energy difference between two conformers of 5CB; one which has an all *trans* (ttt) and one with a *gauche* in the first C-C tail bond (gtt), varies with supercell size. From the table is it can be seen that a box size of $20.5 \times 10.5 \times 10.5\mathring{A}$ was adequate to ensure convergence of energy difference between the two conformers.

2.7 Ion-ion interactions: Ewald sum

Now the only calculations left is the Coulomb interaction between the static ions and their periodic images. As the Coulomb interaction is extremely long ranged the calculation is not straightforward. The sum is instead spilt over real and reciprocal space using the Ewald method [67]. It replaces the non-convergent Coulombic sum:

$$E = \frac{1}{2}\sum_{I \neq J} \frac{Z_I Z_J e^2}{|\mathbf{R_I} - \mathbf{R_J}|} \tag{2.21}$$

with two convergent sums; one in real space, the other in reciprocal space with an additional small correction for self-interaction. Considering first the real space sum, each ion is surrounded by a charge distribution of equal magnitude but opposite sign which spreads out radially from the charge. This distribution normally takes the form of a Gaussian. This extra distribution has the effect of screening the interaction between neighbouring ions, making them short-ranged. The total screened potential is

then calculated for all the periodic images in real space. Following this, another charge distribution of the same sign as the original ion and same magnitude and form of the screening charge distribution is added. This has the effect of cancelling the original screening charge. This cancelling distribution is summed in reciprocal space. Unfortunately this reciprocal space sum includes the interaction of the cancelling distribution with itself, which must be corrected for and subtracted from the total. In the reciprocal space summation the Ewald sum ignores the $\mathbf{G} = 0$ contribution. This is because in the infinitely repeating system the ion-ion energy and the electron-electron energy $\mathbf{G} = 0$ contributions which are divergent, cancel each other out. Omitting the $\mathbf{G} = 0$ contributions also has the consequence that any constant potential across the supercell cannot be represented since it would require $\mathbf{G} = 0$ terms. This is consistent with periodic boundary conditions which do not allow non-periodic potentials.

2.8 Codes and computational details

All the *ab initio* calculations in this thesis have been performed with The Cambridge-Edinburgh Total Energy Package (CETEP code) [68, 69]. CETEP is a parallel version of CASTEP (CAmbridge Serial Total Energy Package) and has been implemented on the massively parallel Cray T3D at the Edinburgh Parallel Computing Centre. Both codes are widely used by members of the United-Kingdom Car-Parrinello consortium on a range of serial and parallel machines. Recently CASTEP has been implemented as part of a commercially available molecular modelling package called Cerius^2 [70]. Developments of the CETEP code as part of the work in this thesis involved writing one new routine to calculate the dipole and quadrupole moments, as described in Chapter 5. Additional alterations to CETEP routines were performed in order to have more control over the charge density read outs. Other code developments performed during the thesis which were not part of CETEP are indicated where relevant.

CETEP and CASTEP use a plane wave basis set to expand the electronic wavefunction on which band-by-band minimisation is achieved through preconditioned conjugate gradients. Orthogonality of the single particle states is obtained through the Gram-Schmidt orthogonalisation scheme [41]. The generalised gradient correction scheme is also used throughout the thesis and only one **k** point is used; the gamma point. In CETEP the plane waves and real space grid points are distributed over different processors [68]. The valence charge density is computed on a discrete fast-Fourier-transform (FFT) grid and it is obtained directly from the wavefunctions.

The size of the FFT grid depends on supercell size and cutoff energy. As the Γ point is used as the only sampling point we are only concerned with the real (as opposed to complex) wavefunctions which halves the computational cost of the calculation. As an example, for the calculation on 2-2′ difluorobiphenyl described in Section 4.2.1 the supercell dimensions were $15 \times 10 \times 10 \mathring{A}$ necessitating an FFT grid size of $160 \times 108 \times 108$. The charge density of the molecule is then therefore mapped by approximately 200,000 points. In terms of computational cost, an electronic structure calculation without any form of relaxation of the ions, requires between 0.5 (small molecules) to 50 (5CB) Cray-T3D CPU hours (where one CPU hour is defined as one hour of processing time on an Alpha 300 MHz workstation). The electronic degrees of freedom were relaxed until the total energy of the molecule was converged to within 10^{-7} eV/molecule, which was more than adequate for the properties under investigation.

Chapter 3

Molecular Structure And Vibrational Properties

3.1 Introduction

Since the total energy obtained from a pseudopotential calculation is not the actual all-electron energy, it is of little meaning by itself. However, when viewed in comparison with energies calculated for other structural configurations of the same molecule, many properties can be determined. For example, once the total energy as a function of the positions of the atoms is known, quantities such as equilibrium structure, bonding, conformational dynamics and vibrational characteristics can be calculated. In many respects, the use of pseudopotentials can actually be an advantage. Since the energy difference between two structural configurations is a greater fraction of the total energy, the pseudopotential calculation can achieve a greater accuracy.

Traditionally, the first principles methods used in this thesis have been used to predict many bulk physical properties of crystalline and amorphous solids [71, 72], defects [73], liquids [74, 75], solid-solid phase transitions [76], surface reconstruction [77, 78, 79] and chemisorption [80]. Only recently have they been applied to study molecular systems [10, 81, 82, 83, 84]. The work in this thesis represents some of these

first applications.

In this Chapter a series of calculations to determine equilibrium structures and vibrational properties are performed on several mesogenic fragments and 5CB. The chapter is organised as follows. The method of structural optimisation is first described and then performed on several molecular systems including small test molecules and mesogenic fragments such as butane, biphenyl and 2-2′ difluorobiphenyl. The results are then compared with available experimental and *ab initio* data. The equilibrium conformation and structure of 5CB is determined and compared with NMR data. Special attention is paid in all cases to how the geometry changes with conformation, as this information is used in the following Chapters to calculate and interpret torsional potentials and electrostatic moments. Following this the vibrational properties of benzene and 5CB are calculated and found to be in excellent agreement with experimentally observed values.

3.2 Determination of equilibrium molecular structure

As the equilibrium structure for molecular systems lies on a relatively flat multidimensional energy surface, it is necessary that an efficient method to locate the minimum energy structure be used. The method used in this work relies on the fact that the atoms are in their equilibrium positions when there are no net forces on them. If a force is found to exist on an atom, that particular atom is moved in order to minimise that force.

3.2.1 Forces

The force acting on an ion at position $\mathbf{R_I}$ in general is given as:

$$F_I = -\frac{dE}{d\mathbf{R}_I}. \tag{3.1}$$

However, as the force is dependent on the energy E and consequently the wavefunction Ψ, care must be taken in calculating the force. This is because the minimum of the Kohn-Sham Hamiltonian is meaningful only within Born-Oppenheimer (BO) approximation. In other words, any change in the ionic positions must be accounted for by calculating a new wavefunction. This allows the electronic wavefunction to lie on the BO surface in the multidimensional space of (E, Ψ, $\mathbf{R}_I$). The forces acting on an ion at position $\mathbf{R}_I$ can be written as an expansion of (3.1):

$$F_I = \sum_i -\frac{\partial E}{\partial \mathbf{R_I}} - \frac{\partial E}{\partial \psi_i}\frac{\partial \psi_i}{\partial \mathbf{R_I}} - \frac{\partial E}{\partial \psi_i^*}\frac{\partial \psi_i^*}{\partial \mathbf{R_I}}. \tag{3.2}$$

The Hellmann-Feynman [85] theorem argues that since the wave function is an eigenstate of the Hamiltonian ($\frac{\partial E}{\partial \psi_i^*} = H\psi_i$), then the second and third terms in (3.2) which involve the wavefunctions become:

$$-\left(\frac{\partial E}{\partial \psi_i}\frac{\partial \psi_i}{\partial \mathbf{R_I}} + \frac{\partial E}{\partial \psi_i^*}\frac{\partial \psi_i^*}{\partial \mathbf{R_I}}\right) = -E\frac{\partial}{\partial \mathbf{R_I}} < \psi_i\psi_i^* > . \tag{3.3}$$

Since $< \psi^*\psi >$ is a constant by normalisation, then its derivative must be zero. The last two terms in Eqn. 3.2 are therefore also zero, which simplifies the calculation of the force (known as the Hellmann-Feynman forces) to taking just the derivative of the total energy with respect to ion position:

$$F_I = -\frac{\partial E}{\partial \mathbf{R_I}} \tag{3.4}$$

However, fundamental to this simplification is the fact that the electronic wavefunction must be an *exact* eigenstate of the KS Hamiltonian, which is impossible in computations to achieve without the use of an infinite basis set. If the wavefunctions are represented by a basis set such as $\psi_i = \sum_j c_{ij}\phi_j$, then the expansion of (3.1) must

include the effect on the basis set of moving the ions. This requires a further expansion of ψ_i into terms involving the basis set:

$$\frac{\partial E}{\partial \psi_i}\frac{\partial \psi_i}{\partial \mathbf{R_I}} = \sum_{ij}\frac{\partial E}{\partial c_{ij}}\frac{dc_{ij}}{d\mathbf{R_I}} + \sum_{j}\frac{\partial E}{\partial \phi_j}\frac{d\phi_j}{d\mathbf{R_I}}. \tag{3.5}$$

The first term on the right hand side is zero if the wavefunctions have completely converged within a calculation. That is, the Hellmann-Feynman theorem holds if $\frac{\partial E}{\partial c_{ij}} = 0$. The second term deals with the contribution to the force from the variation of the basis set with the ionic position, known as the Pulay force [86]. If the basis set is not sufficiently complete to accurately describe the eigenfunctions, the Hellmann-Feynman theorem does not hold. However, for the plane wave basis set which is totally independent of the ion positions, $d\phi_j/d\mathbf{R_I} = 0$. Thus the advantage of using a plane wave basis set is that the Pulay force is zero and any error in the Hellmann-Feynman force is directly related to the extent which the wavefunction is converged, and may therefore be reduced to an arbitrarily small value.

Plane wave basis sets are more accurate and efficient in comparison with other basis sets for the calculation of properties which require the forces to be examined, such as the optimisation of ions and vibrational properties. When localised basis sets are used, the optimisation of molecular geometry under the influence of quantum mechanical forces can be complicated by the need to evaluate correction terms (large Pulay forces) which are due to the basis set itself. A further difficulty arises in the determination of vibrational frequencies. In conventional methods, the calculated mode frequencies are slowly convergent with respect to basis set size and therefore require extremely large numbers of basis functions.

3.2.2 The relaxation of the ions

Relaxing a set of ionic positions is an iterative process which involves moving the ions in the direction of the calculated force, re-calculating the new electron wavefunction from the old one, then re-calculating the new force, and so on. This procedure is performed using the same conjugate gradients scheme as discussed in Section 2.5. The calculation of the Hellmann-Feynman forces requires the wavefunction to be calculated to a high tolerance. Errors in the calculated forces used to optimise ionic positions can cause the ionic configuration to drift away from the local minimum.

To ensure that the efficient relaxation takes place, it is useful to begin with reasonable starting positions. The maximum movement of the atoms is generally constrained to $0.1\mathring{A}$ per iteration so that the new wavefunction can be updated efficiently from the old one. Unless otherwise stated, geometries for the large molecules were taken from a molecular modelling package Cerius^2, [70] without any form of optimisation. For smaller molecules the initial geometries are constructed by hand using standard bond lengths and angles.

The optimisation of the geometry is performed under set constraints so as to guarantee the level of convergence of the optimised structure. The Hellmann-Feynman force on each atom in the molecule is calculated and the atoms are moved under the influence of these forces until no force component exceeds some tolerance. Unless stated otherwise, structure optimisation is converged when residual forces on the atoms are below 0.1 eV/Å(a higher tolerance of 0.01eV/Å is required for vibrational frequencies). It is found that further relaxation beyond this level changed structures by less than 0.15%. For all the calculations performed, molecular point group symmetry is not enforced so as to reveal any small symmetry breaking that may occur. Also in the calculations, finite temperature effects are not included.

Molecule	Parameter	Expt[a]	MP2[a]	DFT/6-31G*[b]	This work
H_2O	r(OH)	0.958	0.969	0.976	0.963
	∠(OH)	104.5	104.0	103.6	105.1
N_2	r(NN)	1.098	1.131	1.118	1.080
HCN	r(NC)	1.169	1.187	1.171	1.131
	r(HC)	0.994	1.002	1.080	1.066
O_2	r(OO)	1.208	1.242	1.234	1.225
HF	r(HF)	0.917		0.940	0.929
AAE			1.72%	2.81%	1.21%

[a] All experimental and MP2 values are taken from Ref. [45]. MP2 values optimised using *Gaussian 90* and a 6-31G^* basis set.
[b] All values taken from Ref. [87]. Optimised using HF-DFT employing a 6-31G^* basis set and the Becke exchange-correlation functional [49].

Table 3.1. Theoretical and experimental geometries for small molecules. Bond distances (r) in Å, bond angles in degrees. The average absolute error (AAE) is also shown.

3.3 Equilibrium molecular structures

3.3.1 Small test molecules

Optimised molecular structures were calculated for several small molecules; H_2O, N_2, HCN, O_2 and HF for which simple comparisons could be made both with other *ab initio* work and experimentally observed values. Initial starting geometries for H_2O were such that the hydrogen atoms were placed at right angles to one another at a distance of $1\mathring{A}$ from the oxygen. For the other molecules all the atoms were initially placed $1\mathring{A}$ apart. The supercell dimension for all these systems was $10.0 \times 10.0 \times 10.0\mathring{A}$ for which the energy had sufficiently converged. The optimised structures are shown in Table 3.1 along with those from localised basis set DFT calculations [87], MP2 level calculations and experiment. The level of accuracy achieved by this work is excellent in comparison with both other *ab initio* methods.

Benzene has been studied in considerable detail by a variety of quantum chemical

Method/Basis set	r(CC)(Å)	r(CH)(Å)	Ref.
This work	1.396	1.089	
CCSD/cc-VTZ[a]	1.393	1.082	[88]
MP2/6-31G**	1.398	1.086	[89]
MP2/TZ2P[b]	1.390	1.079	[90]
MP2/TZ2P	1.390	1.080	[91]
Expt.	1.393-1.398	1.081-1.090	[92]

[a] Contracted, correlation-consistent valence triple zeta set.
[b] Triple zeta plus two polarisation functions.

Table 3.2. Calculated and experimental geometries for Benzene.

methods and it is therefore an excellent test case. It exhibits regular hexagonal planar symmetry with six carbon atoms joined by σ bonds and six remaining p-orbitals which overlap to form a delocalised π bond over all six carbon atoms. The initial configuration of benzene had the C-C and C-H bonds, 1.33 Å and 1.00 Å, respectively. The resultant relaxed structure after optimisation is summarised in Table 3.2, along with results obtained from other methods [88, 89, 90, 91]. To within the numerical accuracy used, all C-C bonds and C-H were of equal length although no external constraint is applied to enforce this symmetry. As the Table indicates the optimised C-C and C-H bondlengths are 1.396Å and 1.089Å, respectively, which compare well with experimental bondlengths of 1.393 - 1.398 Å and 1.081-1.090 Å respectively [92].

3.3.2 Mesogenic fragments with internal rotations

Butane

Butane is the smallest hydrocarbon molecule that forms isomers. It serves as a prototype system for aliphatic chain molecules and so represents an important molecular group found in many mesogenic molecules. Most research interest is concerned with the torsional potential for rotation about the central C-C bond, and in particular the conformational energies which correspond to the potential's four unique stationary points, illustrations of which are given in Figures 3.1(a-d). A full description of this potential

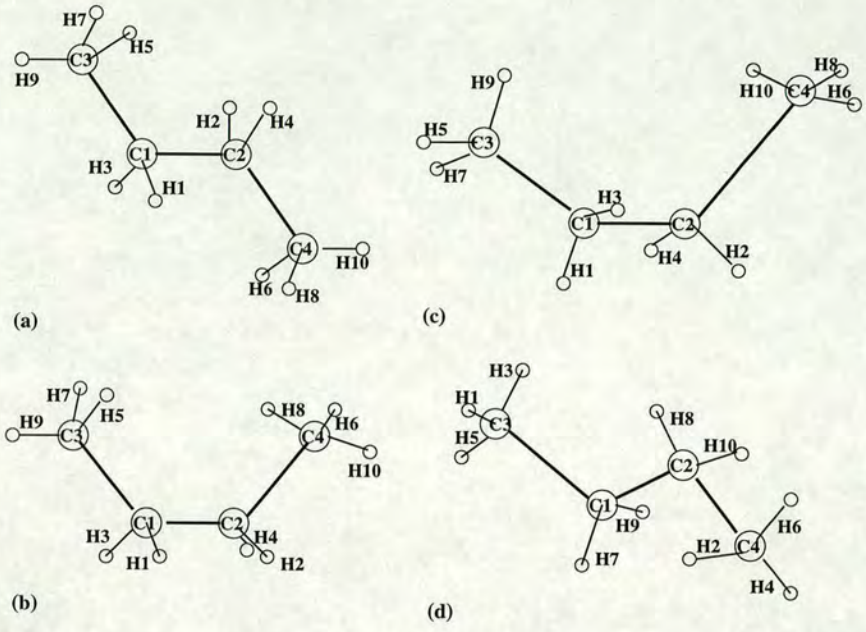

Figure 3.1. The (a) *trans*, (b) G/G-barrier, (c) G/T-barrier and (d) gauche stationary conformers of butane. Atoms are labelled according to Table 3.3.

can be found in Section 4.2.1. Table 3.3 shows a full set of optimised geometrical parameters for each of the four conformers, as well as parameters from the most recent *ab initio* work. It can be seen from the Table that the CISD (configuration interaction with single and double substitutions) results [93] are in reasonable agreement with this work. The bond distances for both sets of results agree to within 0.025 Å and bond angles within 1°. The available experimental data for bond distances: r(CC) 1.533$\AA$, r(CH) 1.108$\AA$, $\theta(CCC)$112.4°, $\theta(CCH)$110.5° (averages between the *trans* and gauche isomers) [94], is in good agreement with both methods. Both sets of parameters also agree that while the C_1-C_3 bondlength varies only slightly between conformers, the central C_1-C_2 bond distance changes significantly. This result is rather surprising since this bond is relatively remote from the centre of interaction.

There are a few disagreements, however, on the relative changes in the structural properties between the different stationary points. Namely the CISD parameters predict an increase in the C_1-C_2 bond distance in going from the G/T barrier to the *gauche*

Bond length (r)	Ref. [93]	This work	Bond angle (θ)	Ref. [93]	This work
trans (anti)					
$r(C_1 - C_2)$	1.527	1.513	$\theta(C_1C_2C_4)$	112.8	113.5
$r(C_1 - C_3)$	1.526	1.510	$\theta(C_1C_2H_2)$	109.1	109.6
$r(C_1 - H_1)$	1.094	1.099	$\theta(C_1C_3H_5)$	110.9	111.2
$r(C_3 - H_5)$	1.092	1.095	$\theta(C_1C_3H_9)$	111.4	111.9
$r(C_3 - H_9)$	1.091	1.094	$\theta(H_1C_1H_3)$	106.3	105.8
			$\theta(H_5C_3H_7)$	107.6	107.3
			$\phi(CCCC)$	0.0	0.0
G/T-barrier (*gauche*)					
$r(C_1 - C_2)$	1.530	1.530	$\theta(C_1C_2C_4)$	114.0	113.5
$r(C_1 - C_3)$	1.528	1.512	$\theta(C_1C_2H_2)$	108.7	110.0
$r(C_1 - H_1)$	1.093	1.095	$\theta(C_1C_2H_4)$	109.1	109.2
$r(C_1 - H_3)$	1.094	1.097	$\theta(C_1C_3H_5)$	110.9	111.0
$r(C_3 - H_5)$	1.091	1.094	$\theta(C_1C_3H_7)$	110.8	111.0
$r(C_3 - H_7)$	1.092	1.094	$\theta(C_5C_3H_9)$	111.7	112.1
$r(C_3 - H_9)$	1.090	1.095	$\theta(H_2C_2C_4)$	108.8	109.3
			$\theta(H_4C_2C_4)$	109.4	109.2
			$\theta(H_5C_3H_7)$	107.8	107.8
			$\theta(H_5C_3H_9)$	107.5	107.7
			$\theta(H_7C_3H_9)$	107.7	107.7
			$\phi(CCCC)$	119.5	112.5
gauche (120 st)					
$r(C_1 - C_2)$	1.543	1.517	$\theta(C_1C_2C_4)$	114.1	113.6
$r(C_1 - C_3)$	1.528	1.513	$\theta(C_2C_1H_7)$	109.4	108.8
$r(C_3 - H_1)$	1.092	1.094	$\theta(C_2C_1H_9)$	110.0	109.5
$r(C_3 - H_3)$	1.092	1.095	$\theta(C_1C_3H_1)$	110.8	111.9
$r(C_3 - H_5)$	1.091	1.094	$\theta(C_1C_3H_3)$	110.9	110.8
$r(C_1 - H_7)$	1.093	1.097	$\theta(C_1C_3H_5)$	111.5	111.9
$r(C_1 - H_9)$	1.092	1.097	$\theta(H_7C_1C_3)$	108.9	109.5
			$\theta(H_9C_1C_3)$	109.0	109.3
			$\theta(H_1C_3H_3)$	107.6	107.3
			$\theta(H_1C_3H_5)$	107.8	106.9
			$\theta(H_3C_3H_5)$	107.8	107.7
			$\phi(CCCC)$	180.0	180.0
G/G-barrier (syn)					
$r(C_1 - C_2)$	1.551	1.548	$\theta(C_1C_2C_4)$	116.6	115.7
$r(C_1 - C_3)$	1.530	1.515	$\theta(C_1C_2H_2)$	108.9	108.5
$r(C_1 - H_1)$	1.092	1.096	$\theta(C_1C_3H_5)$	111.8	111.0
$r(C_3 - H_5)$	1.091	1.091	$\theta(C_1C_3H_9)$	109.9	110.9
$r(C_3 - H_9)$	1.091	1.091	$\theta(H_1C_1H_3)$	105.6	105.1
			$\theta(H_5C_3H_7)$	107.7	107.6
			$\phi(CCCC)$	64.8	62.2

Table 3.3. Comparison of the optimised geometries of 4 conformers of butane: *trans*, *gauche*, G/T-barrier and G/G-barrier, with results from CISD calculations where double plus polarisation (DZP) basis sets (claimed to be very close to complete) were used. Inside the brackets are shown commonly used alternative labels for the conformers.

minimum. This work and other less recent *ab initio* studies of butane [95, 96, 97] predict a reduction in this bond length. Comparison with CISD results also reveals a small yet significant difference in the calculated dihedral angle of the carbon backbone ($\phi(CCCC)$) for the *gauche* conformer. Other high level quantum mechanical calculations [95, 96, 97] predict values from $113.0° - 114.8°$. The available experimental data for the $\phi(CCCC)$ angle of the *gauche* isomer: $108 \pm 5°$ [98], $118 \pm 1°$ [99], is in good agreement with both sets of results. The reason for the slight difference is thought partly to be a consequence of the flatness of torsional potential.

Biphenyl

The molecular structure of biphenyl is mainly characterised by the twist angle around the inter-ring C-C bond. Biphenyl is an important bridging group found in many mesogenic molecules and is thought to be responsible for a significant amount of rigidity and polarisability. Considerable experimental and theoretical efforts have been devoted to the study of the geometry and torsional potential. An important requirement for the accurate theoretical determination of the barrier heights and torsional potential is the optimisation of molecular structure. As there is still a disagreement between the experimental and *ab initio* calculations of the torsional potential (they differ in their predictions of energy barriers) the molecular structure has therefore attracted great interest. The π-conjugation between the phenyl rings stabilises the planar conformer whereas the steric repulsion between the ortho hydrogens favours the non-planar conformer.

The equilibrium torsional angle depends strongly on the state of aggregation. The angle has been found to very small in the condensed phases [100] where x-ray crystallography showed biphenyl to be planar in the crystalline state at room temperature. Recent electron diffraction studies [101] suggest that in the gas phase the equilibrium torsional angle (ϕ_{min}) is $44.4 \pm 1.2°$. Various levels of molecular orbital calculations have been used to estimate the twist angle. The more recent of these calculations

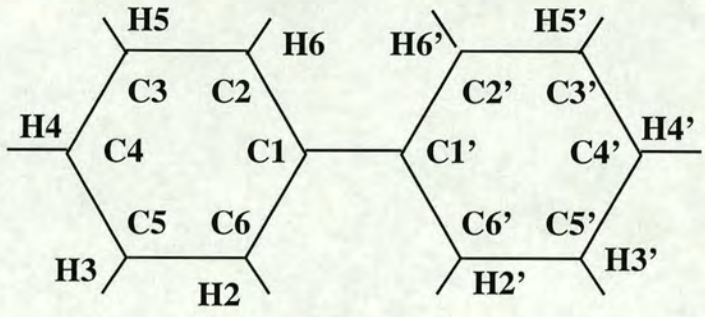

Figure 3.2. The numbering of the atoms in biphenyl as used in Table 3.4

Bond Distances and angles	Coplanar			Twisted			Perpendicular	
	This work	Ref. [102][a]	Expt[b]	This work	Ref. [102][a]	Expt[c]	This work	Ref. [102][a]
$C_1 - C_1'$	1.495	1.501	1.497	1.466	1.491	1.509	1.472	1.498
$C_1 - C_2$	1.391	1.396	1.398	1.386	1.392	1.406	1.383	1.390
$C_2 - C_3$	1.378	1.383	1.387	1.375	1.384	1.397	1.376	1.385
$C_3 - C_4$	1.373	1.383	1.379	1.377	1.385	1.398	1.375	1.385
$C_2 - H_2$	1.083	1.072	0.980	1.085	1.075	1.102	1.085	1.075
$C_3 - H_3$	1.086	1.075	0.990	1.085	1.075	1.102	1.086	1.076
$C_4 - H_4$	1.087	1.075	1.000	1.084	1.075	1.102	1.085	1.076
$H_2 ... H_2$	1.997	1.966	2.056	2.449	2.498		3.517	3.529
$C_2 - C_1 - C_6$	115.4	116.8	117.4	118.1	118.3	119.4	118.2	118.7
$C_1 - C_2 - C_3$	122.5	121.6	121.2	121.0	120.8	119.9	120.9	120.6
$C_2 - C_3 - C_4$	120.4	120.5	120.4	120.2	120.2	120.9	120.2	120.1
$C_3 - C_4 - C_5$	118.8	118.7	119.5	119.5	119.4	119.0	119.5	119.5
$C_1 - C_2 - H_2$	120.6	120.6	118.7	119.3	119.5	119.8	119.4	119.4
$C_2 - C_3 - H_3$	119.9	119.3	119.5	119.7	119.6	119.8	119.9	119.7
$C_3 - C_4 - H_4$	120.6	120.6	120.3	120.2	120.2	120.5	120.2	120.2

[a] (HF/6-31G**)

[b] From x-ray diffraction in the crystalline phase[100]

[c] From electron diffraction in the gas phase[101]

Table 3.4. Theoretical and experimental geometries for the coplanar, twisted and perpendicular conformers of biphenyl. All three sets of results are within 0.025Å and 0.1° of each other. When comparing the experimental and theoretical data for the coplanar structure it should be noted that the X-ray diffraction results used for reference, found that there were large oscillations about the coplanar structure around the interring C-C bond. There are no experimental parameters available for the perpendicular conformer.

estimate the angle to be 44.34° (HF/6-31G** [102]) and 46.26°(complete active space SCF where full CI is performed only on a subset of orbitals which is known as the *active space*) [103]. This work estimates the twist angle to be 43.0°, which is in good agreement with the most recent experimental observation.

The bond distances and angles of the twisted, coplanar and perpendicular conformers are shown in Table 3.4 along with results taken from HF/6-31G** level calculations and experiment. Figure 3.2 shows the atom numbering. Comparison of the geometries of the three conformers illustrates the significant variation upon internal rotation. The most significant changes occur in the inter-ring parameters which are involved in determining the distance between the hydrogen atoms in the ortho positions. The coplanar structure has the largest value of the C-C distance between the two phenyl rings and the smallest C_2-C_1-C_6 angle. It also has the smallest C_2-H_2 distance and largest C_1-C_2-H_2 angle. These features favour a large separation between the hydrogen atoms in the ortho positions. Subsequent rotation about the inter-ring C-C bond decreases the steric repulsion between the H_2 and H_2' atoms, allowing the central bond to become shorter, which is favoured by conjugation. This conjugation effect also explains why the C_1-C_1' distance for the perpendicular conformer increases, where there is less π conjugation. An enlargement of the C_1-C_2-C_6 angle occurs in going from the coplanar to perpendicular conformer is also noted.

3.3.3 Mesogenic fragment with dipolar regions

2-2′ difluorobiphenyl

There has been recent interest in understanding the effect that lateral fluorine substitutions on the central core has on liquid crystalline characteristics [104, 105]. The use of polar lateral substituents allows for the manipulation of the dielectric properties of the material. This has been investigated for the case of fluorinated terphenyls where the relative positions of the fluorine atoms significantly alters the electro-optical properties

and phase behaviour [106]. Although these substitutions lead to a smaller length to breadth ratio which tends to reduce the stability of a mesophase, they can also alternatively lead to inter-molecular interactions which enhance the phase stability. The molecular flexibility will have an important role to play in these interactions.

In this Section the molecule 2-2′ difluorobiphenyl is investigated. The addition of fluorine atoms on the lateral hydrogen sites of biphenyl to create 2-2′difluorobiphenyl, results in highly dipolar regions situated on the carbon fluorine bonds. Consequently the strong electrostatic interactions arising from accumulation of charge on the fluorine atoms and their increased steric repulsion, can significantly affect the molecular structure. The calculations on this molecule were performed using geometry optimisation at 20° and 10° intervals from 0° to 180°. Examination of the torsional potential for rotation about the C_1-C_1' bond (described in the later Section 4.2.1), shows the molecular structure to be described by two minima. As Table 3.5 shows, those minima occur at 57° (*cis* minimum) and 130° (*trans* minimum). This work finds the *cis* minimum to be the global minimum. This is in reasonable agreement with recent NMR spectroscopy investigations which have also investigated the molecular structure and torsional potential [107, 108]. They found that global minimum to occur at 51° and the local minimum at 130°. X-ray investigations of 2,2′-difluorobiphenyl have also been performed on the solid crystalline [108] and vapour phases [109]. In both cases (it was only possible to model the data in terms of a single conformation due to a small experimental data set) the molecule was found to be in the *cis* minimum with torsional angles of 58.4° (in the solid phase) and 60.0° (in the gas phase) respectively.

Although all the sets of results shown in Table 3.5 differ on the exact locations of the two minima, they agree on the preference for *cis* minimum as the global minimum. This preference for the *cis* minima is counterintuitive, since in this conformation the two highly dipolar C-F regions approach more closely than the 130° conformation. A similar "cis effect" has recently been observed in *ab initio* investigations of the molecule 1,2-difluoroethane [110]. The reason underlying this stabilisation is not well understood.

Method	*cis* minimum	*trans* minimum	C_1-C_1'-C_2'	C_1-C_2-F	C_1-C_1'	C_2-F
This work	57.0	130.0	122.1	119.8	1.475	1.339
(HF/6-31G*)[a]	56.98	128.7	121.7	119.0	1.489	1.328
NMR[b]	51.0	130.0	-	-	-	-
X-ray[c]	60.0	na	121.4	118.5	1.485	1.385

[a] Ref. [111]
[b] Ref. [107]
[c] Ref. [108]

Table 3.5. A selection of geometrical parameters (in Å and degrees) obtained in this work, recent *ab initio* work and experimental methods. Atom labelling is shown in Figure 3.3(a). All geometrical parameters are taken from global minimum conformer

Dihedral	C_1-C_1'	C_2-F	C_1-C_1'-C_2'	C_1-C_2-F
0.0 (*cis*)	1.489	1.335	128.0	122.2
20.0	1.478	1.335	126.7	121.9
40.0	1.474	1.336	124.5	120.2
60.0	1.473	1.337	121.9	119.1
80.0	1.474	1.339	122.0	118.8
100.0	1.474	1.340	122.0	118.8
120.0	1.473	1.340	122.0	119.0
140.0	1.474	1.342	122.1	119.4
160.0	1.477	1.343	122.3	120.8
180.0 (*trans*)	1.481	1.345	122.6	121.9

Table 3.6. Optimised geometrical parameters for different conformers. Each optimised geometry required approximately 400 T3D CPU hours. The 0^0 and 180^0 rotations correspond to the *cis* and *trans* conformations respectively. The atom labels are shown in Figure 3.3 (a).

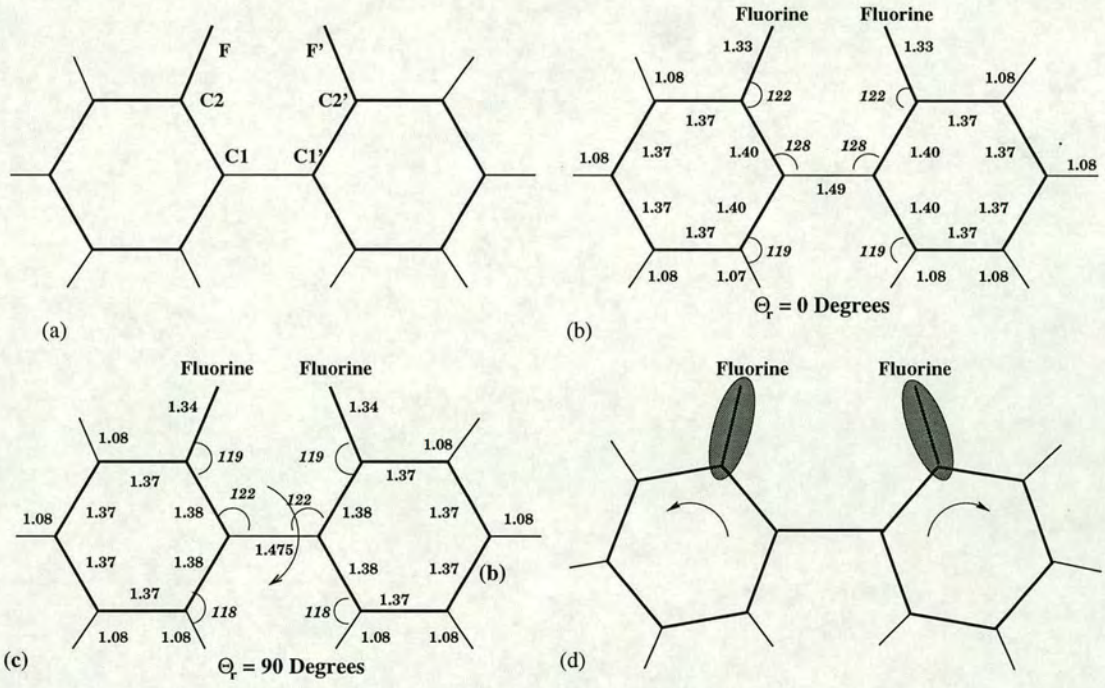

Figure 3.3. Figure (a) is a schematic illustration of 2-2′ difluorobiphenyl in the *cis* conformation with atom labels. Figures (b) and (c) show the optimised 0^0 and 90^0 conformations for comparison. The distances are in Å and both figures are projected onto a planar conformation for clarity. Figure (d) shows a schematic diagram indicating the nature of bond deformation that occurs in the 0° conformation. The highlighted areas indicate the dipolar regions.

The geometry of 2,2′-difluorobiphenyl changes markedly with rotation about the C_1-C_1' bond. Table 3.6 shows the values for certain key bond lengths and angles for 20° intervals between 0^0 and 180^0. As can be seen from the Table, although the bond angles C_1'-C_1-C_2 and C_1-C_2-F are insensitive to the torsional angle between the *cis* and *trans* minima, they do increase as the torsion angle approaches the planar conformation due to an increase in the steric repulsion between the fluorine atoms as they move adjacent to each other. The C_1-C_1' bond length also shows a dependence on the torsional angle, reflecting the contributions from the π electron conjugation and the H—H′, H—F′, and F—F′ steric effects.

In going from 180° to 0°, a reduction in the bond distance is initially observed due to increased conjugation. However, as the torsional angles approaches 0°, the steric interaction between the two fluorine atoms becomes more significant and the C_1'-C_1 bond lengthens. The C-F bond length is found to increase gradually from the 0° conformer to a maximum for the 180° conformer, with an inflection located at the torsional angle of the global minimum.

Figure 3.3(b) and (c) gives a comparison of two optimised structures in the 0^0 and 90^0 conformations. In the region 0^0 to 50^0 where significant repulsion between the two fluorine atoms occurs, the central bond bends such as to push the fluorines further apart. This effect is shown schematically in Figure 3.3(d). Also shown in this Figure are the two dipolar regions of the molecule which are located on the C-F bonds. These two areas of charge are the dipole components which are responsible for the overall molecular dipole described in Section 5.1.2.

3.3.4 The mesogenic molecule 5CB

NMR investigations [112] have determined that the minimum energy conformation of the nematogen 5CB, has an inter-ring torsional angle of 37.0° and ring-tail torsional angle of 90.0°, where the tail is all *trans* and perpendicular to the plane of the adjoining phenyl ring. This minimum energy conformation is also predicted by this work [81, 113]

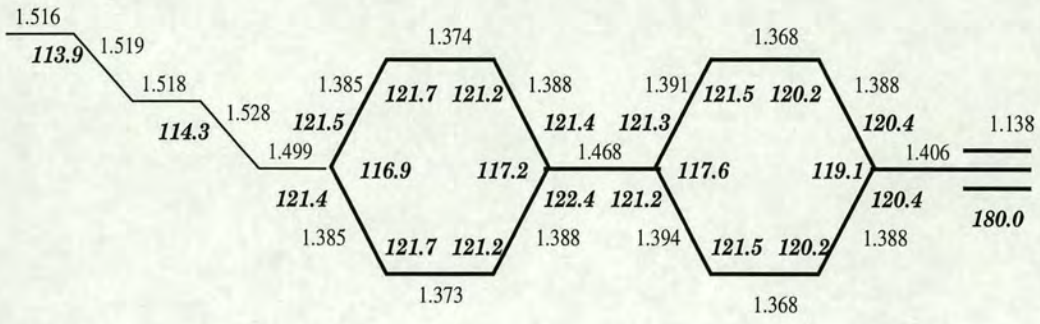

Figure 3.4. Schematic illustration of the important bond lengths and angles for the equilibrium structure of 5CB with an all *trans* tail perpendicular to the second phenyl group and a inter-ring torsional angle of 37°. The structure is projected onto a planar conformation for clarity.

although the equilibrium twist angle is predicted to be 36.0°. It should be noted, however, that the NMR investigation was performed using 5CB dissolved in a nematic liquid crystal solvent. The agreement between this work and NMR therefore suggests that 5CB does not change its equilibrium structure substantially on going from the gas to liquid phase. A full investigation into the conformational properties of 5CB, in the gas and nematic phases, can be found in Sections 4.4 and 6.4 respectively.

The calculated equilibrium bond lengths and angles for 5CB in its minimum energy conformation are shown in Figure 3.4. In the Figure the structure is projected onto a planar conformation for clarity. Investigations of the tail dynamics, as reported in the later Section 4.4.1, found the structure of the tail not to change by more than a few percent for all 27 conformations. This was not the case however for rotation around the inter-ring carbon bond, where significant changes in the structure occur. These changes, however, follow exactly the same trends as the biphenyl molecule already discussed in Section 3.3.2.

3.4 Molecular vibrations

3.4.1 Determination of vibrational modes

Vibrational properties provide an important test of the accuracy of first principles calculations as they give direct information about bond strengths and are easily compared with experimental evidence. Once the equilibrium structure of a molecule has been determined, the dynamical properties can be investigated by displacing each atom in the molecule and calculating the resultant forces on all atoms. The magnitude of the displacements must be chosen such that they are small enough to be within the harmonic regime but large enough to give rise to measurable restoring forces. The effect of anharmonicity can be greatly reduced by making positive and negative displacements about the equilibrium positions and averaging the corresponding restoring forces. This procedure can be used to construct a dynamical matrix of dimension $3N \times 3N$ where N is the number of atoms in the molecule. Subsequent diagonalisation of this matrix gives directly all $3N - 6$ normal mode vibrational frequencies and their associated eigenvector displacement patterns [114, 115]. The results of the calculation on benzene and 5CB are shown in the following Section, along with comparison to experimental data and other calculations. It should be noted that the diagonalisation of the forces to give the vibrational frequencies was performed by Dr. S. J. Clark.

3.4.2 Calculated vibrational frequencies of benzene

The harmonic vibrational frequencies of benzene were calculated and are summarised in Table 3.7. Benzene has 30 vibrational modes of which there are 20 distinct frequencies. Column 1 gives the labelling for the 20 distinct modes. The mode symmetries were assigned from the examination of the phonon eigenvectors which were determined when the dynamical matrix was diagonalised. Individual drawings of all the modes can be found in [91]. Column 2 shows the estimated harmonic frequencies derived

by Goodman *et al.* [89] using experimental data for the fundamentals and subtracting the anharmonic corrections. Column 3 shows the results from this work. Percent differences from the Goodman predicted harmonic frequencies are indicated in parentheses. Column 4 gives HF (SCF) calculated values obtained with a TZ2P (triple zeta plus two polarisation functions) basis set [91]. Column 5 shows the frequencies calculated from MP2 values with a 6-31G** basis set [89]. Column 6 gives the MP2 values with a (TZ2P) basis set [91] and Column 7 shows CCSD values [88] obtained using a contracted, correlation-consistent valence triple zeta set (cc-VTZ). Column 8 gives the frequencies calculated with a HF-DFT hybrid method using BLYP correlation functional and again a (TZ2P) basis set [91].

Previous studies have shown that Hartree-Fock calculations substantially overestimate the benzene vibrational frequencies for all basis sets and that, in particular, the largest discrepancies are found for the CH stretch modes [89]. This is clearly illustrated in the Table which shows that the percentage differences for the HF results are on average several percent too high. Second-order Møller-Plesset theory improves the agreement with experiment. However, both sets of MP2 results and those of the DFT-BLYP calculations fail particularly badly for the B_{2u}. This mode is very badly described by these methods, MP2 in particular, as they tend to overestimate the relative movement of the C atoms [91]. Apart from this one mode and the HF results, all the methods are in reasonable agreement with experiment, differing on average by a few percent. Careful examination shows the results from this work and those from the DFT-BLYP calculation give the best agreement with experiment.

3.4.3 Calculated vibrational frequencies of 5CB

In addition to benzene, the 108 harmonic vibrational modes of 5CB were also calculated [115]. Figure 3.5 shows the frequencies of all normal modes as tick marks along the bottom of the graph. On the plot is also the results of room-temperature Raman scattering measurements [116]. A full symmetry analysis of all the modes has not been

Sym.	Obs.	This work	HF	MP2(6-311G**)	MP2(TZ2P)	CCSD	DFT-BLYP
A_{1g}	994	1006(1.2%)	1070(7.6%)	1015(2.1%)	1018(2.4%)	1012(1.8%)	1015(2.1%)
A_{1g}	3191	3260(2.1%)	3352(5.0%)	3240(1.5%)	3242(1.6%)	3228(1.2%)	3195(0.1%)
A_{2g}	1367	1351(-1.7%)	1491(9.0%)	1367(0.0%)	1374(0.5%)	1391(1.7%)	1360(-0.5%)
E_{2g}	608	597(-1.8%)	662(8.8%)	610(0.3%)	608(0.0%)	613(0.8%)	606(-0.3%)
E_{2g}	3174	3208(1.0%)	3323(4.7%)	3215(1.3%)	3217(1.35%)	3204(0.9%)	3198(0.8%)
E_{2g}	1607	1607(0.0%)	1774(10.3%)	1645(2.3%)	1637(1.8%)	1672(4.0%)	1616(0.6%)
E_{2g}	1178	1181(0.25%)	1280(8.6%)	1199(1.7%)	1195(1.4%)	1207(2.4%)	1161(-1.4%)
B_{1u}	1010	1008(-0.2%)	1090(8.0%)	1009(-0.1%)	1039(2.9%)	1025(1.5%)	1030(1.9%)
B_{1u}	3174	3199(0.8%)	3311(4.3%)	3204(0.9%)	3218(1.4%)	3189(0.5%)	3202(0.8%)
B_{2u}	1309	1339(2.3%)	1335(1.9%)	1451(10.8%)	1461(11.6%)	1304(-0.3%)	1435(9.6%)
B_{2u}	1150	1120(-2.6%)	1180(2.6%)	1173(2.0%)	1178(2.4%)	1166(1.4%)	1145(-0.4%)
E_{1u}	1038	1042(0.4%)	1128(8.6%)	1063(2.4%)	1074(3.4%)	1071(3.2%)	1050(1.1%)
E_{1u}	1494	1476(-1.2%)	1629(9.0%)	1509(1.0%)	1515(1.4%)	1528(2.3%)	1489(-0.3%)
E_{1u}	3181	3224(1.35%)	3341(5.0%)	3231(1.5%)	3238(1.8%)	3221(1.3%)	3212(0.9%)
B_{2g}	990	993(0.3%)	1118(12.9%)	-	-	-	978(-1.2%)
E_{2u}	967	962(-0.5%)	1099(13.6%)	-	-	-	951(-1.6%)
B_{2g}	707	722(2.1%)	769(8.7%)	-	-	-	720(1.8%)
E_{2u}	398	399(0.25%)	448(12.5%)	-	-	-	392(-1.5%)
A_{2u}	674	667(-1.0%)	755(12.0%)	-	-	-	617(-8.4%)
E_{1g}	847	833(-1.6%)	954(12.0%)	-	-	-	827(-2.3%)

Table 3.7. This table shows the observed harmonic frequencies of benzene and those from this work (the units are in cm^{-1}). Also shown, are results from several commonly used quantum chemistry methods and basis sets. Apart from the HF results and the B_{2u} mode, agreement with experiment to better than 0-4% is obtained in most cases. Some quantum chemistry methods do not calculate the out of plane modes.

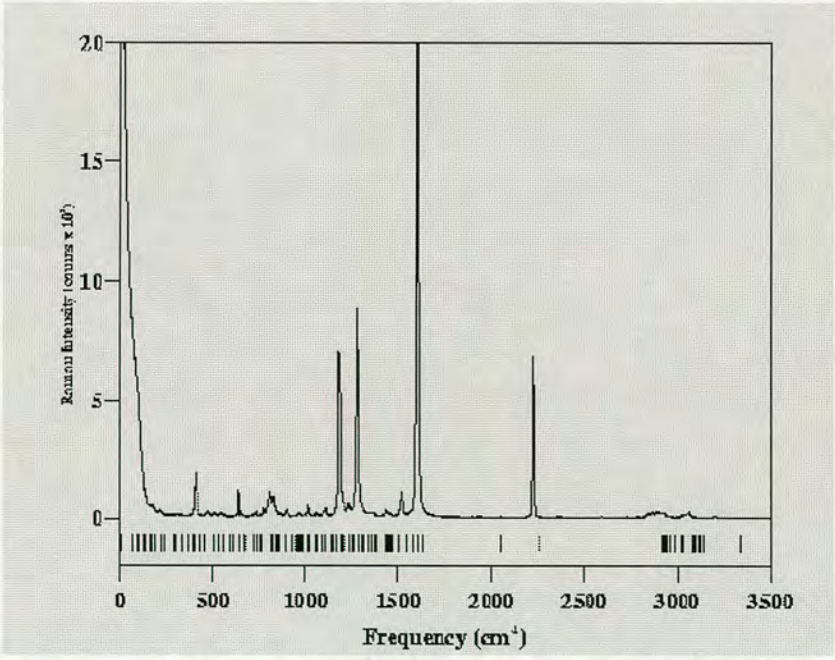

Figure 3.5. The calculated vibrational frequencies for an isolated molecule of 5CB are shown as vertical tick marks running along the bottom the figure. Also shown for comparison is the room temperature Raman spectra of 5CB obtained by Dr. H, C. Hsueh *et al.* [116].

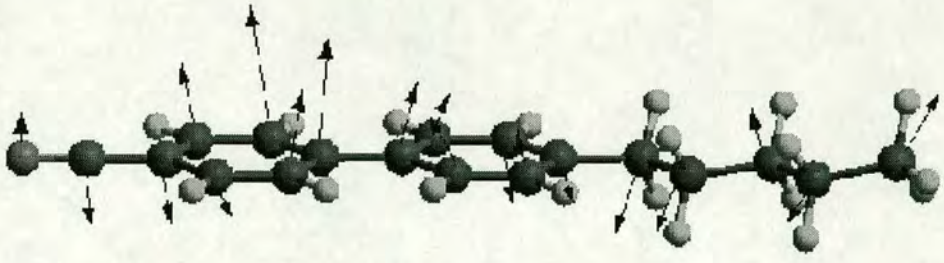

Figure 3.6. A selected normal mode eigenvector of the 5CB molecule is schematically drawn. The arrow at each atom indicates the direction and relative magnitude of motion that the atom vibrates under excitation of the mode. The mode shown is the low frequency (166cm^{-1}) standing wave-like mode. Information about the actual displacements of atoms such as this is inaccessible to experiment. However the atomic displacements can be seen to form a motion similar to a standing wave on the molecule. The nodes of this standing wave appear to occur on the C≡N bond, on the right phenyl group, and half way along the pentyl chain.

performed and, therefore, only frequencies are compared. In general a large number of modes with frequencies up to about 1630 cm^{-1} are found. On examination of the eigenvectors for these vibrational modes, it is found that these correspond to molecular bond bending and torsional modes. The calculation also shows good agreement at the higher frequencies near 3000 cm^{-1} which is dominated by C-H stretching modes. In between these two regions, two more modes were found having frequencies of 2054cm^{-1} and 2255cm^{-1} . Upon examination of the calculated eigenvectors, the former of these modes is associated with a pure $C \equiv N$ stretch. The latter mode is not observed in the spectrum and it was concluded that is was Raman silent. It was not possible to calculate the Raman line intensity since this requires the molecular polarisability. Figure 3.6 shows the motion of the molecule frozen in time for one of the lowest frequency modes.

3.5 Summary and conclusions

In this Chapter structural properties were determined for small test molecules (Section 3.3.1), mesogenic fragments with both internal rotations (Section 3.3.2 and dipolar

regions (Section 3.3.3), and the mesogenic molecule 5CB. The harmonic vibrational frequencies for benzene and 5CB were calculated also (Section 3.4). For all the molecules studied, the results were found to compare well with experimental and other theoretical calculations. The Chapter has shown that the pseudopotential plane wave total energy method used in this thesis, is capable of determining structural and dynamic properties of mesogenic molecules and fragments to a high level of accuracy. Since no experimental input is required, the technique can be applied to as yet unsynthesised molecules with the same level of reliability and can thereby contribute to the exploration of structure-property relationships in liquid crystals.

Chapter 4

Torsional Potentials And Their Transferability

4.1 Introduction

Mesogenic molecules are low-symmetry flexible objects with complicated intra and inter-molecular interactions. Computer simulations, ranging from hard spheres joined by flexible links [24] to atomistic-level treatments [117], have shown that molecular flexibility strongly influences liquid crystal properties. In atomistic simulations, the intra-molecular potentials are modelled using force fields where bond stretching, bond bending and internal rotation are the main contributers to the internal energy. The potential energy for one conformer is expressed as a sum of bonded interactions (bond stretching, bond angle bending, dihedral angle torsions) and non-bonded interactions (Lennard-Jones interactions and electrostatic). The sum of all the terms is referred to as a force field. The MM2 and MM3 force fields as developed by Allinger [118, 119] (MM3, the successor to MM2 can also reproduce vibrational frequencies), are most commonly used for investigations of mesogenic molecules [120].

The parameterisation of these force fields relies on both experimental and *ab initio* data on torsional potentials. In general, it is a difficult task to routinely extract

torsional potentials from experiment, although a combination of diffraction, optical spectroscopy and NMR studies can provide some quantitative information [101, 116, 121, 122]. This Chapter explores the torsional potentials of several mesogenic fragments which are found in a wide range of liquid crystalline molecules. An investigation is made of transferability of torsional potentials between molecules. Throughout, an attempt is made to define the criteria required for transferability and understand the circumstances in which transferability of potentials is expected to be preserved.

The Chapter begins by investigating the influence of geometry optimisation on torsional potentials and their transferability. An examination is then performed on the influence that polar and lateral substituents have on the torsional potentials for the common mesogenic fragments, biphenyl and phenyl cyclohexane. Also determined is the flexibility of alkyl and alkoxy tail groups attached to both benzene and cyclohexane units. For the systems investigated, the transferability is found to depend sensitively on steric factors and molecular electronic structure, particularly through the degree of electron delocalisation and dipolar interactions. Since one of the continuing aims of *ab initio* investigations is the development of reliable force fields for real mesogenic molecules, the transferability of fragment-derived potentials to 5CB is also explored. This is achieved by examining the coupling between the inter-ring torsion and flexible alkyl tail for 5CB.

4.2 Geometry optimisation

The following Sections investigate the influence that geometry optimisation has on torsional potentials and their transferability. Potentials relating to calculations where optimisation was performed for each conformer are termed *optimised* potentials. Those potentials which do not involve optimisation for each conformer are termed *non-optimised* potentials. However, the geometry used to construct the conformers for the non-optimised potentials corresponds to an optimised geometry for a single chosen

conformation. Specific details of the optimisation method can be found in the earlier Section 3.2.2. In terms of computational cost, geometry optimisation is expensive, sometimes increasing the computational resources required six fold. However, as the following sections will show, optimisation is necessary to acquire accurate torsional potentials and investigate transferability.

4.2.1 Influence on torsional potentials

Butane

Figure 4.1 displays the optimised and non-optimised potentials for rotation about the central C-C bond in butane, in which the lowest energy conformation (*trans*) is at 0°, the highest (G/G-barrier) at 180°, and a local minimum (*gauche*) occurs at 113°. Examination of the two potentials shows that although there is reasonable similarity between them, they predict significantly different energies for the various stationary points. This can be clearly seen from Table 4.1, which tabulates the relative energy differences of the stationary points with respect to the global *trans* minimum. Also tabulated are results from experimental observation, empirical forces fields and other *ab initio* work including a DFT plane wave pseudopotential calculation.

The Table shows, not surprisingly, that it is the optimised results which are in much better agreement with experimental observations and other *ab initio* work. The relative energies for the optimised potential, apart from an overestimation of the *gauche* energy of $\approx 0.2 kcal/mol$ (30%), are in good agreement with those of the CISD/CCSD [93] calculations (few percent). This excellent agreement is particularly remarkable for the G/G barrier for which has been the subject of discussion for some time [95]. Recent *ab initio* calculations have shown [93, 123] that in conventional quantum-chemical schemes, large basis sets and extensive treatment of electron correlation are necessary to obtain an accurate value for this barrier. The non-optimised potential over estimates the G/G-barrier by approximately 2 kcal/mol ($\approx 30 - 40\%$) in comparison with

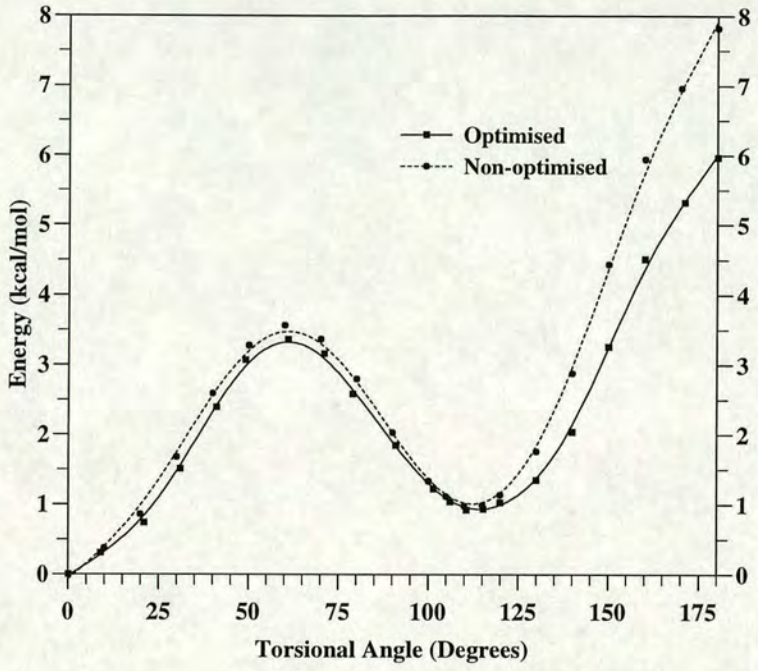

Figure 4.1. Potentials for rotation about the central C-C bond in butane. Energies are given in kcal/mol (1kcal/mol=4.418kJ/mol). Although not shown in the Figure, the functions should be symmetric at 0° and 180°.

Method	Ref.	anti	G/T-barrier	Gauche	G/G-barrier
This work (non-optimised)		0.0	3.50	1.06	7.83
This work (optimised)		0.0	3.35	0.91	5.90
CISD/CCSD(T)[a]	[93]	0.0	3.31	0.62	5.50
CCSD[b]	[123]	0.0	3.33	0.69	5.25
DFT (GC-BP)[c]	[95]	0.0	3.0	0.9	5.5
MP2/6-31G*	[124]	0.0	3.45	0.60	5.99
CHARMM	[125]	0.0	3.32	0.70	5.1
RB	[126]	0.0	2.95	0.70	10.7
Expt	[95][d]	0.0	3.1-3.8	0.7-1.0	4.5-4.9

[a] Results obtained from extrapolation from a table which was constructed such that one axis listed the basis set in order of increasing completeness and the other incrementally improved levels of correlation. The assumption made is the most reliable results are found along the diagonal which matches basis sets to level of theory.
[b] A variety of basis sets are used including double zeta with polarisation (DZP)
[c] DFT with a plane wave basis set and gradient corrections (GC) using the Becke [49] and Perdew [127] parameterisations, norm-conserving pseudopotentials, cutoff energy of 500eV and Car-Parrinello minimisation.
[d] and References therein.

Table 4.1. Relative energy differences of the four stationary points as described in the text with respect to the global *trans* minimum. Energies are given in kcal/mol.

CCSD, highlighting the importance that that geometry optimisation has in obtaining an accurate potential. The experimental values for the stationary points vary over a very wide range. Apart from the G/G barrier, the results from this work are within the range of experimental values. It is interesting to note that all the *ab initio* methods overestimate the G/G barrier in comparison with experimental values.

Also included in the Table are results from two commonly used empirical force fields; CHARMM [125] and RB (after Ryckaert and Bellemans [126]). The potential generated by CHARMM appears to reproduce reasonably well the values from this work and CCSD, whereas the RB potential strongly overestimates the G/G-barrier. The DFT results reported by Röthlisberger *et al.* [95] are similar to those predicted by this work. In their work they also used a plane wave basis set and norm conserving pseudopotentials. The main difference was that they used an exchange-correlation functional of Becke [49] and Perdew [127] as opposed to the Perdew-Zunger [54] parameterisation used in this work.

2-2′ Difluorobiphenyl

The important influence that geometry optimisation has on torsional potentials is even more apparent for the molecule 2-2′ difluorobiphenyl. Figure 4.2 shows both optimised and non-optimised potentials for rotation about the inter-ring C-C bond in 2-2′ difluorobiphenyl. The geometries used to calculate the optimised potential were discussed in Section 3.3.3. The fixed geometry used to calculate the non-optimised potential was chosen to be that of 90^0 conformation. The Figure clearly shows the optimised potential has significantly smaller barrier energies in relation to the non-optimised potential. The differences in barrier heights are particularly large around 0^0 (the *cis* conformer with fluorine atoms adjacent), where the effect of full optimisation is to significantly decrease the barrier height.

The influence of geometry optimisation between the angles of 50° and 140° is not clear from simple inspection of the potentials. The more subtle energy differences in

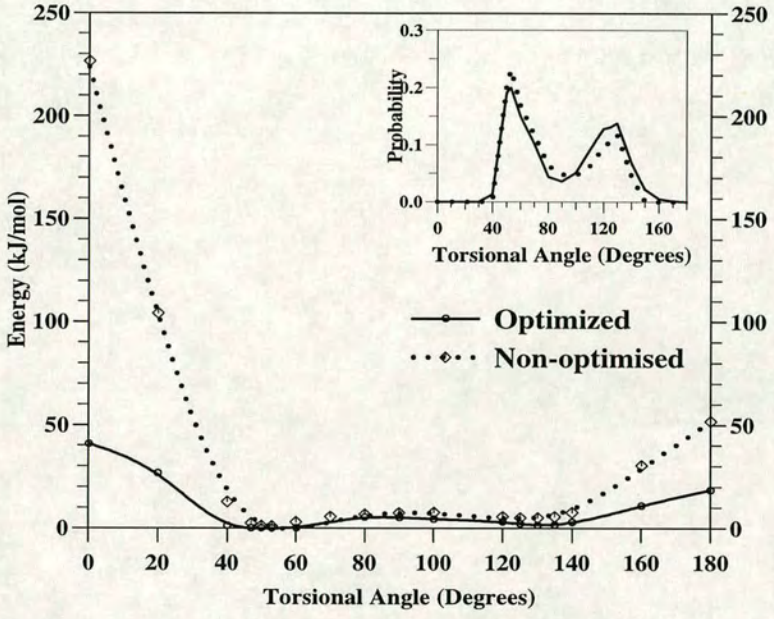

Figure 4.2. Torsional potentials for 2-2′ difluorobiphenyl as determined using both full molecular geometry optimisation for each conformer and fixed molecular bond lengths and angles as described in the text. Calculations were performed at 10° and 20° intervals from $0^0(cis)$ to $180^0(trans)$. The curves (inset) show the relative probabilities of the conformations and the clear preference of the 57^0 to the 130^0 minimum at 300K. This preference was previously discussed in Sec. 3.3.3. Although not shown in the Figure, the functions should be symmetric at 0° and 180°.

this region are better resolved by recasting the energy scale as a probability density. This is done firstly by calculating the Boltzmann statistical partition function [128]

$$Z = \int d\Theta_r e^{-\frac{E(\Theta_r)}{k_B T}} \tag{4.1}$$

which is the normalisation constant for the probability density given by

$$P(\Theta_r) = \frac{e^{-E(\Theta_r)/k_B T}}{Z} \tag{4.2}$$

where k_B is the Boltzmann constant, T is the given temperature, 300K in this case. The plot of the probability as shown in Figure 4.2(inset), clearly indicates that the molecule in the gas phase generally populates only those states between 40° and 160°. Both the optimised and non-optimised results predict similar probabilities. This similarity is in part due to the fact that the geometry used to calculate the non-optimised potential was from the optimised 90° conformer.

4.2.2 Influence on transferability

The influence of geometry optimisation on the transferability of the inter-ring C-C torsional potentials for 5CB and 4-cyanobiphenyl is investigated in this Section. The molecule 4-cyanobiphenyl is the core fragment of 5CB with the alkyl tail removed. It can be seen from Figure 4.3 that the optimised potentials for 5CB and 4-cyanobiphenyl are very similar, suggesting that the potentials are indeed transferable. This conclusion however, would not be drawn if only the non-optimised potentials (inset in Figure) were available, since their dissimilarity suggests otherwise. It is evident therefore, that full structural relaxation is required in order to assess the degree of transferability of the inter-ring torsions. Transferability for 5CB is further discussed later in Section 4.4. All torsional potentials in the preceding Sections are optimised.

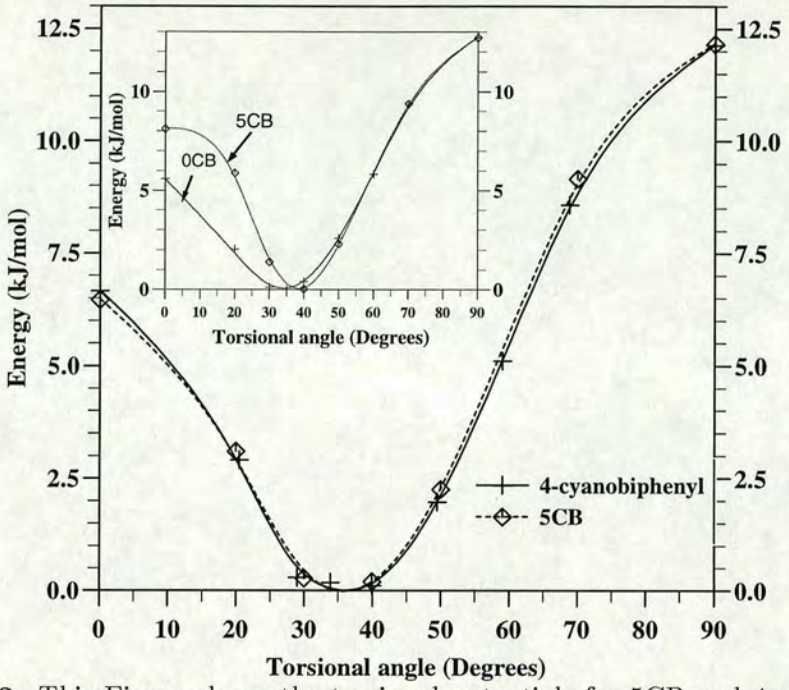

Figure 4.3. This Figure shows the torsional potentials for 5CB and 4-cyanobiphenyl with both optimised and non-optimised structures (inset) as described in the text. The 90° conformer was used for both of the non-optimised potentials. Although not shown in the Figure, the functions should be symmetric at 0° and 90°.

4.3 Transferability for mesogenic fragments

4.3.1 Polar end group substituents

The major contribution to the dielectric anisotropy ($\Delta\epsilon$),which is crucial in determining the electro-optic response is from the permanent dipoles within the molecule. Many liquid crystal molecules contain a highly dipolar substituent such as a cyano group, positioned along the long molecular axis so $\Delta\epsilon$ is large and positive. Here an investigation is made of the influence the polar cyano group has on the potential governing the rotation about the inter-ring C-C bond in biphenyl.

The total energy of biphenyl and 4-cyanobiphenyl was calculated for dihedral angles between 0° and 90° in various step sizes. The total energy as a function of torsional angle is plotted for both systems in Figure 4.4. The potential for 4-cyanobiphenyl is markedly different from the torsional potential of biphenyl. In general the shape of

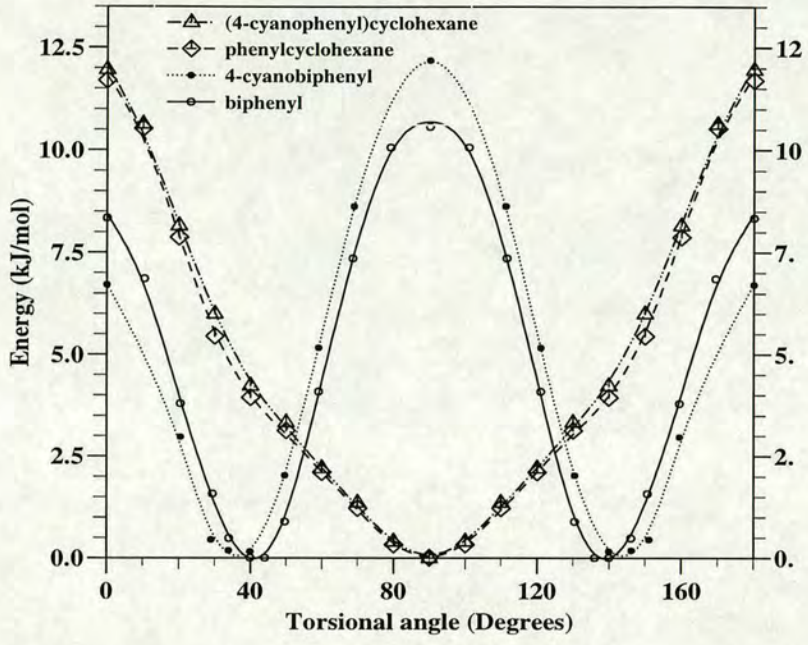

Figure 4.4. This Figure shows the torsional potentials for rotation about the C-C inter-ring bond for 4-cyanobiphenyl, biphenyl, (4-cyanophenyl)cyclohexane and phenylcyclohexane. Although not shown in the Figure, the functions should be symmetric at 0° and 180°.

the potentials are governed by a trade-off between steric repulsion and increased conjugation, which is maximised when the rings are coplanar. Electronic charge transfer towards the highly electronegative cyano group results in subtle bonding and structural effects which influences this trade-off. These are sufficient to change both the barrier heights and position of the minimum, as can be seen from Figure 4.4. To determine whether this charge transfer mechanism is specific to aromatic biphenyl, the same calculations were also performed on the molecules phenylcyclohexane and (4-cyanophenyl)cyclohexane, where fully saturated cyclohexane rings prevent delocalisation occurring over the whole molecule. The torsional potentials for both systems, as also shown in Figure 4.4, are almost identical. As expected, the cyano group does not have a significant effect on the torsional potential as there are no π-electrons enabling it to influence the electronic distribution. The shapes of the torsional potentials are, in contrast to those for biphenyl and 4-cyanobiphenyl, governed by the steric repulsion

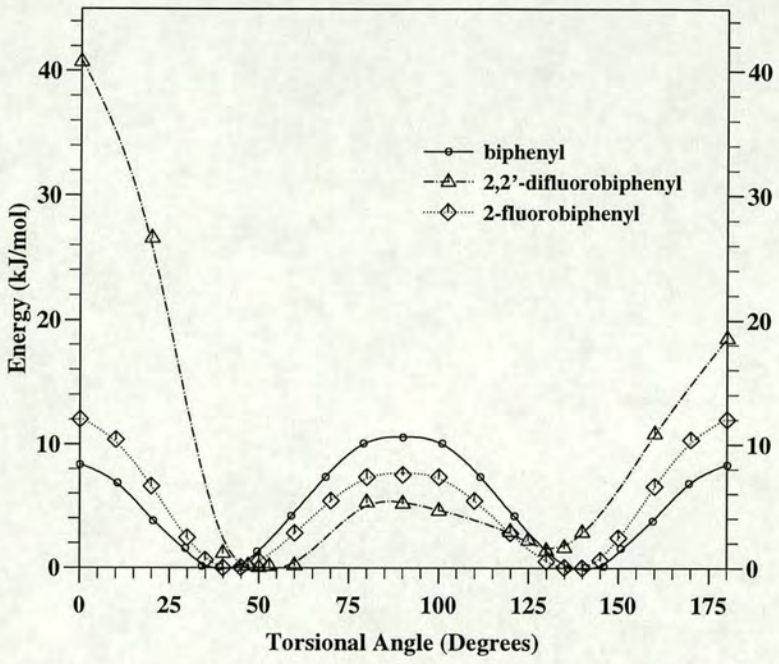

Figure 4.5. This Figure compares the torsional potentials for biphenyl, 2-fluorobiphenyl, 2,2′-difluorobiphenyl. Although not shown in the Figure, the function should be symmetric at 0° and 180°.

of the hydrogens.

It was found that the influence of a polar terminal group on transferability, depends on the degree of electron delocalisation in the fragment. In the present example, the effect of cyano substitution is appreciable for biphenyl and negligible for the phenyl-cyclohexane, which leads to the conclusion that the transferability of the inter-ring C-C torsional potentials depends on the electronic structure of the two ring systems. While it has been have shown that the inter-ring C(aromatic)-C(cyclohexane) torsional potential is transferable in the presence of a polar terminal group, for the C(aromatic)-C(aromatic) it is not.

4.3.2 Polar lateral substituents

This Section explores the inter-ring C-C torsional potential between aromatic rings in the presence of fluorine substituents. As has been previously discussed in Sections

3.3.3 and 4.2.1, the addition of fluorine atoms results in strong electrostatic interactions which can significantly affect the internal dynamics and overall molecular shape. The molecule 2-fluorobiphenyl has one substituted fluorine atom on the hydrogen position adjacent to the inter-ring bond. Figure 4.5 shows the torsional potentials for 2-fluorobiphenyl and 2,2′-difluorobiphenyl in comparison to that of biphenyl. Considering first the torsional potential for 2-fluorobiphenyl, it can be seen that the barrier heights with respect to biphenyl have changed although the minimum is unaffected. For the 0° conformer, the barrier height increases by approximately 4 kJ/mol due to the additional steric effect of the fluorine atom. At 90°, the barrier is reduced by a comparable amount. It is plausible this is due to the highly electronegative fluorine attracting electrons from the delocalised π-orbitals and therefore reducing the energy cost of distortion from the 0° conformation.

The nature of the intramolecular interactions changes significantly in the molecule 2,2′-difluorobiphenyl. The barrier height to rotation through the 0°(coplanar *cis*) conformation increases greatly, as expected, due to both the steric hindrance and electrostatic repulsion of the fluorine atoms. At the 90° conformation, the barrier height is even lower than in the single fluorine case for similar reasons to those discussed for 2-fluorobiphenyl.

4.3.3 Combined tail and core segments

There are often several bond rotational motions in mesogens which are important in determining their physical properties. In particular, characteristics of the potential governing rotation about ring-tail bond can have a large influence on conformational shape. This Section investigates the effect that combining alkoxy and alkyl tail groups, with either benzene or cyclohexane, has on the torsional potential for this bond. Combinations of these groups are commonly used in liquid crystal synthesis and are responsible for some interesting structure-property relationships. For example, although cyclohexane is considered inferior to benzene as a central linking unit, it has been found that

this conclusion does not extend to the situation when cyclohexane is substituted for the phenyl ring positioned next to the alkyl tail in 5CB. Properties of cyclohexane analogues of 5CB discussed by Gray [2], illustrate that the this particular cyclohexane substitution leads to a broadening of the nematic range.

In this Section potentials for three molecules are calculated: n-pentylcyclohexane, n-pentylbenzene and methoxybenzene. The first two are chosen to establish the trends in hydrocarbons and the third to demonstrate the additional effect of the non-bonding lone pair electrons in oxygen. Figure 4.6 shows the torsional potentials for these molecules. In all cases the molecules have an all-trans tail and the 0° conformation corresponds to the tail being parallel to the plane of the ring system.

Considering first methoxybenzene, the torsional potential has the appearance of a sinusoidal curve with 2-fold symmetry. The potential corresponds to rotation about the C-O bond, where the oxygen has one further bond (to the methyl group) and the carbon is bonded to two neighbours in the benzene ring. It can be seen that there is a strong minimum at the planar 0° conformation and a maximum at 90°, which is consistent with NMR studies of orientation of the ethoxy group in 4-ethoxy-4′-cyanobiphenyl in the nematic mesophase [129]. The preference for the planar structure can be attributed to the additional electron density donated from the oxygen lone pair strengthening the C-O bond.

By analogy with methoxybenzene, the torsional potential for n-pentylbenzene also has stationary points at the 0° (180°) and 90° (270°) conformations and 2-fold symmetry. However the potential corresponds to rotation about a C-C bond, as opposed to a C-O bond. Since there are no additional delocalised electrons from an oxygen atom to contribute to the bonding in the planar structure, the tail adopts the 90° conformation which maximises the distance between ring and tail atoms. This result is in exact agreement with *ab initio* and microwave spectrum calculations of ethylbenzene [130]. It is found there that a conformation in which the ethyl group is also perpendicular to the phenyl group is the most stable. The observation that the 0° conformation is

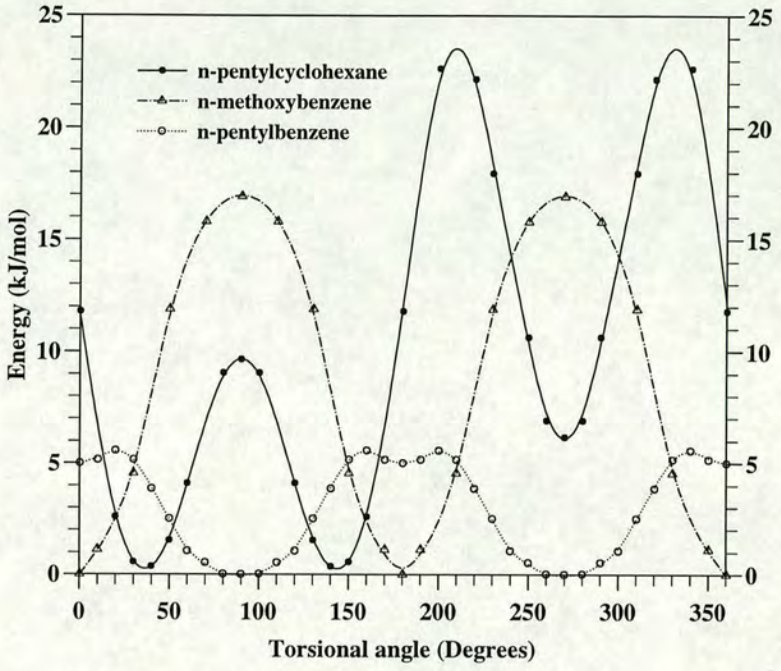

Figure 4.6. This Figure shows the full 0° to 360° torsional potentials for n-pentylcyclohexane, n-pentylbenzene and n-methoxybenzene. Although not shown in the Figure, the function should be symmetric at 0° and 360°.

also a shallow minimum can be understood by noting that although it maximises the ring-tail repulsions, it minimises the steric repulsion between nearest hydrogen atom on the ring and those on the first tail carbon. These repulsions increase as we rotate away from 0° leading to a maximum near their closest approach at 15°.

Finally, n-pentylcyclohexane is yet more complicated as the carbon atoms in the cyclohexane group have additional hydrogens. Figure 4.7 shows a schematic illustration of the molecule in the 0° conformation and the subsequent direction of rotation. The torsional potential is most easily understood by considering interactions between the hydrogens in the vicinity of the torsional bond. More specifically, the interactions occur between three sites: the single hydrogen bonded to the carbon at the ring end of the bond (ring H), the pairs of hydrogens bonded to the neighbouring carbons on the ring (neighbouring ring H pair) and the pairs of hydrogens bonded to first and second tail carbon (1^{st} or 2^{nd} tail H pair). The torsional potential has three barriers to rotation and three stable conformational states. The three maxima at 90°, 210° and

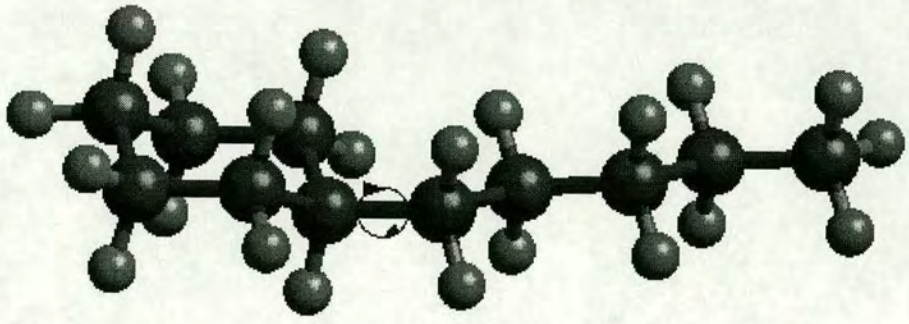

Figure 4.7. This Figure shows the molecule n-pentylcyclohexane which has the most complex torsional potential, in the 0° conformation and the direction of rotation which is clockwise.

330° correspond to eclipsed conformations. The 90° conformation has the 1^{st} tail H pair eclipsed with the ring H, while the 210° and 330° conformations have the 1^{st}tail H pair eclipsed with the two neighbouring ring H pairs. The three minima at 30°, 150° and 270° correspond to the anti-eclipsed conformations. The result that the minimum at 270° is less favoured than the 30° and 150° minima as shown in Figure 4.6, can be understood by noting that the repulsion between ring H and 1^{st} tail H pair, is stronger than that between the ring H and the 2^{nd} tail H pair. It is thus concluded that while the ring-tail torsional potential is not transferable, the energetics can be better modelled by considering non-bonding interactions between atoms on either side of the bond. In the case of hydrocarbons such interactions are repulsive, but for electron donors such as oxygen they can be attractive.

4.4 Transferability in 5CB

The preceding Sections have focussed on intra-molecular torsional potentials of constituents of typical thermotropic mesogens. However, in large liquid crystal molecules

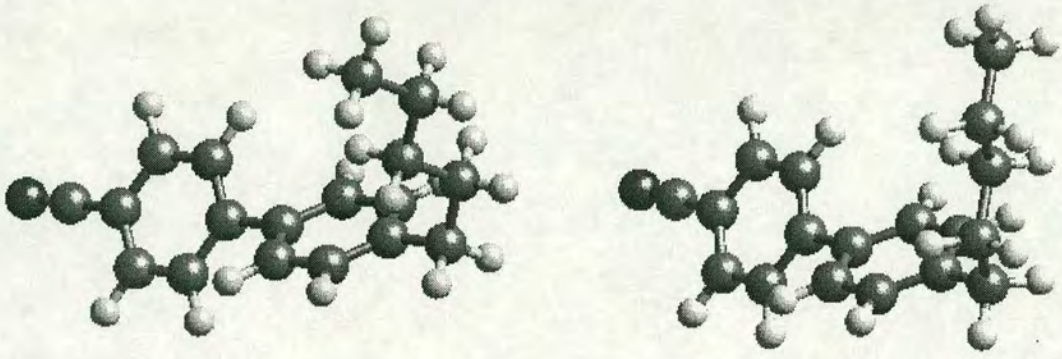

Figure 4.8. Figure (a)(on the left) shows the 5CB conformer *gtt+* and (b)(right) shows the conformer *gtt−*.

it is conceivable that coupling may exist between each segment of the molecule and resulting shape changes of distant segments may influence transferability. To investigate this coupling this Section explores the influence of tail flexibility on the inter-ring torsion for the specific case of 5CB.

4.4.1 Tail conformations

The flexibility of 5CB is governed by rotations about the inter-ring bond, ring-tail bond and four C-C bonds in the tail. Although the minimum energy conformation is known to have an inter-ring torsional angle of 36.0° and an alkyl tail which lies perpendicular to the adjoining phenyl ring, less is known about the conformational properties of the alkyl tail. Although the rotational potential about the 4th C-C bond in the tail, which attaches the terminal methyl group, can be assumed to have three-fold symmetry, the remaining three C-C bonds can each occupy one of the different conformational states denoted by *trans* (t), *gauche+* ($g+$) and *gauche−* ($g-$). The conformational distribution of 5CB will be dominated by the 27 possible combinations of these states. Although the comparison shown in Figure 4.3 suggested there is minimal coupling between segments in 5CB as the torsional potential for 4-cyanobiphenyl was

transferable, this only involved the all trans tail conformer (ttt). It is therefore necessary to investigate transferability for all 27 tail conformers. Figures 4.8(a) and (b) are schematic representations of two of the 5CB conformers investigated; *gtt+* and *gtt−*. Although both of these conformers have the same tail conformation *gtt*, they differ in the relative orientation of the inter-ring torsion to the tail segment. This is the only distinction between the conformers and the orientation is indicated by a + or − in the 5CB conformer label.

Table 4.2 shows the total energies and corresponding relative probabilities for the 5CB conformers as calculated by DFT using MM3 optimised structures [131] (DFT-MM3), DFT using DFT optimised structures(DFT-DFT) and the MM3 force field using MM3 optimised structures(MM3-MM3). In all cases the magnitude of the inter-ring torsional angle is set to a value of 36°(the equilibrium angle as discussed in Section 3.3.4). Examination of the probabilities in Table 4.2 show that the majority of the probability distribution is taken up by seven 5CB conformers, namely; *ttt*, *g+tt*, *g−tt*, *tg+t*, *tg−t*, *ttg+* and *ttg−*. Their relative probability accounts for approximately 77% of the probability distribution at room temperature. Table 4.3 displays the relative energies for these seven conformers only. The Table shows, however, there are significant differences in the results predicted by each calculation. The implications of these differences are discussed in the following sections.

Order of preference

As Table 4.3 shows, all three calculations predict that the *ttt* and *gtt* tail conformers are significantly more favourable than *ttg* and *tgt*. The results indicate that *gauche* conformers are more likely for the dihedral angle nearest to the core which results in a molecular structure which is considerably bent. This suggests that there is an attractive interaction occurring between the tail and the core which stabilises this conformer. All three calculations also agree that the energy difference between *trans* and *gauche* conformations (E_{tg}) changes depending on the position in the alkyl tail.

Conf.	Energy(kJ/mol)			Probability		
	DFT-DFT	DFT-MM3	MM3-MM3	DFT-DFT	DFT-MM3	MM3-MM3
g−g−g−	8.34	9.02	8.36	0.87	0.71	0.93
g−g−t	5.05	5.66	4.51	3.25	3.45	4.34
g−g−g+	18.51	17.16	14.96	0.01	0.03	0.07
g−tg−	6.02	6.43	5.52	2.21	2.34	2.91
g−tt	2.03	3.10	2.56	10.89	11.55	9.49
g−tg+	5.61	6.01	6.19	2.60	2.75	2.23
g−g+g−	16.80	17.31	13.29	0.03	0.03	0.13
g−g+t	12.74	14.03	7.36	0.15	0.16	1.39
g−g+g+	14.72	15.07	9.36	0.07	0.07	0.63
tg−g−	5.95	5.76	6.48	2.27	2.39	1.98
tg−t	2.81	3.35	3.60	7.95	8.43	6.26
tg−g+	13.19	14.25	13.79	0.13	0.09	0.11
ttg−	2.95	4.01	3.42	7.53	5.22	6.73
ttt	0.00	0.00	0.00	24.48	26.04	26.40
ttg+	2.93	3.92	3.42	7.60	5.38	6.73
tg+g−	13.07	14.56	14.59	0.13	0.14	0.08
tg+t	2.85	3.40	3.65	7.84	8.30	6.14
tg+g+	5.40	5.04	6.23	2.82	2.99	2.19
g+g−g−	15.17	16.37	9.40	0.06	0.04	0.61
g+g−t	12.10	14.50	7.77	0.19	0.20	1.18
g+g−g+	17.14	18.92	22.70	0.03	0.01	0.00
g+tg−	6.04	7.74	6.23	2.19	2.31	2.19
g+tt	1.99	3.19	2.12	11.03	11.71	11.31
g+tg+	6.29	8.57	6.35	1.98	2.09	2.08
g+g+g−	18.52	19.04	15.42	0.01	0.01	0.06
g+g+t	5.33	6.71	5.60	2.91	3.07	2.81
g+g+g+	8.64	9.63	8.11	0.77	0.55	1.03

Table 4.2. Energies and probabilities for the 27 conformations of 5CB. The probabilities are calculated using a Boltzmann partition function at a temperature of 300K. All three calculations predict the all *trans* conformer to be the most populated state. They do however predict a different order of preference for the other conformers.

Calculation method	5CB Conformer						
(Method-Structures)	*ttt*	*g+tt*	*g−tt*	*tg+t*	*tg−t*	*ttg+*	*ttg−*
DFT-DFT	0.00	1.99	2.03	2.81	2.84	2.93	2.94
DFT-MM3	0.00	3.19	3.10	3.40	3.35	3.93	4.01
MM3-MM3	0.00	2.12	2.56	3.65	3.60	3.42	3.42

Table 4.3. The relative energies (kJ/mol) of the seven most highly populated conformers of 5CB.

This is in contradiction to the rotational isomeric state (RIS) model of Flory [132] which is often used to predict the structures of mesogenic molecules. In the RIS model, the internal energy (gas phase energy) is:

$$U_{int}(n) = N_g E_{tg} + N_{g\pm g\mp} E_{g\pm g\mp} \tag{4.3}$$

where N_g is the number of *gauche* segments, $N_{g\pm g\mp}$ is the number of $g\pm g\mp$ sequences and $E_{g\pm g\mp}$ is their corresponding energy increments to the internal energy U_{int}. In this form of the RIS model, a single energy term is used for the contribution in internal energy due to a *gauche* conformation regardless of its position in the tail. The results shown in the table indicate this is not the case.

Table 4.3 indicates that the DFT-DFT and DFT-MM3 calculations predict the same order of preference for the tail conformations: $ttt > gtt > tgt > ttg$. The MM3-MM3 calculation predicts a similar order, except that the *ttg* tail conformer is preferred to the *tgt*. The MM3-MM3 order of preference is: $ttt > gtt > ttg > tgt$. Closer inspection of the total energies for MM3-MM3 in comparison with DFT-MM3, reveals that the MM3 force field also shows a distinct preference for the *gtt* tail conformer in addition to favouring the *ttg* conformer. The MM3-MM3 total energies for both the *gtt* and *ttg* tail conformers are lower than the corresponding total energies calculated by DFT-MM3, whereas for the *tgt* conformer, the MM3-MM3 total energy is higher than that of

DFT-MM3. Interestingly, the two conformers *gtt* and *ttg* for which MM3-MM3 shows a preference, are similar in that both represent situations where the tail is bent back on itself and hence comes closer to the 4-cyanobiphenyl group.

Accuracy of method

It is apparent from the results that the differences in the total energies are not only due to the accuracy of the structures used, but also the method used to calculate the total energy. For instance, although the DFT-MM3 and MM3-MM3 calculations use the same structures(MM3), Tables 4.2 and 4.3 show that they predict different energies. For the *gtt* conformers the total energies differ by more than 1 kJ/mol. The results show that careful consideration must be given to the accuracy and reliability of the method used. As MM3-MM3 and DFT-MM3 both significantly overestimate the energies of the investigated conformers, it is evident that the method used both to optimise the structure and calculate the total energy, are equally influential in determining accuracy.

Coupled torsions and transferability of fragment potentials

It had been concluded earlier that the inter-ring torsional potential for 4-cyanobiphenyl is indeed transferable to inter-ring torsions of 5CB for when the tail was in a ttt conformation. This Section determines the transferability of fragment potentials to 5CB with other tail conformers. By using the results for the 5CB tail conformers shown in Tables 4.2 and 4.3, the level of coupling between the inter-ring torsion and the torsions in the tail is investigated. The stronger the level of coupling between segments, the weaker the transferability of fragment potentials to 5CB. This coupling can be measured by noting the influence the orientation of the inter-ring torsion has on the total energy. Any discernible interaction between the tail and inter-ring torsion will be revealed by the dependence that the total energy of each 5CB tail conformer has on the orientation (+ or −) of the inter-ring torsion. The results for the DFT-DFT calculation shown in Tables 4.2 and 4.3, indicate that there is negligible coupling between the

Molecule	Figure	Coefficients						
		c_0	c_1	c_2	c_3	c_4	c_5	c_6
butane	4.1	2.30	-1.02	0.40	-1.72	-	-	-
biphenyl	4.4	5.03	-	-1.96	-	4.61	-	0.61
4-cyanobiphenyl	4.4	5.04	-	-3.55	-	4.25	-	0.74
(4-cyanophenyl)cyclohexane	4.4	4.70	-	5.08	-	1.08	-	0.76
phenylcyclohexane	4.4	4.49	-	4.96	-	1.18	-	0.85
2-fluorobiphenyl	4.5	5.04	-	1.26	-	4.96	-	0.843
2,2′-difluorobiphenyl	4.5	9.21	5.17	10.40	4.65	8.00	1.82	1.32
n-pentylcyclohexane[a]	4.6	4.73	-	-1.45	-	4.51	-	1.37
n-methoxybenzene	4.6	9.262	-	-8.626	-	-0.675	-	0.475
n-pentylbenzene	4.6	2.936	-	2.998	-	-0.351	-	0.492

[a] Also use c_8 =0.80,c_{10} =0.64 and c_{12} =0.40

Table 4.4. Coefficients for the torsional potentials for the molecules investigated in this Chapter. The coefficients are chosen to provide a reasonable fit to 1 decimal place of the calculated points.

inter-ring torsion and tail torsions in 5CB. This negligible coupling suggests that the torsional dynamics of 5CB can be modelled by superimposing fragment potentials for the different segments of the molecule.

4.5 Parameterisation of the torsional potentials

In order that the potential surfaces described in this Chapter can be implemented elsewhere, a parameterised function has been fitted to the torsional potentials. The potentials can be easily fitted by a cosine function expressed as:

$$V(\Theta_r) = \sum_{n\in\{S\}} c_n \cos(n\Theta_r), \tag{4.4}$$

where $\{S\}$ is the set of indices to be summed over.

The values of the coefficients, c_n, are given in Table 4.4.

4.6 Summary and conclusions

The degree to which potentials which determine molecular flexibility in liquid crystals are transferable between different intramolecular environments has been explored. Based on the results obtained from representative systems common to many thermotropic liquid crystals several conclusions are proposed which are expected to be generally valid. In section 4.3.1 it is found that the degree to which polar substituents in terminal positions affect the transferability of semi-rigid core torsional potentials depends mainly on the extent of electron delocalisation in the core region. Also provided is a detailed quantitative analysis for biphenyl and phenylcyclohexane. In sections 4.3.2 and 4.3.3 the significant effect of steric hindrance is shown by investigating the interaction between substituents on the ring torsion and investigating the substantial 'fifth neighbour' interactions which determine the torsion characteristics of ring-tail bonds. Finally in section 4.4 we show that the effect of the tail on the inter-ring potential of 5CB is negligible provided full relaxation of the tail atoms is taken into account, a conclusion which is vital to the development of accurate intra-molecular potentials for specific molecules.

These results presented in this Chapter will have implications for the parameterisation and use of intramolecular potentials in atomistic-level modelling of liquid phase behaviour. These potentials play a vital role in the development of accurate models for mesogenic molecules which can be used to simulate the behaviour of bulk liquid phases. As such, they play a key part in the advancement of molecular engineering, providing a link between microscopic molecular properties and the collective behaviour of an ensemble of molecules. One of the most important practical questions concerning such potentials is the degree to which they can be used in environments which differ from those in which they have been determined. In general there may be a variety of mechanisms which compromise transferability of potentials generated from model fragments. For example, the intramolecular dynamics may be influenced by charge transfer

between functional groups or electrostatic interactions and steric effects. However, it has been shown that so long as the solvent effects in bulk simulations are accounted for via intermolecular van der Waals and electrostatic interactions, they can be successfully modelled [133, 134].

Chapter 5

Conformation-Dependent Electrostatic Moments

Although the orientational ordering in liquid crystals is believed to arise predominantly from short range forces coupled with a high degree of molecular shape anisotropy [135, 136, 137, 138, 139], longer range interactions may also have an influence on ordering. One contribution to these interactions is the electrostatic interaction between molecular charge distributions. The significance of these interactions in particular has been confirmed by both theoretical studies [140] and computer simulations [32, 141, 142, 143, 144]. The leading term of the electrostatic interaction is given by the lowest non-vanishing permanent electric multipole moment of the molecule. This Chapter investigates the first non-vanishing terms, namely the dipole and quadrupole moments, and their conformational dependence for various mesogenic fragments and 5CB. The Chapter is split into two Sections, the first one deals with molecular dipoles and the second quadrupole moments.

5.1 Molecular dipoles

There have been a number of Monte Carlo (MC) and molecular dynamics (MD) studies which highlight the role dipolar interactions have in influencing mesophase behaviour. The effect of dipolar interactions on the structure and thermodynamical properties of hard spherocylinders was recently examined by McGrother et al. [141] using MC simulations. In that study a point dipole was located at the end of the molecule in the hemispherical cap (spherocylinders consist of a cylinder with hemispherical caps on the end). The dipolar interactions were found to slightly destabilise the nematic phase relative to the isotropic phase when compared with simulations of non-polar hard spherocylinders. The smectic phase was also destabilised to the extent that it was only seen at high densities. Interestingly, this was not the case when the dipole was located at the centre of the hard spherocylinder. Although the effect of the central dipole was also to destabilise the nematic, there was, however, a stabilisation of the smectic phase due to strong anti-parallel dipolar interactions.

Monte Carlo investigations into dipolar interactions by Satoh *et al.* [142, 143] also found the location of the dipole to be important. In their studies they placed the dipole at the centre [142] and the end [143] of a Gay-Berne unit. In the case where the dipole was located in the centre, the transition temperature from the isotropic to nematic phase was found not to be sensitive to the value of the dipole, whereas the transition from nematic to smectic was. The dipolar interaction between particles contributed to a spread in the temperature range of the smectic phase, thereby stabilising it, and producing a similar effect to that seen in the simulation of McGrother *et al.* [141] which used a central dipole. Satoh *et al.* [142] also noted that the population of anti-parallel arrangements was high when the dipole was located in the centre. In the case where the dipoles were placed on the end of a GB unit [143], it was found that the nematic-isotropic transition was shifted towards higher temperature and spread the range of the nematic, an effect that was stronger and opposite to the slight destabilisation seen

by the simulation of McGrother *et al.* [141]. Other studies into dipolar effects have also reported anti-ferroelectric bilayer stripe domains [145] and ferroelectric and anti-ferroelectric columnar phases using dipolar oblate ellipsoids of revolution [146].

In this Section the conformational dependence of molecular dipoles are investigated. In general, it is expected that the molecular dipole will be defined either by a fixed molecular bond or by the relative position of the most electronegative species. In the former case a weak dependence of the molecular dipole on conformation is expected while a more pronounced effect is expected in the later situation. As examples of these cases phenyl benzoate and 2-2′difluorobiphenyl are examined. Phenyl benzoate has a highly polar C=O bond and therefore falls into the former category. The fragment 2-2′difluorobiphenyl is in the second category since the relative positions of the highly electronegative fluorine atoms depend on the dihedral angle between the phenyl groups. Therefore, the molecular dipole is expected to have strong conformation dependence.

Also considered is 5CB, for which the dominant contribution to the molecular dipole is expected to arise from the highly polar CN group. In the case of 5CB, however, the quantitative effects on the molecular dipole from the alkyl chain, cyano group, and phenyl rings are uncertain. Therefore the degree to which the total molecular dipole can be estimated from the individual moments of the mesogenic fragments is assessed, providing insight into the influence of charge transfer. Before proceeding to findings on fragments and mesogens a discussion is first given of test calculations on small molecules.

5.1.1 Molecular dipole moments of test molecules

Once the relaxed electronic structure for a given molecular conformation has been found, the molecular dipole moment can be determined from the electronic and ionic charge distributions. The molecular dipole is a vector quantity and points from the negative to the positive charge. It is calculated as the vector difference between the locations of the centroids of both the electronic and ionic charge distributions, multiplied

Molecule	Dipole Magnitude (Debye)		
	This work	DFT with 6-31G*	Observed
H_2O	1.92	2.09	1.85[a]
HF	1.85	1.84	1.82[a]
HCN	3.08	2.83	2.98 [a]
F-benzene	1.52	-	1.60[b]

[a] From Refs. within [87]
[b] From Refs. within [147]

Table 5.1. This table shows the calculated dipole moments of the small molecules H_2O, HF, CH, HCN and F-benzene (C_6H_5F). Also shown are the experimentally observed values and those calculated using HF-DFT and a 6-31G* basis set [87].

by the total charge. To test the accuracy of the algorithm, tests were performed on the molecules H_2O, HF, HCN and F-benzene, the results of which are shown in Table 5.1. There is a very good agreement with experimental values, with the maximum deviation being approximately 5%. The dipole moment for the non-polar molecule methane was also calculated. The dipole was found to be 0.004 Debye (D), which is expected to be the upper level of noise in the subsequent calculations. This is negligible in relation to the magnitudes found for polar mesogenic fragments and molecules.

Dipole moments can be measured accurately from the Stark effect on rotational spectra of gases. Application of an electric field lifts the degeneracy of the rotational transitions, producing splittings of spectral lines which are proportional to the dipole moment. Alternatively dipole moments can be determined from measurements of the low-frequency dielectric properties of gases and dilute solutions. The *Debye equation* allows polarisabilities and dipoles to be obtained from measurements of permittivity and density as a function of temperature [148]. The equation, however, only applies at sufficiently low frequencies since it assumes the orientation polarisation responds instantaneously to electric field. This method also has drawbacks in that it is not possible to find the absolute direction of the dipole relative to the molecular axes and often dipoles tend to associate through electrostatic interactions which leads to

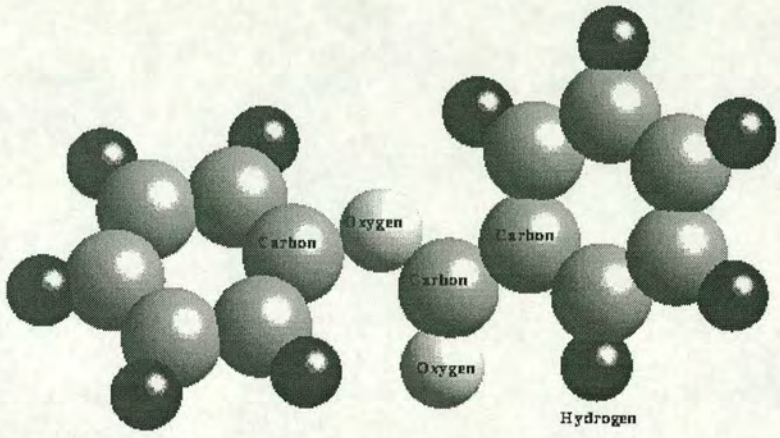

Figure 5.1. Illustration of the molecule phenyl benzoate in its 50^0 conformation

complications in interpreting the results [148].

5.1.2 Dipole moments and internal rotations

Phenyl Benzoate

Phenyl benzoate (an illustration is shown in Figure 5.1) is a widely used linking group and promising molecule in liquid crystal synthesis [149]. The C-O link (the middle rotator) is thought to restrict rotational motions thereby preserving the elongation and rigidity of the molecule [2]. In this Section the dipole for phenyl benzoate is determined for two conformations around the middle rotator; the planar conformation and one with a rotation of 50^0 around the middle C-O rotator. These conformations were chosen on the basis that the C=O double bond, which is thought to be responsible for the majority of the dipole moment (as the oxygen has a lone pair of electrons), is lying in two easily differentiated planes.

The calculation of the dipole moment for the optimised structures of these two conformations show this to be the case. The dipole vector in both conformations was found to be collinear with the C=O bond. However, the magnitude changed with

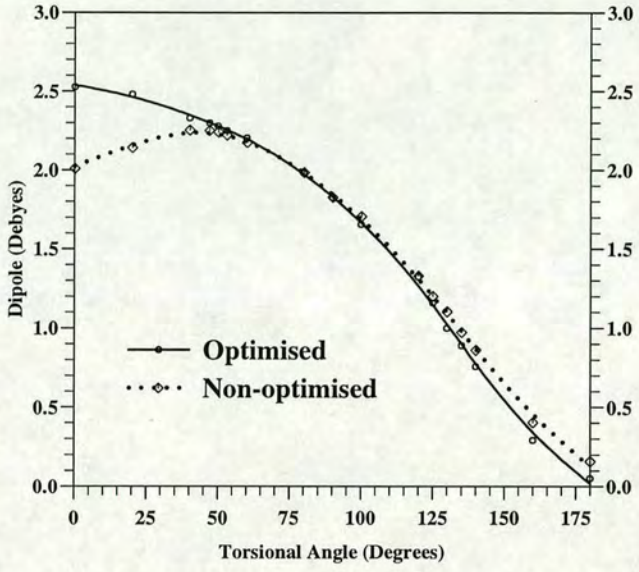

Figure 5.2. The molecular dipole for 2-2′ difluorobiphenyl as a function of torsional angle for both optimised and non-optimised structures.

conformation, increasing from 2.07 D in the planar conformation to 2.45 D for the 50^0 rotation. Although the molecular dipole can mostly be attributed to a specific bond within the molecule, the conformation changed the magnitude by up to 15%. The relative energy differences between the conformations were found to be 20.2kJ/mol with the planar conformation being more stable.

2-2′ Difluorobiphenyl

For the molecule 2-2′ difluorobiphenyl the molecular dipole moment is expected to be a sensitive function of torsional angle, since this governs the relative positions of the fluorine atoms. This is shown to be the case in Figure 5.2, which plots the dipole moment magnitude with respect to torsional angle. It is apparent that the dipole is strongly influenced by conformation but is otherwise relatively insensitive to molecular geometry. The dipole moments for the optimised curve and non-optimised curve approximately converge at 50^0, the same torsional angle at which the energy curves also

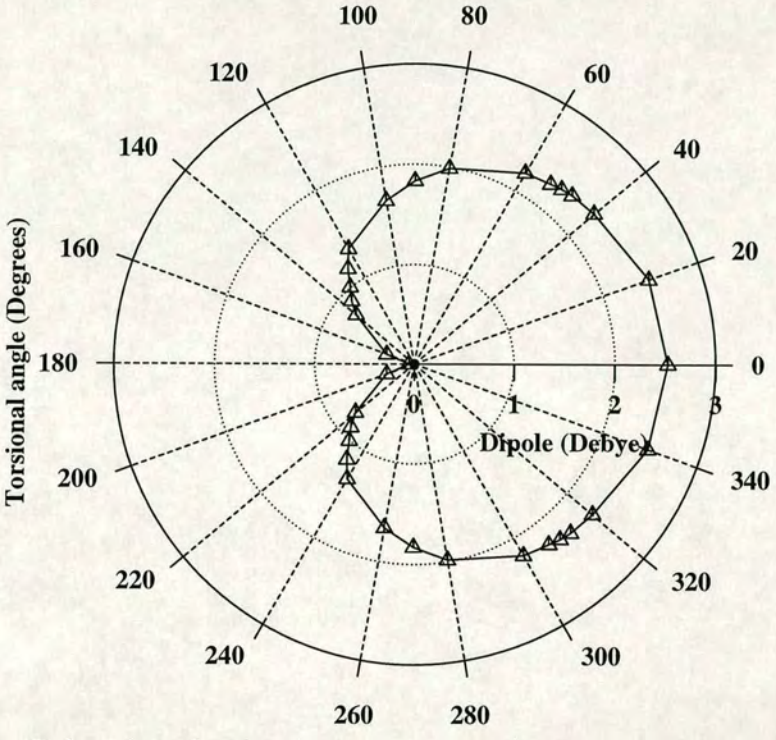

Figure 5.3. Polar plot of molecular dipole for 2-2′ difluorobiphenyl as viewed along the long molecular axis. The torsional angle, Θ_r, is related to the direction of the dipole, Θ_D, by $\Theta_D = \Theta_r/2$.

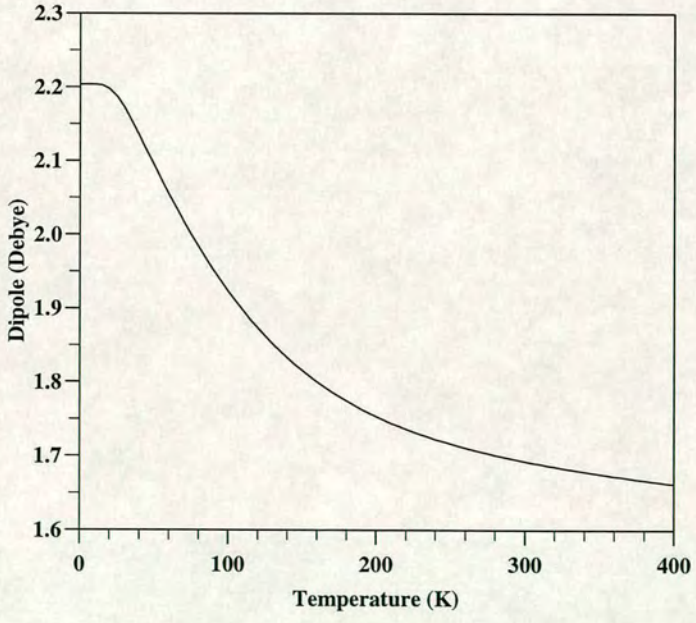

Figure 5.4. Plot of the temperature dependence of the molecular dipole of 2-2′ difluorobiphenyl as found from the Boltzmann-weighting scheme described in the text.

converge as discussed in Section 4.2.1. The two dipolar regions of the molecule located on the C-F bonds are responsible for the overall molecular dipole. Both components are directed from the C to the F atoms. The total molecular dipole is the vector sum of these two dipoles and hence is located at their centre. The dipole vector for the total molecular dipole is found to be predominantly in the y and z directions moving in a path which follows the relative positions of the fluorine atoms. That is, it points in a direction which lies at half of the torsional angle between the two phenyl rings. A diagram showing the direction and magnitude of the molecular dipole as a function of torsional angle is given in Figure 5.3.

The statistically averaged dipole can be found by multiplying the Boltzmann probability for each conformer (as shown in Figure 4.2 (inset)) and the corresponding dipole magnitude. The molecular dipole moment as a function of temperature can be easily calculated and is shown in Figure 5.4. It can be seen that the dipole of the molecule decreases with temperature from 2.21D to 1.66D at room temperature (300K). This can be understood by examining the probability distribution with respect to temperature (see Section 4.2.1). The local energy minimum conformation at 130^0 becomes increasingly occupied as temperature rises but since this conformation has a lower dipole moment, the total averaged dipole decreases.

5.1.3 5CB and related fragments

For 5CB it is generally recognised that the highly polar cyano group accounts for most of the polarity, along with the alkyl chain which is thought to increase the dipole through electron donation. To quantify the effect of these contributions, the dipole moments have been calculated for 4-cyanobiphenyl (0CB), 5CB and 4-pentyl biphenyl (5B) for various inter-ring bond torsional angles. The results are shown in Table 5.2.

It can be seen that there is a slight conformational dependence for all three molecules. In each case the dipole moment follows the same trend by decreasing by $\approx 7 - 8\%$ in going from $0°$ to $90°$. For 5CB there was also found to be a slight dependence on the

Molecule	Inter-ring bond torsional angle					
	0°	20°	37°	40°	60°	90°
0CB	5.92	5.87	5.83	5.77	5.61	5.47
5CB	6.70	6.61	6.50	6.48	6.38	6.08
5B	0.59	0.58	0.55	0.54	0.52	0.50

Table 5.2. Dipole moment magnitudes (in Debye) for the mesogenic fragments and 5CB as described in the text.

tail conformation, where the dipole ranged from 6.2 to 6.6 D. The Table shows that the largest contribution to the dipole moment of 5CB (in its minimum conformation at 36° with an all trans tail), comes from the cyano group since 0CB has a relatively large dipole of 5.83D. However, the effect of the electron donating tail is evident as the dipole moment of 5B is 0.55 D. The addition of these fragment dipoles is 6.38 D, which is marginally smaller than the dipole of 5CB (6.50D). The results suggest that intramolecular charge transfer is slight and implies that simple vector addition of dipole moments of fragments provides a reasonable estimate of the total molecular dipole.

5.2 Molecular quadrupoles

Recent evidence suggests quadrupolar interactions play an influential role in determining liquid crystalline properties, particularly of the smectic phase [32, 144, 150, 151]. Molecular dynamics simulations performed by Neal *et al.* [32, 150] have investigated the effect on the smectic phase from the steric asymmetry arising from molecular quadrupoles and also the inter-molecular interactions between longitudinal linear quadrupoles. In both cases the smectic phase showed substantial sensitivity to the quadrupolar effects. The steric quadrupoles [32] were found to induce a rippled structure through the smectic B phase. The linear quadrupoles [150] were found to destabilise the formation of the smectic phase, with the phase disappearing altogether at higher magnitudes of quadrupole. Also reported in [150] is the first simulation of a smectic C phase. This finding is in agreement with the theoretical studies of Barbero

and Durand [144] and Poniewierski and Sluckin [151], which both predict a smectic C phase using quadrupolar interactions. Barbero and Durand [144] report by means of a Landau expansion of free energy, that tilt of the director is an intrinsic property of a well ordered quadrupolar layered system. Poniewierski and Sluckin [151] have demonstrated that for a system of uniaxial perfectly aligned hard parallel cylinders, the smectic C phase is favoured by the electric quadrupole.

However, although computational simulations such as those described above provide valuable generic insight into the role of quadrupolar interactions, conclusions are not directly transferable to real liquid crystals since molecular charge densities are represented as only one or two point dipoles or quadrupoles, and often conformational degrees of freedom are neglected. Also despite the growing interest in the molecular quadrupoles of liquid crystals, there have been few attempts to determine their values for real mesogenic fragments and molecules. Quadrupole moments are hard to determine experimentally because they require a non-uniform field. They are often derived from measurements of field gradient induced birefringence [152] or the deflection of a molecular beam in a field gradient [148]. In this work the conformational dependence of the diagonalised quadrupole moments Q_{xx}, Q_{yy} and Q_{zz} and their influence on intermolecular interactions are determined for the non-polar molecule biphenyl [153].

5.2.1 The quadrupole tensor

Although electric quadrupole moments are encountered in numerous circumstances, they are not consistently defined and several variants may be noted in the literature [154]. In terms of multipole expansions it is the form proposed by Buckingham [155] that is most commonly used. Here the quadrupole tensor describes departures of the charge distribution from spherical symmetry [155]. The full form of the quadrupole tensor is given as:

$$\mathbf{Q} = \frac{1}{2}\begin{pmatrix} \sum q_i(3x_i^2 - r_i^2) & 3\sum q_i x_i y_i & 3\sum q_i x_i z_i \\ 3\sum q_i y_i x_i & \sum q_i(3y_i^2 - r_i^2) & 3\sum q_i y_i z_i \\ 3\sum q_i z_i x_i & 3\sum q_i z_i y_i & \sum q_i(3z_i^2 - r_i^2) \end{pmatrix} \tag{5.1}$$

where q_i is the electronic or ionic charge and x_i, y_i and z_i are Cartesian coordinates and r_i is the position relative to some origin. Since the core electrons are considered to be a superposition of spherical atomic charge densities and would therefore have no surrounding quadrupolar field, the electrostatic forces arise only from the valence charge distribution. This means that the pseudopotential approximation is sufficient for the calculation of the quadrupole tensor. Diagonalisation of the tensor yields the quadrupole moments and the corresponding principle axis frame:

$$\mathbf{Q} = \begin{pmatrix} Q_{xx} & 0 & 0 \\ 0 & Q_{yy} & 0 \\ 0 & 0 & Q_{zz} \end{pmatrix} \tag{5.2}$$

and since $\mathbf{Q}$ is traceless only two body-fixed components exist, Q_{xx} and Q_{yy} where $Q_{zz} = -(Q_{xx} + Q_{yy})$.

Before the method was used to calculate the quadrupole moments of biphenyl, it was first applied to four test molecules for which the quadrupole moments are known experimentally. These results and comparisons are shown in Table 5.3. For N_2 and benzene, comparison with the experimental value is good, with the difference being approximately 10%. For the other molecules there is a larger discrepancy between the observed and calculated values. The difference increases to a maximum of 15% for the Q_{zz} component of naphthalene.

Molecule	This work			Experimental	
	Q_{xx}	Q_{yy}	Q_{zz}	Q_{zz}	Ref.
N_2	2.69	2.69	-5.38	-4.92±0.09	[147]
benzene	12.33	12.28	-24.62	-28.3±1.2	[152]
hexafluorobenzene	-12.76	-12.74	25.50	31.7±2.3	[147]
naphthalene	18.39	19.50	-37.88	-45.0±0.4	[147]

Table 5.3. This Table shows the molecular quadrupole moments calculated from this work. Also shown are experimental values derived from measurements of the electric field gradient induced birefringence. All values are quoted in 10^{-40}Cm^2. For linear molecules the z axis is the symmetry axis. All quadrupoles are calculated using optimised structures, although structural optimisation had little effect on the values. The molecules are planar in the x-y plane and the long axis of naphthalene is parallel to the x axis.

5.2.2 Molecular quadrupole for biphenyl

Single molecule calculation

In this Section the diagonalised quadrupole moments Q_{xx}, Q_{yy} and Q_{zz} are calculated as a function of the torsional angle. The reference frame used for the calculations is shown in Figure 5.5 (a). The molecule is positioned such that its long molecular axis is directed along the z axis. The torsional angle θ, is the relative angle between the phenyl rings. A projection in the x-y plane is shown in Figure 5.5 (a) to illustrate θ more clearly. The movement arrows shown in the Figure indicate that in going from 0° to 180°, one phenyl ring rotates clockwise by 90° and the other anti-clockwise by 90°. This relative rotational movement of the two phenyl groups preserves the symmetry in the x-y plane and thereby ensures that the principal axes for the quadrupole moments Q_{xx}, Q_{yy} and Q_{zz} are coincident with the xyz frame for all torsional angles. Since the principal axes are coincident, direct comparison can be made between the three quadrupole moments Q_{xx}, Q_{yy} and Q_{zz} as a function of the torsional angle.

The magnitude of the quadrupolar moments Q_{xx}, Q_{yy} and Q_{zz} are shown in Figure 5.6. The results show that although one component Q_{zz}, remains constant the other two components Q_{xx} and Q_{yy}, change in a counter-acting sinusoidal fashion with 1-fold

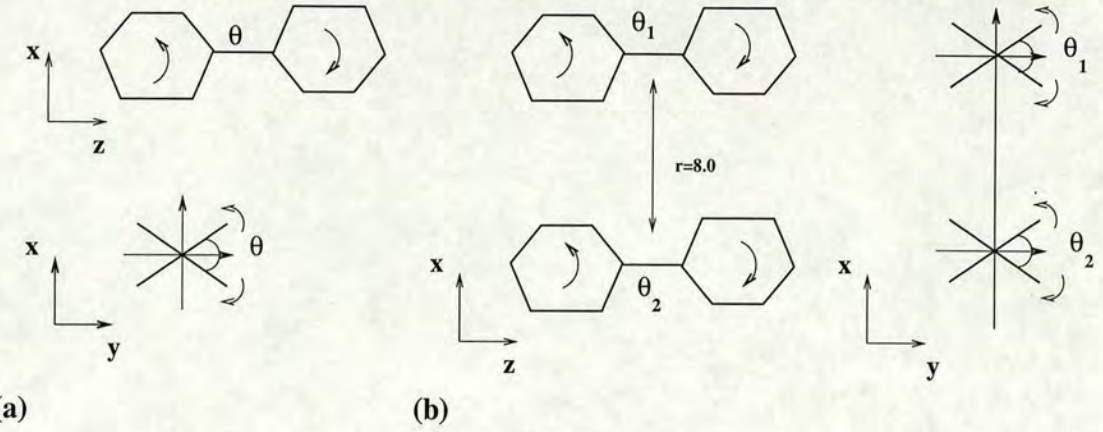

Figure 5.5. This Figure schematically shows the reference frame used to (a) calculate the quadrupole moments of a single molecule of biphenyl and (b) calculate the inter-molecular quadrupole-quadrupole potential. The phenyl rings are drawn as projections to indicate movement into or out of the plane. The movement arrows indicate that each phenyl ring is rotated $\theta/2$ out of the x-y plane. The point quadrupoles are located in the centre of the inter-ring C-C bonds.

symmetry around 360°. It can be seen that for the 0° and 180° conformers there has been an interchange of Q_{xx} and Q_{yy} which corresponds the the fact the molecule has gone from $\theta = 0°$, where it lies planar in the x-z plane, to $\theta = 180°$, where it lies planar in the y-z plane. The strong dependence of Q_{xx} and Q_{yy} on torsional angle was expected due to the significant redistribution of charge about the x and y axes. The slight variation in Q_{zz} is most likely due to subtle changes in bonding.

Quadrupole-quadrupole inter-molecular potential

In this Section the quadrupole-quadrupole potential is calculated for two biphenyl molecules aligned parallel as shown in Figure 5.5 (b), as a function of the torsional angles θ_1 and θ_2. In order to calculate the inter-molecular quadrupole-quadrupole potential, it is necessary to use a multipole expansion. There are a number of forms available to perform this expansion and usually it depends on the symmetries involved. The expansion due to Buckingham *et al.* [155] is the most commonly used since generally only linear quadrupoles are modelled. However for multipoles of lower symmetry, as in the case of biphenyl, the complete form of Price *et al.* [156] is necessary.

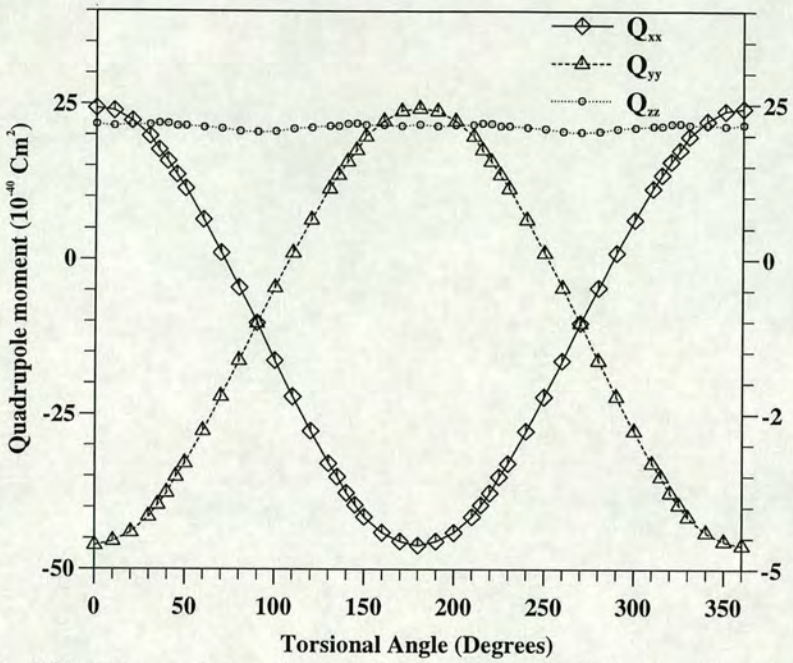

Figure 5.6. This Figure shows the varying magnitude of the quadrupole components Q_{xx}, Q_{yy} and Q_{zz} as a function of the torsional angle. The principal axes for each conformation are coincident with the xyz frame. Markers indicate the torsional angles for which the quadrupole tensor was calculated.

Using the same abbreviations as those of Price *et al.* [156], the quadrupole-quadrupole potential between the two molecules can be written as:

$$
\begin{aligned}
U &= (4\pi\epsilon_0)^{-1} r^{-9} \Bigg\{ \frac{3}{4} Q_{20}^{(1)} Q_{20}^{(2)} \Big\{ 35(\hat{\mathbf{z_1}}.\hat{\mathbf{r}})^2(\hat{\mathbf{z_2}}.\hat{\mathbf{r}})^2 - 5r^2\Big[(\hat{\mathbf{z_1}}.\hat{\mathbf{r}})^2 + (\hat{\mathbf{z_2}}.\hat{\mathbf{r}})^2\Big] \\
&- 20r^2(\hat{\mathbf{z_1}}.\hat{\mathbf{r}})(\hat{\mathbf{z_2}}.\hat{\mathbf{r}})(\hat{\mathbf{z_1}}.\hat{\mathbf{z_2}}) + 2r^4(\hat{\mathbf{z_1}}.\hat{\mathbf{z_2}})^2 + r^4 \Big\} \\
&+ (1+P_{12})\, Q_{20}^{(1)} Q_{22c}^{(2)} \frac{\sqrt{3}}{4} \Big\{ 5\Big[7(\hat{\mathbf{z_1}}.\mathbf{r})^2 - r^2\Big]\Big[(\hat{\mathbf{x_2}}.\mathbf{r})^2 - (\hat{\mathbf{y_2}}.\mathbf{r})^2\Big] \\
&- 20r^2\Big[(\hat{\mathbf{z_1}}.\mathbf{r})(\hat{\mathbf{x_2}}.\mathbf{r})(\hat{\mathbf{z_1}}.\hat{\mathbf{x_2}}) - (\hat{\mathbf{z_1}}.\mathbf{r})(\hat{\mathbf{y_2}}.\mathbf{r})(\hat{\mathbf{z_1}}.\hat{\mathbf{y_2}})\Big] + 2r^4\Big[(\hat{\mathbf{z_1}}.\hat{\mathbf{x_2}})^2 - (\hat{\mathbf{z_1}}.\hat{\mathbf{y_2}})^2\Big] \Big\} \\
&+ Q_{22c}^{(1)} Q_{22c}^{(2)} \frac{1}{4} \Big\{ 35\Big[(\hat{\mathbf{x_1}}.\mathbf{r})^2 - (\hat{\mathbf{y_1}}.\mathbf{r})^2\Big]\Big[(\hat{\mathbf{x_2}}.\mathbf{r})^2 - (\hat{\mathbf{y_2}}.\mathbf{r})^2\Big] \\
&- 20r^2\Big[(\hat{\mathbf{x_1}}.\mathbf{r})(\hat{\mathbf{x_2}}.\mathbf{r})(\hat{\mathbf{x_1}}.\hat{\mathbf{x_2}}) + (\hat{\mathbf{y_1}}.\mathbf{r})(\hat{\mathbf{y_2}}.\mathbf{r})(\hat{\mathbf{y_1}}.\hat{\mathbf{y_2}}) - (\hat{\mathbf{x_1}}.\mathbf{r})(\hat{\mathbf{y_2}}.\mathbf{r})(\hat{\mathbf{x_1}}.\hat{\mathbf{y_2}}) \\
&- (\hat{\mathbf{x_2}}.\mathbf{r})(\hat{\mathbf{y_1}}.\mathbf{r})(\hat{\mathbf{y_1}}.\hat{\mathbf{x_2}})\Big] + 2r^4\Big[(\hat{\mathbf{x_1}}.\hat{\mathbf{x_2}})^2 + (\hat{\mathbf{y_1}}.\hat{\mathbf{y_2}})^2 - (\hat{\mathbf{x_1}}.\hat{\mathbf{y_2}})^2 - (\hat{\mathbf{y_1}}.\hat{\mathbf{x_2}})^2\Big] \Big\} \Bigg\} \qquad (5.3)
\end{aligned}
$$

where $\hat{x_1}$, $\hat{y_1}$, $\hat{z_1}$, and $\hat{x_2}$, $\hat{y_2}$, $\hat{z_2}$ are the unit vectors describing the orientation of molecules 1 and 2 respectively and **r** is the vector from site 1 to site 2. The operator P_{12} exchanges the labels of the two molecules. The particular choice of reference frame used to perform the calculation, as described by Figure 5.5 (b), means many of the terms in Eqn. 5.3 are equal to zero. The parameters Q_{20} and Q_{22c} are expressed as:

$$Q_{20} = Q_{zz}$$
$$Q_{22c} = \sqrt{(1/3)}\,(Q_{xx} - Q_{yy}). \tag{5.4}$$

From Figure 5.6 it is clear that Q_{20} does not change and is approximately equal to $24.0\times10^{-40}\mathrm{Cm}^2$. The parameter Q_{22c} however does show a significant torsional angle dependence, and can be described by a simple sinusoidal curve; $Q_{22c}=40.487\cos(\frac{2\pi\theta}{360})$, where θ is replaced by either θ_1 and θ_2 accordingly. It can be seen that Q_{22c} is a measure of the biaxiality of the quadrupole moments.

Quadrupole-quadrupole potentials were calculated for intermolecular separations of 5.0Å and 8.0Å. The 2 dimensional contour plots shown in Figure 5.7 (a) and (b) show the potential as a function of the angles θ_1 and θ_2 from 0° to 360°. The inter-molecular separation of 5.0Å represents a close approach of two molecules, leaving only 1Å of vacuum between neighbouring phenyl rings. For the inter-molecular separation of 8.0Å, there is 4Å of vacuum and the quadrupole-quadrupole interaction is expected to be much weaker.

The potentials are very similar in appearance although the potential for the 5.0Å separation is much deeper. The plots can be described by three main features; a deep minimum which occurs at four symmetrically equivalent points of θ_1=0° and θ_2=180°, a small local maximum which again occurs at four symmetrically equivalent points of θ_1=0° and θ_2=0°, and one global maximum located in the centre at θ_1=180° and θ_2=180°. Figure 5.8 schematically shows these three configurations in the x-z and x-y planes. The terms broadside, T and axial are used to describe them and refer to the

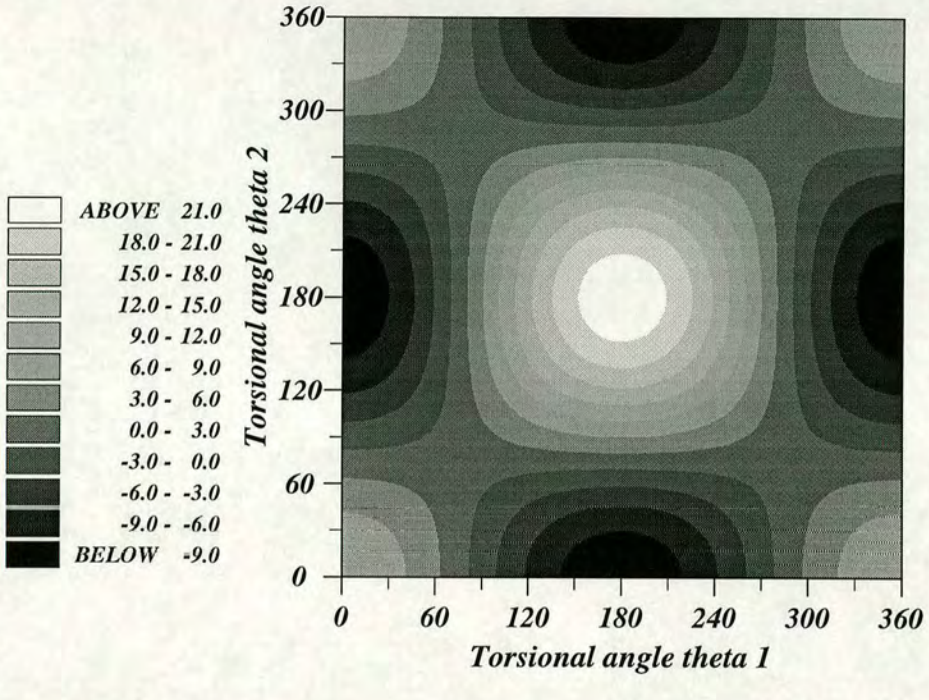

(a)

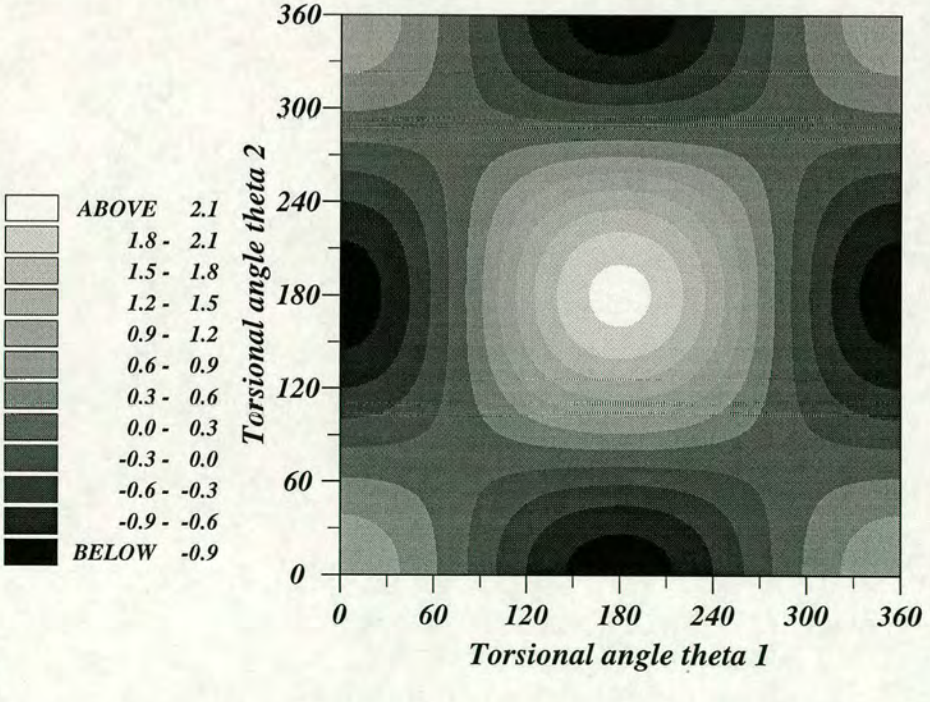

(b)

Figure 5.7. This Figure shows the inter-molecular quadrupole-quadrupole potential (in kJ/mol) as a function of θ_1 and θ_2 for separations of (a) $5\mathring{A}$ and (b) $8\mathring{A}$.

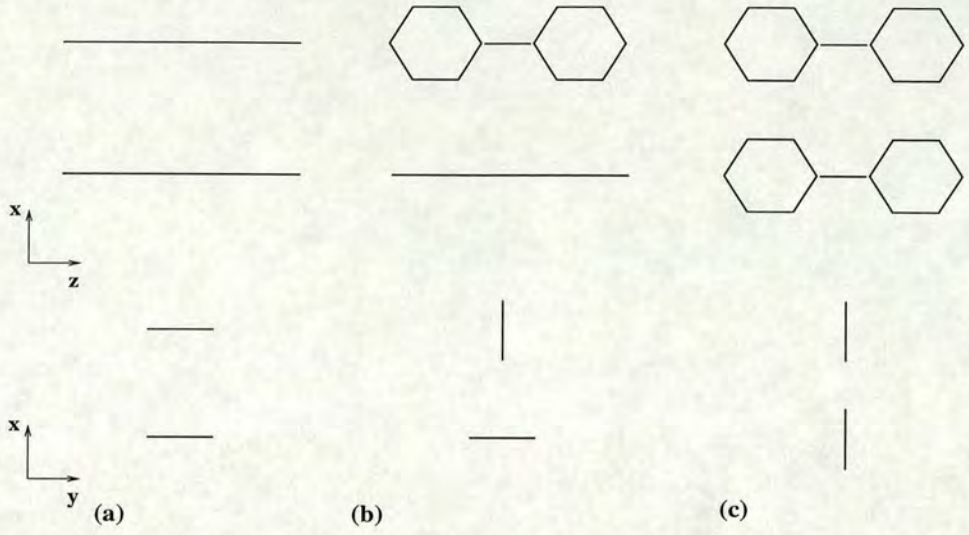

Figure 5.8. This Figure schematically illustrates the broadside, T and axial configurations as described in the text. Configuration (a) is the broadside configuration and occurs at symmetrically equivalent points of θ_1=0° and θ_2=0°, configuration (b) is the T configuration and occurs at symmetrically equivalent points of θ_1=0° and θ_2=180°, and configuration (c) is the axial configuration which occurs when θ_1=180° and θ_2=180°. The terms broadside, T and axial refer to the projection of the molecules in the x-y plane.

shape of their respective projections in the x-y plane. The contour plots show that the four attractive energy configurations correspond to a T configuration. The global maximum corresponds to an axial configuration and the four local maxima correspond to broadside configurations.

So far, only the quadrupole-quadrupole potential between two molecules has been considered. However, the configuration that the molecules adopt will also be significantly influenced by their torsional potentials which restricts rotation about the inter-ring C-C bonds. Therefore, in order to gain a more realistic insight into the effects of quadrupole-quadrupole potential on inter-molecular interactions, it is necessary to incorporate the torsional potential into the 2 dimensional contour plots. Using the parameterised potential for biphenyl from Section 4.5, the torsional potential as a function of θ_1 and θ_2 was superimposed onto the quadrupole-quadrupole potential. The resultant contour plots are shown Figure 5.9 (a) and (b) for the same separations as before.

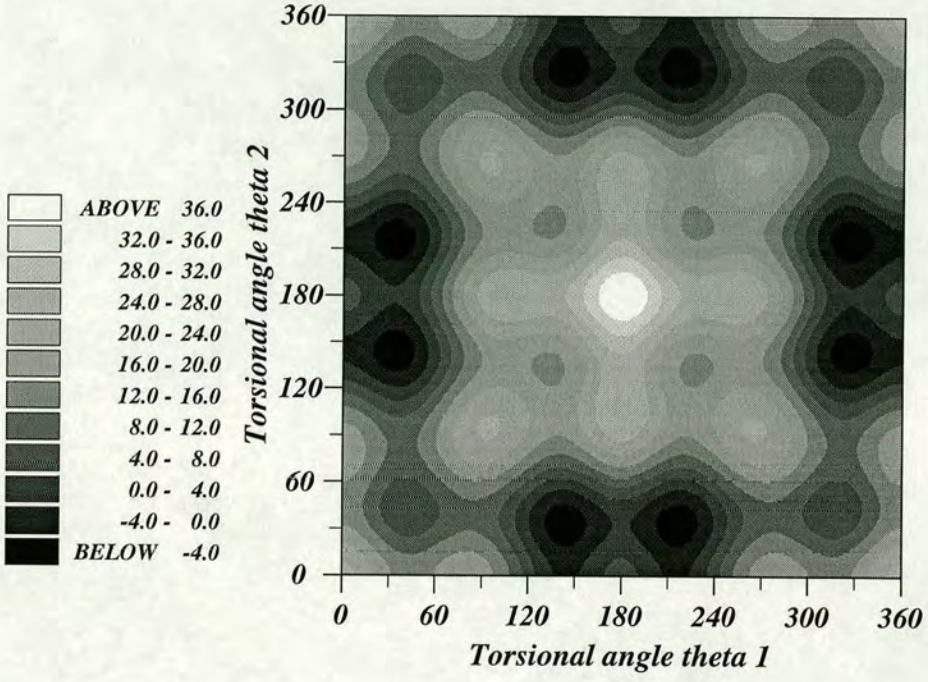

(a)

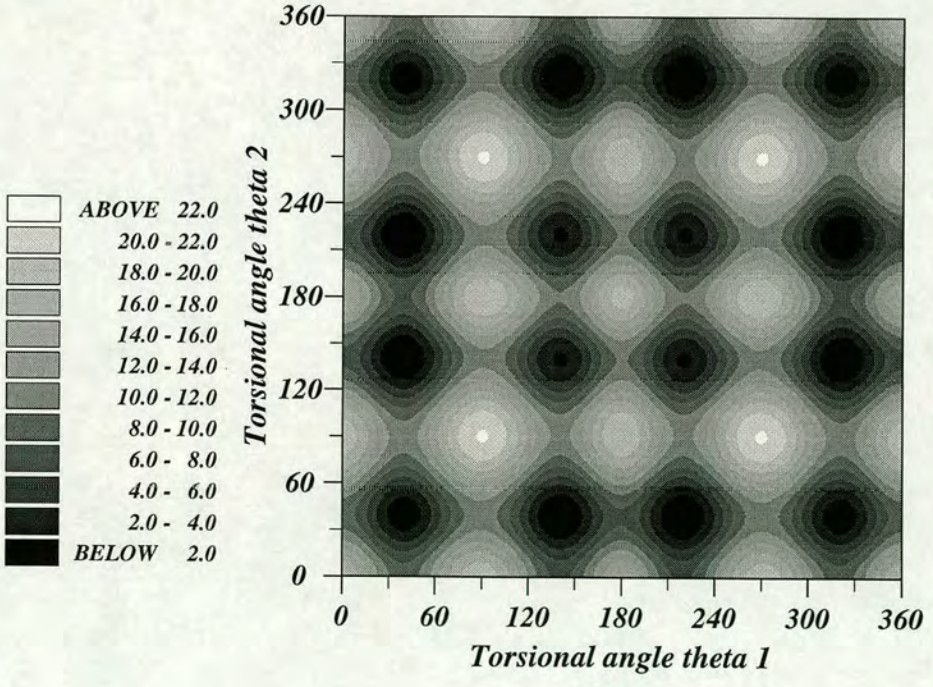

(b)

Figure 5.9. This Figure shows the superposition of the torsional and quadrupole-quadrupole potentials (in kJ/mol) as a function of θ_1 and θ_2 as described in the text for an inter-molecular separations of (a) $5\mathring{A}$ and (b) $8\mathring{A}$.

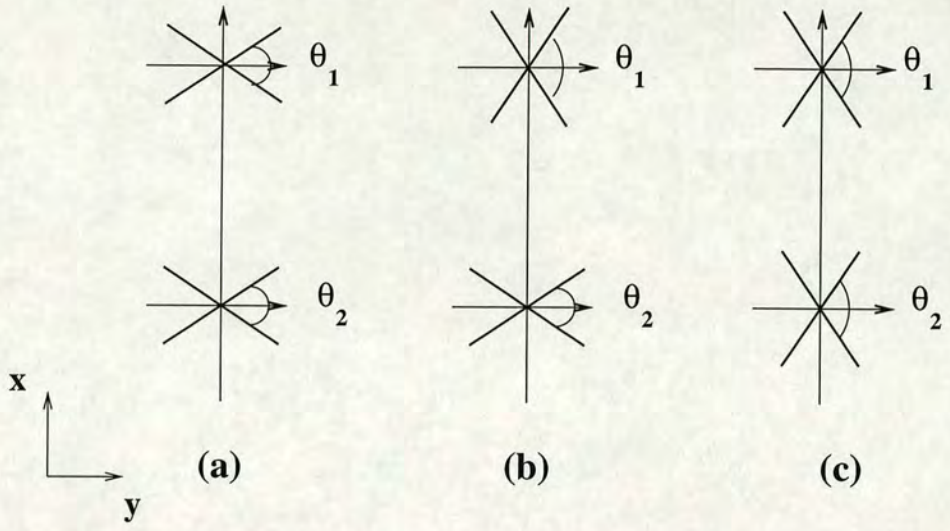

Figure 5.10. This Figure shows the three configurations of θ_1 and θ_2 which are stable at a separation of 8Å. Figure (a) is broadside, (b) T and (c) axial.

The inclusion of the torsional potential significantly effects the contour plots. For the separation of 8Å, it can be seen from Figure 5.9 (b) that the potential is dominated by 16 minima. The 16 minima all correspond to configurations where both molecules have a torsional angle which is some multiple of 44.0°, which is the equilibrium torsional angle for biphenyl [81]. Of the 16 minima, there are 3 which are distinct. These are shown schematically in Figure 5.10.

The four identical mimina located at the corners are symmetrically equivalent and correspond to the configuration shown in Figure 5.10 (a). The 8 symmetrically equivalent minima located on the edges of the plot correspond to the configuration shown in Figure 5.10 (b). The four in the centre region which are comparatively shallower than those on the outside, correspond to the configuration shown in Figure 5.10 (c). Figure 5.9 (b) indicates that at an inter-molecular separation of 8 Å, the energy differences between the 3 distinct configurations are small. The quadrupole-quadrupole interaction is too weak to have any significant influence. However, it can still be seen that its effect is to enhance the configuration shown in Figure 5.10 (b), which is most like the T configuration and likewise suppress the configurations shown in Figure 5.10 (a)

and (c), which are most like broadside and axial configurations respectively. For the shorter separation of 5Å, the influence of the quadrupole-quadrupole energy is much stronger and sufficient to completely change the structure of the potential. It can be seen from Figure 5.9 (a) that from the previous 16 minima, only 8 survive. As expected it is those which correspond to the T configuration once again. The other 8 minima are barely visible and dominated by a cross shaped potential barrier centred at θ_1 and θ_2 equal to 180.0°

5.3 Summary and conclusions

The electrostatic, induced dipole and dispersion (London) forces all contribute to the inter-molecular interactions in liquid crystals. A detailed knowledge of the molecular charge distributions and their conformation dependence is essential for an understanding of these interactions. The Chapter began by investigating the conformation dependence of molecular dipole moments. After testing the accuracy of the dipole calculations on a variety of small molecules and it was then applied to larger systems. It is found that the influence of the molecular shape (defined by the torsional angle) on the dipole moment depended on the location of the dipolar region within the molecule. For the molecule 2-2′ difluorobiphenyl discussed in Section 5.1.2 the temperature dependence of conformer populations was found to give rise to an associated temperature dependence of the molecular dipole. In this particular case a decrease was observed of approximately 25% in the temperature range 0K to 300K. In the case of 5CB (Section 5.1.3), it was demonstrated that the vector sum of the dipole moments due to the isolated fragments is representative of the total molecular dipole moment.

The second half of the Chapter investigated the conformation dependence of the quadrupole moments for biphenyl. Current simulation studies which employ explicit quadrupolar interactions between two molecules have generally expressed them as an expansion of linear quadrupoles along the long molecular axis. This work has shown

the significant effect that the conformational dependence of the quadrupole moments of biphenyl can have on intermolecular interactions. It was found that the Q_{xx} and Q_{yy} components had a strong dependence on the torsional angle, while Q_{zz}, which corresponds to the quadrupole component along the long axis of the molecule, remained unchanged. A parameter Q_{22c} which was a measure of the biaxiality of Q_{xx} and Q_{yy}, was parameterised. The quadrupole-quadrupole potential between the two molecules aligned side-by side was then calculated. It was found that the strength of the interaction was significantly dependent on intermolecular separation and certain configurations of θ_1 and θ_2 were selectively favoured and disfavoured. The lowest energy configuration was found to correspond to the molecules forming a T projection in the x-y plane, whereas the higher energy configurations corresponded to broadside and axial projections.

The quadrupole-quadrupole potential was then superimposed onto a torsional potential which described the restricted torsional movement of the biphenyl molecules. At a separation of 5Å the quadrupole-quadrupole interaction was found to have a significant effect on the structure of the potential, whereas at 8Å there was only slight appreciable change. For liquid crystals, where ordering is of unique importance, predispositions towards certain configurations in a subtle intermolecular environment may be highly influential. It is apparent that at short separations there is a significant quadrupole-quadrupole interaction which favours and disfavours certain configurations. This work marks a unique step towards gaining a deeper understanding of the quadrupole properties of liquid crystal molecules.

As a suggestion for further work, it would be of use to determine the inter-molecular potential for two biphenyl molecules from first principles. Although significant computational resources would be required, it would enable the loss of accuracy incurred as a result of truncating the multipole expansions to be investigated. It would also enable an investigation into the the accuracy of distributed multipole analysis (DMA) [157] method, where the electrostatic forces are represented using sets of atomic multipoles

distributed over the molecule. In fact the wavefunctions generated by CETEP could in principle be used to parameterise a DMA and provide valuable information about how the electron density of differing functional groups varies with conformation. In analogy to Chapter 4 where the transferability of torsional potentials was investigated, the transferability of DMAs could also be investigated. A fuller discussion of the DMA models and their parameterisation can be found in [157]. The plane wave basis set does not, however, offer a natural way of specifying quantities such as atomic charge, orbital populations and charge transfer which would be necessary to parameterise a DMA. The plane wave states require to be projected onto a localised basis set. This has recently been achieved using a technique described by Sanchez-Portal *et al.* [158] and has recently been used to perform a population analysis of bulk materials [159].

Chapter 6

Conformational Properties In The Nematic Phase

The coupling of molecular degrees of freedom to orientational order is a complex problem and central to understanding structure-property relationships in liquid crystals. In order to gain a deeper understanding, accurate data is required on single molecule properties such as conformational energies and their dependence on molecular environment. Two approaches to obtaining this data are possible: large scale atomistic simulations of the bulk phase [33, 34, 35, 36] or single molecule investigations [160] with inter-molecular effects handled by a mean field approximation. Large scale atomistic simulations offer the most realistic treatment of the inter-molecular effects. Here fluctuating short range interactions between molecules can be easily modelled. However, the accuracy of such studies in predicting conformational distributions is strongly determined by the quality of the force field. The single molecule approach has the advantage that it can benefit from a more accurate method to describe the intra-molecular interactions, although it is necessary to use the a mean field model to approximate the inter-molecular orientational potential.

Different approaches are possible in the description of the mean field. There are

models (as described in Section 1.1.1) which start from realistic expressions of the inter-molecular pair potential and derive the mean field by averaging over both the relative orientation of the coupled particles and their inter-molecular vector. There are also empirical mean field models, such as those developed by Ferrarini *et al.* [16] and Zimmerman *et al.* [137]. These models are based upon different hypotheses for the anisotropy of the molecular interactions. The model of Ferrarini *et al.* [16] uses an analogy with surface anchoring forces to derive the mean field potential, whilst the model of Zimmerman *et al.* [137] considers elastic distortions of the liquid crystal. In essence, both models provide phenomenological descriptions of the mean field potential experienced by the molecule. In both cases, the anisotropy of the mean field is derived from the anisotropy of the molecular shape.

The mean field model used in this work is that of Ferrarini *et al.* [16]; the surface tensor model. The model defines an anisotropic orientational potential which is constructed from details of the size and shape of the molecule and controlled by one temperature dependent adjustable parameter that is a property of the nematic medium. The model assumes that the molecular surface is split up into infinitesimally small surface elements, dS, and that each element contributes to an overall potential by an amount which depends on its orientation relative to the mesophase director. The surface tensor model can generally predict order parameters of rigid and flexible solutes to within 10% [16, 161, 162]. Although still a phenomenological description of the short range interactions, the model has been extended to predict the variation in transitional properties along a series of liquid crystal dimers [163] and even the induced twisting power of chiral dopants in nematic solvents [164].

However, one drawback of empirical models such as the surface tensor model, is that longer range interactions are not accounted for. As discussed in the previous Chapter, interactions between quadrupole and dipole moments have been shown to influence liquid crystal properties. There have also been a number of investigations into the ordering mechanisms of solute-solvent mixtures, which suggest that interactions

involving the permanent electric dipole and quadrupole moments of the solute molecules interacting with the average electric field (EF) and the average electric field gradient (EFG) of the solvent, respectively, are partly responsible for the solute orientational ordering [165, 166]. These fields originate from the charge distributions of the solvent molecules and their arrangement around the solute. Therefore, in order to eliminate any possible electrostatic contributions to orientational ordering, liquid crystal mixtures have been developed which have zero average EFs and EFGs [167]. These mixtures are ideal for studying short range anisotropic interactions and consequently many of the best comparisons between empirical models and experiment have been achieved using them.

This Chapter investigates the influence of the nematic environment, described in terms of the surface tensor model, on the conformational properties of the tail in 5CB [168]. So far all previous implementations of the model have used simple computational algorithms for generating molecular surfaces, the rotational isomeric state approximation for conformational distributions and molecular structures constructed from commonly accepted values of bond lengths and angles. In this work the gas phase conformational energies, molecular structures and surfaces are all determined from first principles. The Chapter is organised as follows. In the next Section details pertaining to the surface tensor model and the procedure to generate a molecular surface are summarised. Test calculations are performed on a number of molecular systems. The final Section of the Chapter investigates the conformational properties of the alkyl tail in 5CB. Order parameters for C-H bonds are calculated and compared to those determined by NMR and those predicted by theoretical investigations. The Fortran routines used in the calculations of the surface tensor model were provided by Dr. Alberta Ferrarini of Padova University, Italy.

6.1 The surface tensor model

The surface tensor model [16] derives the orientational potential from details of the molecular surface. The model assumes that the molecular surface is split up into infinitesimally small surface elements dS, and that each element tends to align parallel with respect to the mesophase director, $\hat{\mathbf{n}}$. The potential is expressed as:

$$U_{\mathrm{or}}(\beta,\gamma) = k_B T\,\epsilon \int_S P_2(\hat{\mathbf{n}}\cdot\mathbf{s})\; dS \tag{6.1}$$

where the integral is defined over the whole surface of the molecule and $\mathbf{s}$ is a unit vector normal to the surface area element dS. The spherical polar angles (β,γ) define the orientation of mesophase director in the molecular frame. P_2 is the second Legendre polynomial and ϵ is a parameter governing the strength of the ordering potential [16]. In thermotropic nematics, ϵ is positive so that each vector $\mathbf{s}$ will tend to align perpendicular to $\hat{\mathbf{n}}$. The value of ϵ is strongly temperature dependent and increases as the temperature is lowered. A self-consistency expression can be derived for ϵ [163]; under the simplifying assumption that the nematic is made of rigid uniaxial molecules this can be written as:

$$\epsilon = \gamma^2 T_s^{2,0} S_{zz}^s / k_B T, \tag{6.2}$$

where γ is a proportionality constant, $\mathrm{T}_s^{2,0}$ is the non-zero irreducible spherical component of the surface tensor for the mesogenic molecules and S_{zz}^s the corresponding order parameter at the temperature T, which is a function of ϵ.

The explicit dependence of $U_{\mathrm{or}}(\beta,\gamma)$ on the molecular orientation of a molecule can be derived using the addition theorem for spherical harmonics [169]:

$$P_2(\hat{\mathbf{n}} \cdot \mathbf{s}) = \sum_m C^*_{2m}(\theta, \phi)\, C_{2m}(\beta, \gamma), \tag{6.3}$$

where the C_{2m} are modified spherical harmonics. The angles (θ, ϕ) relate to the orientation of the unit vector $\mathbf{s}$ in the molecular frame. A second rank tensor, the surface tensor $T^{2,m}$ [16], whose irreducible spherical components depend on the orientational distribution of the surface elements can be introduced:

$$T^{2,m} = -\int_S dS\, C^*_{2m}(\theta, \phi). \tag{6.4}$$

This allows Eqn. 6.1 to be rewritten as:

$$U_{\mathrm{or}}(\beta, \gamma) = -k_B T\, \epsilon \sum_m T^{(2,m)*}\, C_{2,m}(\beta, \gamma). \tag{6.5}$$

The surface model allows for the calculation of orientational order parameters. The second rank orientational order parameters $\overline{C_{2m}}$ are defined as

$$\overline{C_{2m}} = Z^{-1} \int_0^{\pi} \sin(\beta)\, d\beta \int_0^{2\pi} d\gamma\, C_{2m}(\beta, \gamma)\, \exp[-U_{\mathrm{or}}(\beta, \gamma)\,/\,k_B T], \tag{6.6}$$

where

$$Z = \int_0^{\pi} \sin(\beta)\, d\beta \int_0^{2\pi} d\gamma\, \exp[-U_{\mathrm{or}}(\beta, \gamma)\,/\,k_B T]. \tag{6.7}$$

In the case of flexible molecules the orienting potential produces a coupling between orientational and torsional degrees of freedom. Following Emsley, Luckhurst and Stockley [170], the total potential of the nth conformer in a nematic field can be approximated

as:

$$U_n(\beta,\gamma) = U^n_{\rm conf} + U^n_{\rm or}(\beta,\gamma) \tag{6.8}$$

where the terms $U^n_{\rm or}$ and U^n_{conf} are the orienting and conformational contributions, respectively. The orienting term, $U^n_{\rm or}(\beta,\gamma)$, depends on the conformation of the molecule, because the molecular shape is different for the various conformers. The conformational term, U^n_{conf}, is independent of the molecular orientation. Therefore, the averaged molecular order parameters can be evaluated by summing over the n conformations,

$$\overline{C_{2m}} = \sum_n [\overline{C_{2m}}]_n \, p_n, \tag{6.9}$$

where p_n is the statistical weight of the nth conformer and given by,

$$p_n = \frac{Z_n}{\sum_n Z_n}, \tag{6.10}$$

where Z_n is the orientational partition function for the nth conformer, defined by an expression analogous to Eqn. 7. The Saupe ordering matrix can be derived from these order parameters [2], as well as the segmental order parameters $S^k_{CD}(n)$ for a conformer. The latter are calculated as:

$$S^k_{CD}(n) = \sum_m C^*_{2m}(\beta_k,\gamma_k)[\overline{C_{2m}}]_n \tag{6.11}$$

where β_k and γ_k are the spherical polar angles giving the orientation of the kth carbon deuteron (C-D) bond vector in the molecular frame.

The S_{CD} order parameters which can be determined, for example, from NMR spectra, are averages over all possible conformations adopted by the molecule and are

expressed as as:

$$S_{CD} = \sum_n p_n S_{CD}(n). \tag{6.12}$$

6.2 The molecular surface

In the original implementation of the surface model [16], the molecular surface is defined as the outer contour of the assembly of overlapping van der Waals spheres centred at the atomic positions. However, the discontinuities appearing at the intersections between spheres appear unrealistic and a more appropriate representation of the surface exposed to the solvent should be characterized by smoother contours. In the case of planar rigid molecules a better definition of the surface was obtained by considering a series of ribbons connecting the outer contours of sections of the vdW spheres on planes parallel to the horizontal symmetry plane [161].

Further to this work, the surface has recently been defined according to the rolling sphere algorithm [171], which maps the contact surface generated by a sphere of radius R rolling on a van der Waals surface. In this way a smoothed molecular surface is produced, by eliminating the details characterised by a length scale much shorter than R (in the limit $R \to \infty$ the ribbon model is recovered by the rolling sphere algorithm). It has been argued that the radius R can be interpreted as a parameter which measures the capability of solvent molecules to probe the cavities of the solute surface [172]. Use of the rolling sphere representation of the surface has been shown to improve the agreement between measured and calculated orientational order parameters [172].

6.2.1 The molecular surface from first principles

In this work the molecular surfaces are constructed from the electron distribution. Once the electronic wavefunctions have been calculated, the problem of converting information on the electron distribution into a smooth continuous molecular surface is

straightforward. The Marching Cubes algorithm as developed by Lorensen and Cline [173], can efficiently extract an isosurface (surface generated by many thousand of triangles) from any density distribution which is stored on a regular 3D grid.

The Marching Cubes algorithm [173] defines an isosurface by processing each cell on the 3D grid one at a time. A cell is made up of eight grid points and each point can be in two states, inside or outside the molecular surface, which is decided by whether the density at that point is greater than or less than a set cutoff parameter. The algorithm also determines how the isosurface intersects the cell of which there are 2^8 (256) different ways, however most of them are topologically equivalent either by rotation and/or by switching the states of the points. Lorensen and Cline [173], after some consideration of these equivalent arrangements, reduced the problem to 14 unique cases. A lookup table was then constructed for all 256 possible arrangements using simple permutations of these 14 cases. Two cases are trivial; one where all the points are outside the surface and the other when they are all inside. If however the cell has one or more vertices with values less than the chosen cutoff, and one or more vertices with values greater than the cutoff, then the cell contributes in some way to the surface.

The arrangement of the isosurface within the cell is determined from the vertices which are outside the surface. The algorithm uses an indexing convention to decide which of the 256 permutations a particular arrangement replicates and a lookup table is used to indicate which edges the isosurface intersects. The indexing convention numbers the vertices of the cell 0 to 7, and the edges 0 to 11. By labelling the vertices in this manner a reference can be given to the arrangement of the isosurface by summing the *bits* (ie 2 to the power n) from the labels of the vertices outside the surface. This number, which will be somewhere between 0 and 255, can be used as a reference with respect to the lookup table. After some linear interpolation to locate where the intersection points lie along the edges, triangles are placed accordingly and a surface created by connecting them all together. The algorithm ensures that adjacent triangles from adjacent cubes will share the same vertices and hence produce a continuous surface.

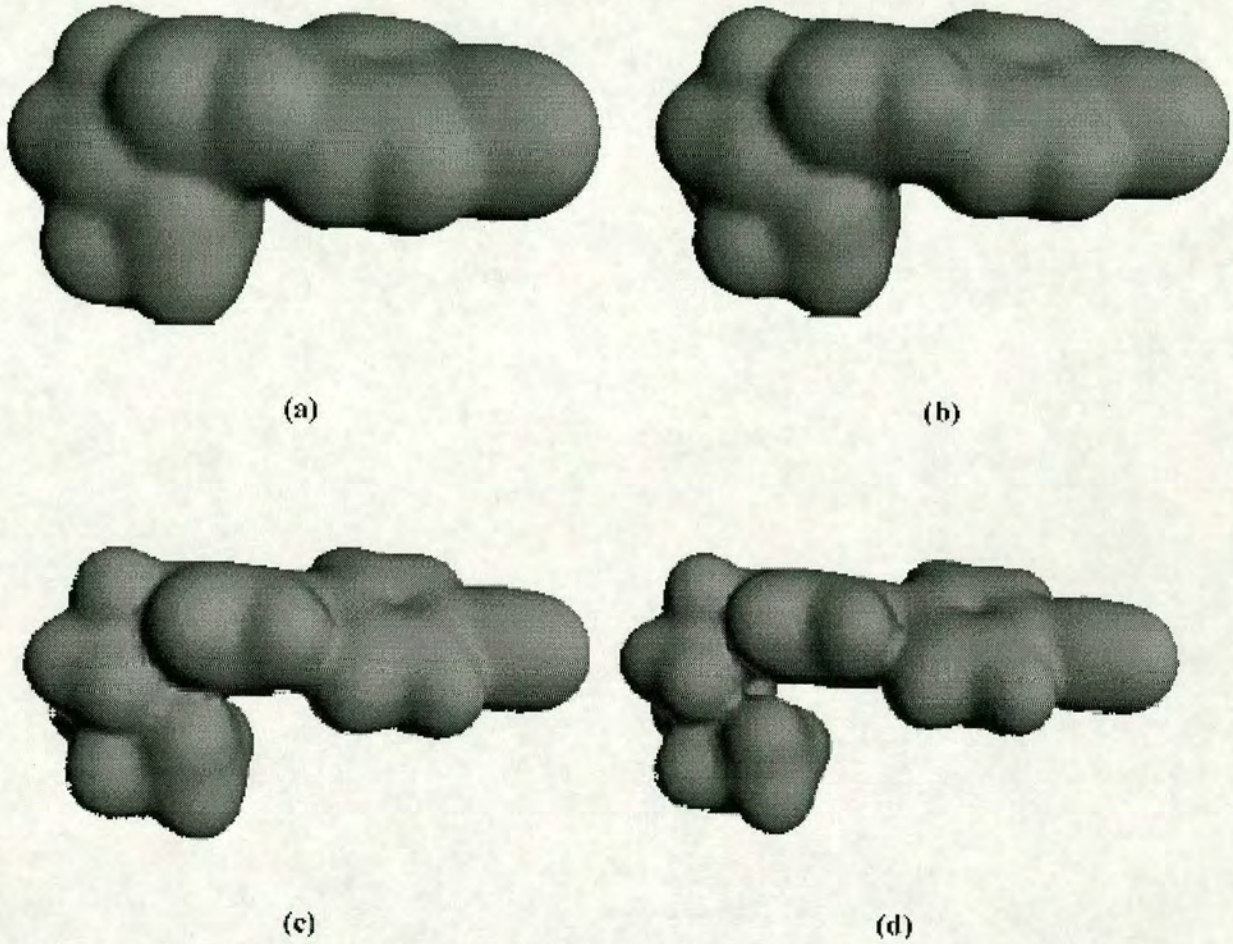

Figure 6.1. Molecular surfaces for 5CB (in a gtt conformation as described in Section 6.3), drawn to the same scale using different values of the isosurface cutoff parameter (in units of $e\mathring{A}^{-3}$); (a) 1.0, (b) 10.0, (c) 50.0 and (d) 100.0. The surfaces were visualised using the AVS/Express [174] software. It can be seen that the surfaces corresponding to lower cutoff values are more extended and smoother, with the holes in the phenyl rings less pronounced.

Cutoff ($e\mathring{A}^{-3}$)	Surface area ($\mathring{A}^2$)	% of charge
1.0	375.3	99.9
2.0	370.3	99.7
5.0	341.0	99.4
10.0	308.6	98.8
100.0	258.0	96.7

Table 6.1. Surface areas and the percentage of electron charge included within isosurfaces derived for a series of cutoffs.

The area of each triangular surface element is taken as half the length of the vector normal, calculated as the cross product of two vectors which define the triangles edges. The direction cosines of the vector normals are chosen so as they are pointing outward from the molecular surface by calculating the electron density gradient at each point. It is these surface element areas and vector normals which are then inputted into the surface model.

As the isosurface cutoff parameter defines the boundary between points in and out of the volume excluded by the surface, its value relates to the percentage of electron density included. Figure 6.1 illustrates this by showing the molecular surface with respect to the cutoff value, where it can be seen that the lower the chosen value, the smoother and more extended the surface becomes. The differences between these cutoffs become more apparent by examining the total area of surface and percentage of electron charge included. These parameters are shown in Table 6.1.

6.2.2 The optimal choice of surface

The Marching Cubes algorithm generates a molecule surface which is a contour of the electron density determined by a cutoff parameter. The influence of this parameter on the performance of the molecular surface must be investigated and its optimal value chosen on the basis of comparison between the experimental and predicted order parameters. In order to achieve these objectives, the biaxiality $< D^2_{02} >= (S_{xx} - S_{yy})/\sqrt{6}$

as a function of the order parameter $< D^2_{00} >= S_{zz}$ (where D^L_{mn} are the Wigner functions [169]), was calculated for two solutes ortho-dichlorobenzene (ODCB) and meta-dichlorobenzene (MDCB). The temperature dependence of the orientational ordering for these two solutes has been determined using NMR, where they were dissolved in zero average EFG liquid crystal mixtures [139].

Unlike rod shaped molecules, which will preferentially orient themselves such that the long molecular axis is parallel to the director, disc like molecules such as ODCB and MDCB preferentially orient such that the plane of the molecule is parallel to the director. This gives rise to negative order parameters for the z-axis which is perpendicular to the molecular plane. Figures 6.2 (a) and (b) plot the predicted order parameters $< D^2_{02} >$ against $< D^2_{00} >$ for ODCB and MDCB respectively. Four different values of cutoff are used to generate molecular surfaces; 1.0, 2.0, 5.0 and 10.0 e$\mathring{A}^{-3}$. Each point on the curves in Figures 6.2 (a) and (b) corresponds to a unique value of the solvent ordering strength ϵ.

Also shown in Figures 6.2 (a) and (b) are results taken from recent calculations [172] based on molecular surfaces generated with the rolling sphere algorithm, with a rolling sphere radius equal to 3Å. The significant spread of the results for first principles surfaces indicates a strong sensitivity to the cutoff parameter. By lowering the cutoff value, the curves converge towards limiting values, thereby progressively improving the comparison with experimental data. Cutoff values lower than 1.0 were not used since they were found on occasion not to generate fully closed molecular surfaces. For both molecules, the rolling sphere results lie in between the first principles 1.0 and 2.0 curves.

As a further investigation of first principles surfaces and the surface tensor model, the order parameters for benzene, fluorobenzene and naphthalene were determined and compared with experimental values measured in a zero average EFG mixture at a temperature of 300K [161]. The first principles molecular surfaces were characterised using a cutoff parameter of 1.0e$\mathring{A}^{-3}$ and the reference frames are the same as those used in Ref. [161]. The value of the orienting strength parameter ϵ=0.023$\mathring{A}^{-2}$, was

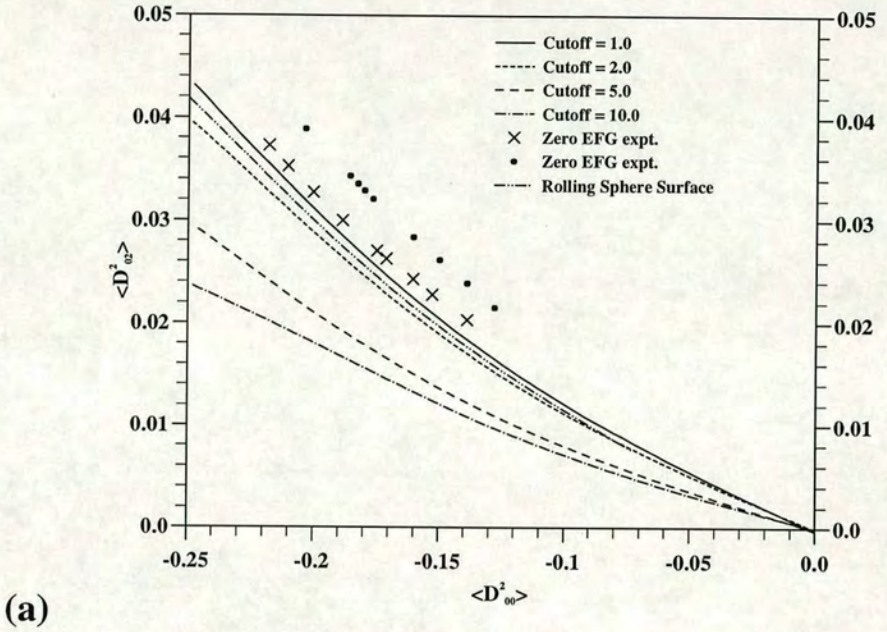

(a)

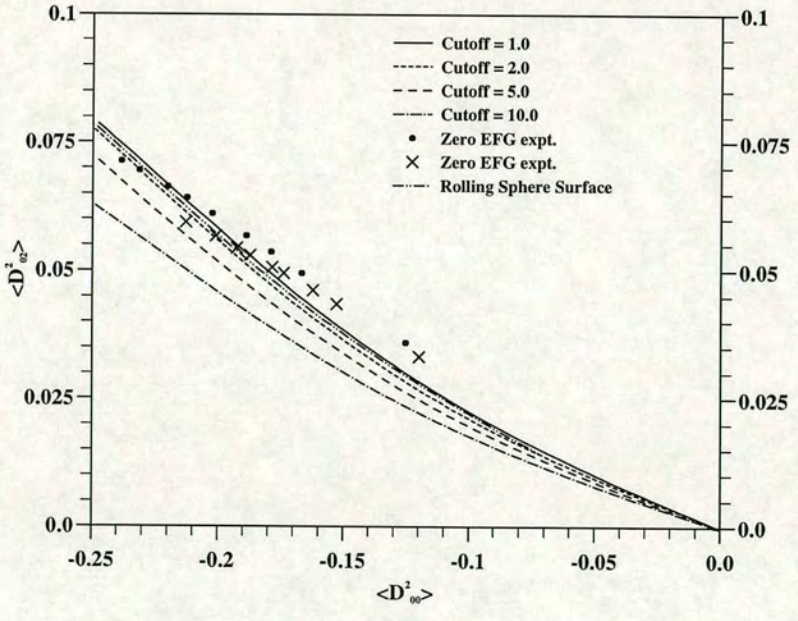

(b)

Figure 6.2. The biaxial order parameter $< D^2_{02} >$ as a function of $< D^2_{00} >$ for (a) dichlorobenzene (ODCB) and (b) meta-dichlorobenzene(MDCB). Two sets of experimental data which were taken from Tables reported in Ref. [139] are also shown where the order parameters of ODCB and MDCB were measured in zero EFG mixtures at different temperatures. Cutoff values are in e$\mathring{A}^{-3}$.

		Exp. [161]	This work	[161]*
Benzene	S_{zz}	-0.134	-0.133	-0.150
F-benzene	S_{zz}	0.117	0.104	0.109
	$S_{xx} - S_{yy}$	0.196	0.214	0.218
Napthalene	S_{zz}	0.273	0.185	0.214
	$S_{xx} - S_{yy}$	0.233	0.241	0.275

* Surface tensor model with ribbon surfaces and an $\epsilon = 0.034\mathring{A}^{-2}$.

Table 6.2. Experimental and calculated order parameters for the molecules benzene, F-benzene and naphthalene dissolved in the zero EFG nematic mixture 55wt% ZLI1132 + EBBA. The value of ϵ used in this work was $0.023\mathring{A}^{-2}$. Reference frames used are the same as those used in Ref. [161]. F-benzene and Napthalene are lying in the xz plane, while benzene lying in the xy plane. The long axis of Napthalene is along the z axis.

chosen so as to give the best agreement with the experimental order parameters. The results are shown in Table 6.2, together with those reported in Ref. [161], which were obtained with surfaces generated using the ribbon algorithm. It should be noted that the different surface definitions used makes a comparison of ϵ values meaningless. Some differences are observed between the two sets of calculations, with the present calculations showing a better agreement with experiment in the case of benzene, and the opposite for naphthalene.

6.3 Bond order parameters of 5CB

In this section the order parameters (S_{CD}) for C-D bonds in the chain and phenyl rings are determined. Optimised geometries, gas phase energies and molecular surfaces for each of the 27 conformations of 5CB (see Section 4.4) were implemented into the surface tensor model to calculate the probability distributions and corresponding S_{CD} order parameters (calculated according to Eqn. 6.12) for different values of mean field strength. Molecular surfaces were generated using a cutoff of 1.0 e$\mathring{A}^{-3}$.

Table 6.3 shows the calculated S_{CD} order parameters for the ring and tail C-D bonds from this work and deuterium NMR investigations by Emsley *et al.* [175], who

ϵ ($\AA^{-2}$)	Order parameter					
	ring[a]	1	2	3	4	5
0.015	-0.055	-0.138	-0.095	-0.094	-0.067	-0.053
0.018	-0.063	-0.165	-0.119	-0.118	-0.087	-0.068
0.020	-0.067	-0.179	-0.132	-0.131	-0.097	-0.077
0.022	-0.070	-0.191	-0.142	-0.142	-0.104	-0.082
0.025	-0.079	-0.215	-0.170	-0.168	-0.134	-0.107
NMR Expt. [175][b]	-0.044	-0.202	-0.137	-0.147	-0.099	-0.072

[a] Ring order parameter represents the average of the eight S_{CD} C-D bond order parameters for the two phenyl groups.
[b] 5CB NMR order parameters measured at 300K. Values of 168 and 185 kHz as used for the quadrupolar coupling constant for the alkyl chain and aromatic ring deuterons, respectively.

Table 6.3. Experimental and calculated S_{CD} order parameters for the 5CB molecule using different mean field strengths. The temperature used to determine the Boltzmann probabilities was set at 300K.

Method	S_{CD} order parameters					
	ring[a]	1	2	3	4	5
This work[b]	-0.068	-0.186	-0.138	-0.137	-0.100	-0.079
Surface Model [16][c]	-0.042	-0.207	-0.120	-0.131	-0.085	-0.081
Monte Carlo [160][d]	-0.078	-0.223	-0.125	-0.127	-0.083	-0.057
Molecular dynamics [34][e]	-	-0.185	-0.120	-0.150	-0.100	-0.060
NMR Expt. [175]	-0.044	-0.202	-0.137	-0.147	-0.099	-0.072

[a] Ring order parameter represents the average of the eight S_{CD} C-D bond order parameters for the two phenyl groups.
[b] For a mean field strength of ϵ=0.022$\AA^{-2}$.
[c] The RIS approximation and vdW surfaces were used.
[d] Single molecule Monte Carlo simulation done using molecular mechanics and a mean field. Mean Field Strength = 0.875 kJ/mol$^{-1}\AA^{-1}$.
[e] Full atomic Molecular dynamics of 75 molecules using an OPLS (optimised potentials for liquid simulations) force field.

Table 6.4. Comparison of the S_{CD} order parameters as calculated from this work, the surface tensor model and vdW surfaces, single molecule Monte Carlo, molecular dynamics simulations and NMR experiment.

determined the quadrupolar couplings for the C-D bonds at 300K. The Table shows that although all the order parameters increase in line with the mean field strength, the order parameters of the carbon atoms further down the tail increase proportionally more. An ϵ value of $0.022\mathring{A}^{-2}$ gives the best overall comparison with the NMR data. Table 6.4 shows for comparison the predicted S_{CD} order parameters from other methods. The differences between the various results depend upon the different conformer structures, gas-phase energies, and the different ways to take into account the effects of the nematic environment. In order to better analyse these contributions, the conformational distributions and their dependence on the mean field strength will be detailed in the next Section.

6.4 The conformational distributions of 5CB

The Boltzmann populations are shown in Table 6.5 for the various strengths of mean field used. The populations indicate that for all the values of ϵ, the conformer populations show no significant dependence on the orientation (+ or −) of the *gauche* torsion (it should be noted that for symmetry reasons this difference would vanish for an interring torsional angle of 90°). It is also apparent that the four tail conformations with at most a single *gauche* state dominate all the distributions; ttt, gtt, tgt and ttg. In terms of a percentage of the total distribution these conformers account for 77% in the gas phase, increasing to 85% for an $\epsilon = 0.025\mathring{A}^{-2}$.

The influence of the mean field is most clearly understood by examining the relative trends for these four conformers only. The most populated state for all strengths of mean field is the ttt conformer, with a population of 25% in the gas phase, increasing to 34% for $\epsilon = 0.025\mathring{A}^{-2}$. The tgt population (combined tg+t and tg−t) also undergoes some significant changes in size, doubling from 15% in the gas phase to 30% for $\epsilon = 0.025\mathring{A}^{-2}$. This occurs in conjunction with a significant reduction in the population of the gtt conformers, which decrease from 22% in the gas phase to 10% for $\epsilon = 0.025\mathring{A}^{-2}$.

conf.	0.000	0.015	0.018	0.020	0.022	0.025
g−g−g−	0.87	0.62	0.54	0.49	0.47	0.38
g−g−t	3.23	2.28	1.97	1.78	1.69	1.38
g−g−g+	0.01	0.01	0.01	0.01	0.01	0.01
g−tg−	2.20	1.64	1.44	1.31	1.25	1.02
g−tt	10.94	8.16	7.20	6.58	6.30	5.19
g−tg+	2.58	2.24	2.09	2.00	2.00	1.77
g−g+g−	0.03	0.02	0.02	0.02	0.02	0.01
g−g+t	0.15	0.11	0.10	0.09	0.08	0.07
g−g+g+	0.07	0.05	0.05	0.04	0.04	0.04
tg−g−	2.26	2.20	2.15	2.10	2.10	1.98
tg−t	7.93	11.10	12.29	13.08	13.47	15.09
tg−g+	0.12	0.13	0.12	0.12	0.13	0.12
ttg−	7.50	7.07	6.83	6.66	6.49	6.08
ttt	24.64	29.27	30.80	31.82	32.26	34.01
ttg+	7.57	7.01	6.77	6.60	6.44	5.93
tg+g−	0.13	0.14	0.14	0.14	0.15	0.14
tg+t	7.86	11.00	12.18	12.92	13.29	15.03
tg+g+	2.81	2.76	2.70	2.65	2.66	2.52
g+g−g−	0.06	0.04	0.04	0.03	0.03	0.03
g+g−t	0.19	0.14	0.13	0.12	0.11	0.09
g+g−g+	0.03	0.02	0.02	0.02	0.02	0.01
g+tg−	2.18	1.94	1.83	1.76	1.77	1.57
g+tt	11.04	7.84	6.88	6.25	5.92	4.82
g+tg+	1.96	1.46	1.29	1.18	1.13	0.93
g+g+g−	0.01	0.01	0.01	0.01	0.01	0.01
g+g+t	2.89	2.08	1.82	1.66	1.59	1.30
g+g+g+	0.77	0.64	0.59	0.56	0.56	0.49

Table 6.5. The tail conformation populations for various mean field strengths, for a temperature of 300K.

These trends are also evident by examining the preferred order of tail conformers. The preferred order in the gas phase, ttt> gtt> tgt> ttg, alternates with application of the mean field and between field strengths of 0.015 and $0.020\mathring{A}^{-2}$ the ordering becomes, ttt> tgt> gtt> ttg. For the higher strengths of mean field, 0.022 and $0.025\mathring{A}^{-2}$, the ordering alternates again with ttg being more populated than gtt; ttt> tgt> ttg> gtt. In summary the ttt and tgt conformations are significantly enhanced by the application of the mean field while the gtt conformers are suppressed. The mean field selectively favours and disfavours certain conformations, according to their shape. In all generality, it can be stated that the most elongated conformers are stabilised in the nematic field. This can be seen clearly by considering the structures with a single *gauche*. The rod-like shape of the all-*trans* conformer is practically not perturbed by a *gauche* in the central position of the chain, while significant deformations are produced if the *gauche* is located at the chain end or, even worse, close to the junction between the chain and the adjacent aromatic rings.

There have been three previous studies that have investigated the tail conformations of 5CB; that of Emsley, Luckhurst and Stockley [170] who used a mean field and RIS approximation, bulk 5CB molecular dynamics simulations [34] and Monte Carlo single molecule simulations [160]. Table 6.6 shows the populations predicted by these studies. As it is not possible to directly relate the mean field strengths of the Monte Carlo simulation to those of this work, the mean field strengths used for comparison are those which give the best agreement with the quoted NMR S_{CD} order parameters. It should also be noted that in the Monte Carlo investigation, details of the molecular biaxiality were neglected in the potential of mean torque.

The results from this work, the Monte Carlo simulations and ELS model all predict an enhancement of the ttt and tgt conformers and a suppression of the gtt conformer. However, there are large disagreements on the exact populations. The Monte Carlo results particularly favour the ttt conformer, with the largest gas phase population of 33% increasing to 39% in the nematic. They also predict that the gtt conformer is

Method	Ordering	ttt%	gtt%	tgt%	ttg%
This work	Gas Phase	24.6	22.0	15.8	15.0
	nematic[a]	32.3	12.2	26.8	12.9
Monte Carlo [160]	Gas Phase	32.7	23.0	12.3	13.7
	nematic[b]	39.0	18.4	14.5	13.7
Molecular Dynamics [34](FA)[c]	nematic	15.4	7.0	25.2	23.0
Molecular Dynamics [34](UA)[d]	nematic	44.7	3.2	31.2	16.2
ELS [170][e]	(isotropic)	22.7	16.7	16.7	16.7
	(nematic)	33.2	9.7	23.2	14.3

[a] Mean field strength of 0.022 $\AA^{-2}$

[b] Mean field strength of 0.875 kJ/mol$^{-1}\AA^{-1}$

[c] Full atomic model

[d] United atom model

[e] Model developed by Emsley, Luckhurst and Stockley to account for variations in orientational ordering along alkyl tails. RIS model used to describe conformations adopted by tail. The potential of mean torque was represented by group contributions, where each rigid segments contribution to the interaction tensor was independent of conformation.

Table 6.6. Conformational populations for the four most populated conformations of the tail, as calculated by this work, Monte Carlo, Molecular Dynamics and the model of Emsley, Luckhurst and Stockley (ELS). All results are for a temperature of 300K.

significantly more populated relative to this work. The gtt conformer corresponds to the tail being bent back on itself and so is the least linear of the conformations, in contrast to the tgt conformer which is the most linear. From the gas to nematic phase, it is interesting to note that Monte Carlo results predict that the relative increase in the ttt population to be greater than that of the tgt population. This suggests that the Monte Carlo simulation does not selectively favour the most elongated conformer. In contrast to the Monte Carlo results, both this work and ELS predict the tgt conformer to have the largest relative increase in population. This is balanced by an equally large decrease in the gtt population. They also predict that the ttg conformer is marginally more favoured in the nematic phase, whereas the Monte Carlo simulation predicts no change.

The Table also shows results from fully atomistic (FA) and united atom (UA) molecular dynamics simulations. The populations predicted by both simulations are very dissimilar which suggests that the type of model used has a great bearing on the results. For what is considered the more realistic simulation, the FA simulation, the populations appear particularly unusual, with the ttt conformer reduced to the third place in terms of ordering. The UA simulation predicts more realistic populations, although both methods significantly underestimate the gtt populations.

6.5 Summary and conclusions

This Chapter investigated the influence of a nematic environment, described by the surface tensor model, on the conformational dynamics of the alkyl tail in 5CB. The order parameters calculated from the surface tensor model for test molecules were found to agree well with experimental observations. Molecular structures and gas phase conformational distributions, as well as charge densities used to define molecular surfaces, were obtained using first principles calculations.

The generation of molecular surfaces from the electronic charge distribution, required a cutoff parameter to be set which related to the percentage of total charge included within the surface boundary. It was found that the appearance and performance of the surface was sensitive to this cutoff and that the surface with the lowest cutoff value gave the best predictions. When compared with rolling sphere and ribbon surfaces, first principles surfaces were found to give similar results. The S_{CD} order parameters of 5CB were then determined and found to be in reasonable agreement with NMR. The relative populations of the tail conformers in 5CB were examined in order to discern the influence of the mean field on conformational dynamics. It was found that the ttt and tgt conformer populations were significantly enhanced by the application of the mean field while the gtt conformers were suppressed. Comparisons were then made with other theoretical investigations into the population distributions and although some similar trends were seen, there was significant disagreement.

Bibliography

[1] P. G. De Gennes. *The Physics of Liquid Crystals*, Clarendon Press, 1974.

[2] G. R. Luckhurst and G. W. Gray, editors. *The Molecular Physics of Liquid Crystals*, Academic press, 1979.

[3] E. B. Priestly, editor. *Introduction to Liquid Crystals*, Plenum Press, New York, 1975.

[4] F. Reinitzer. *Montash. Chem.*, 9:421, 1888.

[5] M. G. Clark, K. J. Harrison and E. P. Raynes. *Phys. Technol.*, 11:232, 1980.

[6] G. H. Heilmeier, L. A. Zanoni and L. A. Barton. *Proc. IE.E.E.*, 56:1162, 1968.

[7] G. W. Gray, K. J. Harrison and J. A. Nash. *Electronics Lett.*, 9:98, 1974.

[8] H. J. Ichler, R. Elschner, G. Heppke, R. Macdonald, H. Schmid. *App. Phys. B*, 61:59, 1995.

[9] L. M. Blinov. *Electrooptic Effects In Liquid Crystals*, Springer Verlag, 1994.

[10] C. J. Adam, S. J. Clark, G. J. Ackland and J. Crain. *Phys. Rev. E*, 55:5641, 1997.

[11] M. Schadt. *Liq. Cryst.*, 5:57, 1989.

[12] W. Maier and A. Saupe. *Z. Naturforsch.*, 13a:564,1958; ibid 14a:882, 1959; ibid 15a:287, 1960.

[13] G. R. Luckhurst. *Ber. Bunsenges. Phys. Chem.*, 97:1169,1993.

[14] J. P. Straley. *Phys. Rev. A*, 10:1881, 1974.

[15] E. Samulski and R. Dong. *J. Chem. Phys.*, 77:5090, 1982.

[16] A. Ferrarini, G. J. Moro, P. L. Nordio and G. R. Luckhurst. *Mol. Phys.*, 77:1, 1992.

[17] R. Y. Dong. *Nuclear Magnetic Resonance of Liquid Crystals*, Springer-Verlag, New York, 1997.

[18] L. Onsager. *Ann. N.Y. Acad. Sci.*, 51:627, 1949.

[19] M. P. Allen. *Philosophical Transactions of the Royal Society London SERIES A*, 344:323, 1993.

[20] Samborski, G. T. Evans, C. P. Mason, M. P. Allen. *Mol. Phys.*, 81:263, 1994.

[21] D. Frenkel. *Mol. Phys.*, 60:1, 1987.

[22] M. P. Allen, G. T. Evans, D. Frenkel and B. M. Mulder. *Adv. Chem. Phys.*, 86:1, 1993.

[23] P. J. Camp and M. P. Allen. *J. Chem. Phys.*, 106:6681, 1997.

[24] M. R. Wilson, M. P. Allen. *Mol. Phys.*, 80:277, 1993.

[25] J. G. Gay and B. J. Berne. *J. Chem. Phys.*, 74:3316, 1981.

[26] D. J. Adams, G. R. Luckhurst and R. W. Phippen. *Mol. Phys.*, 61:1575, 1987.

[27] G. R. Luckhurst, R. A. Stephens and R. W. Phippen. *Liq. Cryst.*, 8:451,1990.

[28] B. J. Berne and P. Pechukas. *J. Chem. Phys.*, 64:4213, 1972.

[29] G. R. Luckhurst and P. S. J. Simmonds. *Mol. Phys.*, 80:223, 1993.

[30] D. J. Cleaver, C. M. Care, M. P. Allen and M. P. Neal. *Phys. Rev. E*, 54:559, 1996.

[31] R. Berardi, C. Fava and C. Zannoni. *Chem. Phys. Lett.*, 236:462, 1995.

[32] M. P. Neal, A. J. Parker and C. M. Care. *Mol. Phys.*, 91:603, 1997.

[33] M. R. Wilson and M. P. Allen. *Liq. Cryst.*, 12:157, 1992.

[34] A. V. Komolkin, A. Laaksonen and A. Maliniak. *J. Chem. Phys.*, 101:4103, 1994.

[35] C. W. Cross and B. M. Fung. *J. Chem Phys.*, 101:6839, 1994.

[36] G. Kromer, D. Paschek and A. Geiger. *Ber. Bunsenges. Phys. Chem.*, 10:1188, 1997.

[37] A. V. Komolkin, Yu. V. Molchanov and P. P. Yakutseni. *Liq. Cryst.*, 6:39, 1989.

[38] D. J. Cleaver, J. M. Callaway, T. Forester, W. Smith and D. J. Tildesley. *Mol. Phys.*, 86:613, 1995.

[39] W. Kohn and L. J. Sham. *Phys. Rev.*, 140:1133A, 1965.

[40] P. Hohenberg and W. Kohn. *Phys. Rev.*, 136:864B, 1964.

[41] M. C. Payne, M. P. Teter, D. C. Allen, T. A. Arias, and J. D. Joannopoulos. *Rev. Mod. Phys.*, 64:1045, 1992.

[42] M. J. Gillan. Calculating The Properties Of Materials From Scratch. In M. Meyer and V. Pontikis, editors. *Computer Simulations in Materials Science*, Kluwer Academic Publishers, Netherlands, 1991.

[43] R. O. Jones. Molecules and Molecular Dynamics. In E. K. U. gross and R. M. Dreizler, editors, *Density Functional Theory*, Plenum Press, New York, 1995.

[44] R. G. Parr and W. Yang. *Density Functional Theory of Atoms and Molecules*, Oxford University Press. 1989.

[45] W. J. Hehre, L. Radom, P. v. R. Schleyer and J. A. Pople. *Ab Initio Molecular Orbital Theory*, John Wiley & Sons, New York, 1986.

[46] C. E. Dykstra. *Ab Initio Calculation Of The Structures And Properties Of Molecules*, Elsevier, 1988.

[47] A. Hinchcliffe. *Ab Initio Determination Of Molecular Properties*, Adam Hilger, Bristol, 1987.

[48] C. Møller and M. S. Plesset. *Phys. Rev.*, 46:618, 1934.

[49] A. D. Becke. *Phys. Rev. A*, 38:3098, 1988.

[50] C. Lee, W. Yang and R. Parr. *Phys. Rev. B*, 37:785, 1988.

[51] D. C. Langreth and J. P. Perdew. *Phys. Rev. B*, 15:2884, 1977.

[52] D. M. Ceperley and B. J. Alder. *Phys. Rev. Lett.*, 45:566, 1980.

[53] J. P. Perdew and A. Zunger. *Phys. Rev. B*, 23:5048, 1981.

[54] J. P. Perdew, J. A. Chevary, S. H. Vosko, K. A. Jackson, M. R. Pederson, D. J. Singh and C. Fiolhais. *Phys. Rev. B.* 46:6671, 1992.

[55] J. D. Perdew. Density gradient expansion of the electronic exchange-correlation energy, and its generalization. In E. K. U. Gross and R. M. Dreizler, editors, *Density Functional Theory*, Plenum Press, 1993.

[56] M. Schluter, and L. J. Sham. *Phys. Today*, 35:36, 1982.

[57] M. T. Yin and M. L. Cohen. *Phys. Rev. B*, 25:7403, 1982

[58] D. R. Hamann, M. Schluter, and C. Chiang. *Phys. Rev. Lett.*, 43:1494, 1979.

[59] G. B. Bachelet, D. R. Hamann and M. Schluter. *Phys. Rev. B*, 26:4199, 1982.

[60] J. S. Lin, A. Qteish, M. C. Payne, and V. Heine. *Phys. Rev. B*, 47:4147, 1993.

[61] M-H. Lee. *Advanced Pseudopotentials.* PhD Thesis, The University of Cambridge, 1995.

[62] L. Kleinman and D. M. Bylander. *Phys. Rev. Lett.*, 48:1425, 1982.

[63] N. W. Ashcroft and N. D. Mermin. *Solid State Physics*, Saunders College Publishing, Florida, 1976.

[64] R. Fletcher and C. M. Reeves. *Comput. J.*, 7:149, 1964.

[65] R. Car and M. Parrinello. *Phys. Rev. Lett.*, 55:2471, 1985.

[66] M. R. Jarvis, I. D. White, R. W. Godby and M. C. Payne. *Phys. Rev. B*, 56:14972, 1997.

[67] P. P. Ewald. *Ann. Phys. (Leipzig)*, 64:253, 1921.

[68] L. J. Clarke, I. Stich, and M. C. Payne, *Comput. Phys. Commun.*, 72:14, 1992.

[69] J. A. White and D. M. Bird. *Phys. Rev. B*, 50:4954, 1994.

[70] Cerius^2 is a molecular modelling package distributed by Biosym Molecular Simulations Inc.

[71] J. Crain, G. J. Ackland and S. J. Clark. *Rep. Prog. Phys.*, 58:705, 1995.

[72] H. C. Hsueh, H. Vass, S. J. Clark and J. Crain. *Europhys. Lett.*, 31:503, 1997.

[73] J. Crain, G. J. Ackland, R. O. Piltz, P. D. Hatton. *Phys. Rev. Lett.* , 70:814, 1997.

[74] J. M. Holender and M. J. Gillan. *Phys. Rev. B*, 53:4399, 1996.

[75] J. M. Holender, M. J. Gillan, M. C. Payne, A. D. Simpson. *Phys. Rev. B*, 52:967, 1995.

[76] H. C. Hsueh, J. R. Maclean, G. Y. Guo, M. H. Lee, S. J. Clark, G. J. Ackland and J. Crain. *Phys. Rev. B*, 51:12216, 1995.

[77] S. J. Clark, G. J. Ackland, J. Crain and M. C. Payne, *Phys. Rev. B*, 50:5728, 1994

[78] R. Perez, M. C. Payne and A. D. Simpson, *Phys. Rev. Lett.*, 75:4748, 1995.

[79] I. Stich, M. C. Payne, R. D. Kingsmith, J. S. Lin, L. J. Clarke, K. D. Brommer, J. D. Joannopoulos and B. E. Larson. *Phys. Rev. Lett.*, 71:3613, 1993.

[80] A. DeVita, I. Stich, M. J. Gillan, M. C. Payne and L. J. Clarke. *Phys. Rev. Lett.*, 71:1276, 1993.

[81] C. J. Adam, S. J. Clark, M. R. Wilson, G. J. Ackland, and J. Crain. *Mol. Phys.*, 93:947, 1998.

[82] C. J. Adam, S. J. Clark, G. J.Ackland and J. Crain. *SPIE Proceedings of the European Conference on Liquid Crystals*, 3318:171, 1998.

[83] V. Milman and M. -H. Lee. *J. Phys. Chem.*, 100:6093, 1996.

[84] M. D. Segall, M. C. Payne and R. N. Boyes. *Mol. Phys.*, 93:365, 1998.

[85] R. Feynman. *Phys. Rev.*, 56:340, 1939.

[86] P. Pulay. *Mol. Phys.*, 17:197, 1969.

[87] A. Garcia, E. M. Cruz, C. Sarasola and J. M. Ugalde. *J. Mol. Struct*, 363:279, 1996.

[88] L. J. Brenner, J. Senekowtsch and R. E. Wyatt. *Chem Phys. Lett.*, 215:63, 1993.

[89] L. Goodman, A. G. Ozkabak, S. N. Thakur. *J. Phys. Chem.*, 95:9044, 1991.

[90] P. E. Maslen, N. C. Handy, R. D. Amos and D. Jayatilaka. *J. Chem. Phys.*, 97:4233, 1992.

[91] N. C. Handy, P. E. Maslen, R. D. Amos, J. S. Andrews, C. W. Murray and G. J. Laming. *Chem. Phys. Lett.*, 197:506, 1992.

[92] A. Berces and T. Zeigler. *J. Chem. Phys.*, 98:9044, 1993.

[93] N. L. Allinger, J. T. Fermann, A. D. Wesley and H. F. Schaefer III. *J. Chem. Phys*, 12:106, 1997.

[94] R. A. Bonham and L. S. Bartell. *J. Am. Chem. Soc.*, 81:3491, 1959.

[95] U. Rothlisberger and M. L. Klein. *Chem. Phys. Lett.*, 227:390, 1994.

[96] K. Rhagavachari. *J. Chem. Phys.*, 81:1383, 1984.

[97] K. B. Wiberg and M. A. Murcko. *J. Am. Chem. Soc.*, 110:8029, 1988.

[98] S. S. Chen, R. C. Wilhoit and B. J. Zwolinski. *J. Phys. Chem.*, 4:185, 1975.

[99] W. F. Bradford, S. Fitzwater and L. S. Bartell. *J. Mol. Struct.*, 38:158, 1977.

[100] G. B. Robertson. *Nature*, 191:593, 1961.

[101] A. Almenningen, O. Bastiansen, L. Fernholt, B. N. Cyvin, S. J. Cyvin and S. Smadal. *J. Mol. Struct.*, 128:59, 1985.

[102] S. Tsuzuki and K. Tanabe. *J. Phys. Chem*, 95:139, 1991.

[103] M. Rubio, M. Merchan and E. Orti. *Theor. chim. Acta*, 91:17, 1995.

[104] M. Bremer. *Advanced Materials*, 7:867, 1995.

[105] H. Y. Yin and J. X. Wen. *Liq. Cryst.*, 21:217, 1996.

[106] C. Jones , *Optical and Dielectric studies of Smectic C Liquid Crystals*, PhD Thesis, University of Hull, 1991.

[107] M. Edgar, J. W. Emsley and M. I. C. Furby. *J. Mag. Reson.*, 128:105, 1997.

[108] B. Aldridge, G. De-Luca, M. Edgar, S. J. Edgar, J. W. Emsley, M. I. C. Furby and M. Webster. *Liq. Cryst.*, 24:569, 1998.

[109] O. Bastiansen and L. Smedvik. *Acta Chem. Scand.*, 8:1595, 1954.

[110] S. Papasavva, K. H. Illinger and J. E. Kenny. *J. Phys. Chem.*, 100:101100, 1996.

[111] M. Edgar, C. J. Adam, M. I. C. Furby and J. W. Emsley. in preparation, 1998.

[112] G. Celebre, M. Longeri, E. Sicilia and J. W. Emsley. *Liq. Cryst.*, 7:731, 1990.

[113] S. J. Clark, C. J. Adam, D. J. Cleaver and J. Crain. *Liq. Cryst.*, 22:477, 1997.

[114] J. C. Decius and R. M. Hexter. *Molecular Vibrations in Crystals*, McGraw-Hill Inc., 1977.

[115] S. J. Clark, C. J. Adam, G. J. Ackland, J. White and J. Crain. *Liq. Cryst.*, 22:469, 1997.

[116] H. C. Hsueh, H. Vass, F. N. Pu, S. J. Clark, C. K. Poon and J. Crain. *Europhys. Lett*, 38:107, 1997.

[117] M. P. Allen and M. R. Wilson. *J. Computer-Aided Mol. Design*, 3:335, 1989.

[118] U. Burkert and N. L. Allinger. *Molecular Mechanics*, ACS Monograph, Washington D. C., 1982.

[119] N. L. Allinger, Y. H. Yuh and J. -H. Lii. *J. Am. chem. Soc*, 111:8551, 1990.

[120] Private discussion with Dr. M. R. Wilson, June 1996.

[121] J. W. Emsley, G. De Luca, G. Celebre and M. Longeri. *Liq. Cryst.*, 20:569, 1996.

[122] J. W. Emsley, M. I. C. Furby and G. Deluca, *Liq. Cryst.*, 21:877, 1996.

[123] N. L. Allinger, R. S. Grev, B. F. Yates and H. F. Schaefer III. *J. Am. Chem. Soc.*, 112:114, 1990.

[124] D. A. Dixon. *J. Phys. Chem.*, 96:3698, 1992.

[125] J. C. Smith and M. Karplus. *J. Am. Chem. Soc.*, 81:3491, 1992.

[126] J. P. Ryckaert and A. Bellemans. *Chem. Phys. Lett.*, 30:123, 1975.

[127] J. P. Perdew. *Phys. Rev. B*, 38:3098, 1986.

[128] F. Mandel. *Statistical Physics*, J. Wiley & Sons, 1988.

[129] J. W. Emsley, T. J. Horne, G. Celebre, M. Longeri and H. Zimmermann. *J. Phys. Chem.*, 96:7929, 1992.

[130] W. Caminati, D. Damiani, G. Corbelli, B. Velino and C. W. Bock. *Mol. Phys.*, 74:885, 1991.

[131] MM3 structure and energies were provided by Dr. Mark Wilson of Durham University using the CACHE molecular mechanics program.

[132] P. J. Flory. *Statistical Mechanics of Chain Molecules*, Interscience, New York, 1969.

[133] W. L. Jorgensen. *J. Am. Chem. Soc.*, 103:677, 1981.

[134] E. Vilaseca. *J. Chem. Phys.*, 104:4243, 1996.

[135] W. M. Gelbart. *J. Phys. Chem.*, 86:4298, 1982.

[136] A. J. van der Est, M. Y. Kok and E. E. Burnell. *Mol. Phys.*, 60:397, 1987.

[137] D. S. Zimmerman and E. E. Burnell. *Mol. Phys.*, 69:1059, 1990.

[138] J. M. Polson and E. E. Burnell. *Mol. Phys.*, 88:767, 1996.

[139] T. Chandrakumar and E. E. Burnell. *Mol. Phys.*, 90:303, 1997.

[140] A. F. Terzis and D. J. Photinos. *Mol. Phys.*, 83:847, 1994.

[141] S. C. McGrother, A. Gilvillegas abd G. Jackson. *J. Phys-Cond. Mat.*, 8:9649, 1996.

[142] K. Satoh , S. Mita and S. Kondo. *Liquid Crystals*, 20:757, 1996.

[143] K. Satoh, S. Mita and S. Kondo. *Chem. Phys. Lett.*, 255:99, 1996.

[144] G. Barbero and G. Durand. *Mol. Cryst. Liquid Cryst*, 179:57, 1990.

[145] R. Berardi, S. Orlandi and C. Zannoni. *Chem. Phys. Lett.*, 261:357,1996.

[146] G. Ayton, D. Q. Wei and G. N. Patey. *Phys. Rev. E*, 55:447, 1997.

[147] C. G. Gray and K. E. Gubbins. *Theory of Molecular Fluids*, Claredon Press, Vol. 1, 1984.

[148] P. J. Wheatley. *The Determination of Molecular Structure*, Dover Publications, New York, 1968.

[149] A. J. Seed, K. J. Toyne, J. W. Goodby and D. G. McDonnell, *J. Mater. Chem*, 5:1, 1995.

[150] M. P. Neal and A. J. Parker. *Chem. Phys. Lett.*, 'in press', 1998.

[151] A. Poniewierski and T. J. Sluckin. *Mol. Phys.*, 73:199, 1991.

[152] G. R. Dennis and G. L. D. Ritchie. *J. Phys. Chem.* 95:656, 1991.

[153] C. J. Adam, M. P. Neal, G. J. Ackland and J. Crain. *Mol. Phys*, submitted, 1998.

[154] M. J. Gunning and R. E. Raab. *Mol. Phys.*, 91:589, 1997.

[155] A. D. Buckingham. *Adv. Chem. Phys.*, 12:107, 1967.

[156] S. L. Price, A. J. Stone and M. Alderton. *Mol. Phys*, 52:987, 1984

[157] S. L. Price. *J. Chem. Soc. Faraday Trans.*, 92:2997, 1996.

[158] D. Sanchez-Portal, E. Artacho and J. M. Soler. *Solid State Comm.*, 95:685, 1995.

[159] M. D. Segall, R. Shah and M. C. Payne. *Phys. Rev. B*, 54:16317, 1996.

[160] M. R. Wilson. *Liq. Cryst.*, 21:437, 1996.

[161] G. Celebre, G. De Luca and A. Ferrarini. *Mol. Phys.*, 92:1039, 1997.

[162] A. Ferrarini and P. L. Nordio. *J. Chem. Soc. Faraday Trans.*, 88:1733, 1992.

[163] A. Ferrarini, G. R. Luckhurst, P. L. Nordio and S. J. Roskilly. *J. Chem. Phys.*, 100:1460, 1994.

[164] A. Ferrarini, G. J. Moro and P. L. Nordio. *Mol. Phys.*, 87:485, 1996.

[165] P. B. Barker, A. J. van Der Est, E. E. Burnell, G. N. Patey, C. A. De Lange and J. G. Snijders. *Chem. Phys. Lett.*, 107:426, 1984.

[166] A. J. van Der Est, M. Y. Kok and E. E. Burnell. *J. Chem. Soc. Faraday Trans. 2*, 84:1095, 1988.

[167] R. T. Syvitski and E. E. Burnell. *Chem. Phys. Lett.*, 281:199, 1997.

[168] C. J. Adam, A. Ferrarini, M. R. Wilson, G. J. Ackland and J. Crain. *Mol. Phys*, submitted, 1998.

[169] D. M. Brink and G. R. Satchler. *Angular Momentum*, Claredon press, 1975.

[170] J. W. Emsley, G. R. Luckhurst and C. P. Stockley. *Proc. R. Soc. Lond. A*, 381;117, 1982.

[171] M. L. Connolly. *Science*, 221:709, 1985.

[172] A. Ferrarini, F. Janssen, G. J. Moro and P. L. Nordio. submitted, 1998.

[173] W. E. Lorensen and H. E. Cline. *Computer Graphics*, 21:163, 1987.

[174] AVS/Express is a data visualisation package distributed by Advanced Visual Systems.

[175] J. W. Emsley, G. R. Luckhurst and C. P. Stockley. *Mol. Phys.*, 44:565, 1981.